LEVEL

INVENTORY

1

AD-A198 938

DTIC ACCESSION NUMBER

TR 26   N00014-83-K-0383

DOCUMENT IDENTIFICATION

FeB 88

This document has been approved
for public release and sale; its
distribution is unlimited.

DISTRIBUTION STATEMENT

ACCESSION FOR	
NTIS GRA&I	☑
DTIC TAB	☐
UNANNOUNCED	☐
JUSTIFICATION	

BY
DISTRIBUTION /
AVAILABILITY CODES

DIST	AVAIL AND/OR SPECIAL

A-1

DISTRIBUTION STAMP

HELD
COPY
INSPECTED

DTIC
SELECTED
SEP 2 8 1988
E

DATE ACCESSIONED

DATE RETURNED

88 9   8 046

DATE RECEIVED IN DTIC

REGISTERED OR CERTIFIED NO.

DTIC FORM 70A
DEC 83

DOCUMENT PROCESSING SHEET

PREVIOUS EDITION MAY BE USED UNTIL
STOCK IS EXHAUSTED.

① SOT1

88-17

Office of Naval Research

JOSEPHSON JUNCTION ARRAYS WITH POSITIONAL DISORDER: EXPERIMENTS AND SIMULATIONS

④ TR No. 26

AD-A198 938

ADVISORY GROUP
RECEIVED
APR 18 1988
ON ELECTRON DEVICES

By

Martin Gerard Forrester

⑤ February 1988

Technical Report No. 26

This report covers TI number(s) _None_
(HAU)

Technical Information

Extracted: Date: _____

Division of Applied Sciences
② **Harvard University   ·   Cambridge, Massachusetts**

③ N00014-83-K-0383

JOSEPHSON JUNCTION ARRAYS WITH POSITIONAL DISORDER: EXPERIMENTS AND SIMULATIONS

by

.Martin Gerard Forrester

Technical Report No. 26

February 1988

Division of Applied Sciences
Harvard University · Cambridge, Massachusetts

REPORT DOCUMENTATION PAGE		READ INSTRUCTIONS BEFORE COMPLETING FORM
1. REPORT NUMBER Technical Report No. 26	2. GOVT ACCESSION NO.	3. RECIPIENT'S CATALOG NUMBER
4. TITLE (and Subtitle) Josephson Junction Arrays with Positional Disorder Experiments and Simulations		5. TYPE OF REPORT & PERIOD COVERED
		6. PERFORMING ORG. REPORT NUMBER
7. AUTHOR(s) Martin Gerard Forrester		8. CONTRACT OR GRANT NUMBER(s) Contract N00014-83-K-0383. NSF Grant DMR-84-04489 NSF Grant DMR-86-14003
9. PERFORMING ORGANIZATION NAME AND ADDRESS		10. PROGRAM ELEMENT, PROJECT, TASK AREA & WORK UNIT NUMBERS
11. CONTROLLING OFFICE NAME AND ADDRESS Division of Applied Sciences Harvard University Cambridge, MA 02138		12. REPORT DATE February 1988
		13. NUMBER OF PAGES 135
14. MONITORING AGENCY NAME & ADDRESS(if different from Controlling Office)		15. SECURITY CLASS. (of this report) Unclassified
		15a. DECLASSIFICATION. DOWNGRADING SCHEDULE

16. DISTRIBUTION STATEMENT (of this Report)

Reproduction in whole or in part is permitted for any purpose of the United States Government. Approved for public release; distribution unlimited.

17. DISTRIBUTION STATEMENT (of the abstract entered in Block 20, if different from Report)

18. SUPPLEMENTARY NOTES

19. KEY WORDS (Continue on reverse side if necessary and identify by block number)

Josephson junctions
Positional disorder
Monte Carlo simulations

20. ABSTRACT (Continue on reverse side if necessary and identify by block number)

We present the results of a study of Josephson junction arrays with positional disorder, using both experiments and Monte Carlo simulations. We have fabricated 50×50 arrays of Pb/Cu proximity-effect junctions, with controlled positional disorder characterized by a parameter Δ^+. The zero-field resistive transitions of these samples are

well described by the Kosterlitz-Thouless-Halperin-Nelson vortex-unbinding theory. Measurements of resistance vs. magnetic field reveal rich structure, with pronounced minima at integer fields, as well as higher-order structure. In samples with disorder the principal oscillations are found to decay linearly with field, after accounting for the effect of the magnetic field on the critical currents of the individual junctions. We can quantify the destruction of phase-coherence on length-scales of order q times the lattice parameter by defining critical fields, $f_c(q) \propto 1/\Delta^*$, by the disappearance of structures at fields $f_o = p/q$, where f_o is the average number of flux quanta per plaquette, and p and q are integers. Extrapolation to $q = \infty$ yields an estimate of the critical field, f_c, for the destruction of quasi-long-range phase coherence which is in good agreement with the theoretical prediction of Granato and Kosterlitz. However, our experiments show no evidence for the predicted reentrant phase transition.

Our Monte Carlo simulations of XY spin systems with positional disorder reveal reentrant behavior in the helicity modulus Y, which is the analog of the effective superfluid density in a junction array, in a narrow range of magnetic fields near the theoretical critical field. As the temperature decreases, Y first increases, then decreases over a narrow temperature range, and finally increases again at low temperatures. We suggest that the complete reentrance proposed theoretically is prevented by either finite-size effects or pinning of vortices due to the disorder.

ABSTRACT

We present the results of a study of Josephson junction arrays with positional disorder, using both experiments and Monte Carlo simulations. We have fabricated 50×50 arrays of Pb/Cu proximity-effect junctions, with controlled positional disorder characterized by a parameter Δ^*. The zero-field resistive transitions of these samples are well described by the Kosterlitz-Thouless-Halperin-Nelson vortex-unbinding theory. Measurements of resistance vs. magnetic field reveal rich structure, with pronounced minima at integer fields, as well as higher-order structure. In samples with disorder the principal oscillations are found to decay linearly with field, after accounting for the effect of the magnetic field on the critical currents of the individual junctions. We can quantify the destruction of phase-coherence on length-scales of order q times the lattice parameter by defining critical fields, $f_c(q) \propto 1/\Delta^*$, by the disappearance of structures at fields $f_o = p/q$, where f_o is the average number of flux quanta per plaquette, and p and q are integers. Extrapolation to $q = \infty$ yields an estimate of the critical field, f_c, for the destruction of quasi-long-range phase coherence which is in good agreement with the theoretical prediction of Granato and Kosterlitz. However, our experiments show no evidence for the predicted reentrant phase transition.

Our Monte Carlo simulations of XY spin systems with positional disorder reveal reentrant behavior in the helicity modulus Y, which is the analog of the effective superfluid density in a junction array, in a narrow range of magnetic fields near the theoretical critical field. As the temperature decreases, Y first increases, then decreases over a narrow temperature range, and finally increases again at low temperatures. We suggest that the complete reentrance proposed theoretically is prevented by either finite-size effects or pinning of vortices due to the disorder.

iv

TABLE OF CONTENTS

LIST OF FIGURES

CHAPTER ONE

THEORETICAL BACKGROUND

1.1 Introduction

Two-dimensional arrays of Josephson junctions are excellent model systems for the study of various problems in the statistical physics of two-dimensional systems. (For a review see Lobb, 1984.) These include the Kosterlitz-Thouless transition, the effects of frustration on phase transitions, commensurate-incommensurate transitions, and the effects of disorder. For example, an array in zero magnetic field provides a realization of a pure XY magnet, and undergoes a Kosterlitz–Thouless transition, while an array in a finite field is a model for the uniformly frustrated XY magnet, the critical behavior of which is far from understood.

Since such arrays can be designed and fabricated in a very controlled way, through the use of photolithography, for example, one has the capability to produce two-dimensional systems with a wide variety of controlled geometries. For example one can introduce controlled disorder by specifying that certain junctions should not be present in an otherwise regular array. An array with junctions randomly removed provides a realization of a dilute two-dimensional magnet, whose critical behavior may be drastically altered when the disorder becomes sufficiently strong.

In this work we are concerned with arrays whose superconducting sites are given random displacements from their "equilibrium" positions (Forrester et al., 1987). This results in a realization of the XY magnet with disorder and frustration, which theory suggests may show novel behavior, including a critical value of the disorder, and a reentrant phase transition.

Before discussing the theory for this non-uniformly frustrated XY system, it is important to review the fundamental concepts behind the critical behavior of two-dimensional systems. In the next section we review the topic of ordering in two dimensions, and in the subsequent section the Kosterlitz-Thouless transition, before moving on to the topic of XY magnets with uniform and non-uniform frustration.

1.2 Ordering in two dimensions

The critical behaviors of two-dimensional (2D) systems such as superfluid and magnetic films are of great interest because, theoretically, such systems cannot show long-range order (Mermin and Wagner, 1966; see also, Peierls, 1934). Consider, for example, the correlation functions

$$G(\mathbf{r}) = \langle \psi(\mathbf{r}) \psi^*(0) \rangle \qquad \text{Superfluid} \qquad (1.1a)$$

$$\langle \mathbf{S}(\mathbf{r}) \cdot \mathbf{S}(0) \rangle \qquad \text{Magnet} \qquad (1.1b),$$

where $\psi(\mathbf{r})$ is the condensate wave function for the superfluid, and $\mathbf{S}(\mathbf{r})$ is the local moment in the magnet. In three dimensions such correlation functions can show three types of behavior at large distances r. In the disordered state (normal state in a superfluid, and paramagnetic state in a magnet) correlations decay exponentially with distance,

$$G(\mathbf{r}) \sim \exp\left(\frac{-r}{\xi(T)}\right) \qquad (1.2),$$

where $\xi(T)$ is a temperature-dependent correlation length. The ordered state is characterized by $G(\mathbf{r})$ decaying to a non-zero value at large r:

$$\lim_{r\to\infty} G(\mathbf{r}) = \text{const.} \neq 0 \qquad (1.3).$$

In a superfluid this means that one has a macroscopic quantum state, characterized by a single phase, while in a magnet one has a spontaneous magnetization. The third type of behavior is possible only at second order critical points, and is characterized by *algebraic* decay of correlations:

$$G(\mathbf{r}) \sim \frac{1}{r^{d-2-\eta}} \qquad .$$

In two-dimensional systems with a continuous symmetry the behavior in (1.3) is impossible, because fluctuations are extremely effective at destroying order. However, Berezinski (1971) and Kosterlitz and Thouless (KT) (1973, and Kosterlitz 1974) have shown that certain 2D systems, including superfluids, crystalline solids, and XY magnets, can undergo a finite-temperature phase transition, between a disordered state characterized by (1.2) and a state with "quasi-long-range coherence" (QLRC), characterized by,

$$G(\mathbf{r}) \sim \frac{1}{r^{\eta(T)}} \qquad (1.4),$$

with $\eta(T)$ a temperature-dependent exponent. This transition is brought about by the unbinding of defects – dislocations in crystals, and vortices in superfluids and XY magnets – whose interaction energy is logarithmic in their separation.

For further discussion we now specialize to a particular realization of the XY magnet – the Josephson junction array.

1.3 Josephson junction arrays and the Kosterlitz Thouless transition

It is well known that a 2D array of Josephson junctions is isomorphic to a 2D XY spin system. As illustrated s   matically in Fig. 1.1, such an array consists of superconducting islands, each characterized by a superconducting order parameter, $\psi_j \exp(i\theta_j)$, connected by Josephson junctions. The coupling energy of a pair of such islands, i and j, is given by

$$E = -J(T)\cos(\theta_i - \theta_j) \qquad (1.5),$$

where $J(T) = \hbar i_c/2e$ is the Josephson energy, and $i_c(T)$ is the critical current of the junction (Tinkham, 1975). The Hamiltonian for an array is obtained by summing terms like (1.5) over nearest neighbors on a lattice:

$$H = -J\sum_{<i,j>}\cos(\theta_i - \theta_j) \qquad (1.6).$$

(When interpreting experimental data one uses an effective temperature $T'=TJ(T_c)/J(T)$, which enables one to consider the coupling constant J in (1.6) to be temperature independent (Abraham et al, 1982; Lobb et al., 1983)).The ground state of this system clearly has all θ's equal (all spins aligned in the XY magnet). This ordered state is, however, destroyed at finite temperatures by two types of excitation – spin waves and vortices, illustrated in Figs. 1.2a and 1.2b respectively. It is the spin waves which destroy the long-range order (1.3) in favor of the algebraic order (1.4), while the vortices are responsible for the phase transition to the disordered state (1.2).

The energy of an isolated vortex is given by (Lobb et al.,1983)
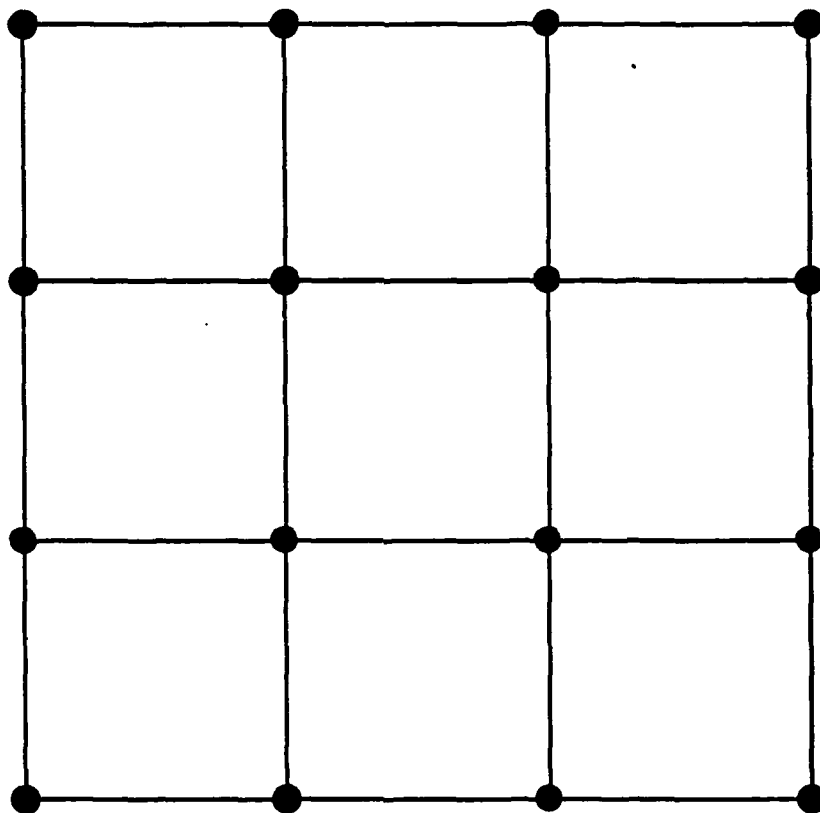
Figure 1.1   Schematic diagram of a Josephson junction array.   The dark circles are superconducting islands, and the lines are junctions.

(a)

(b)
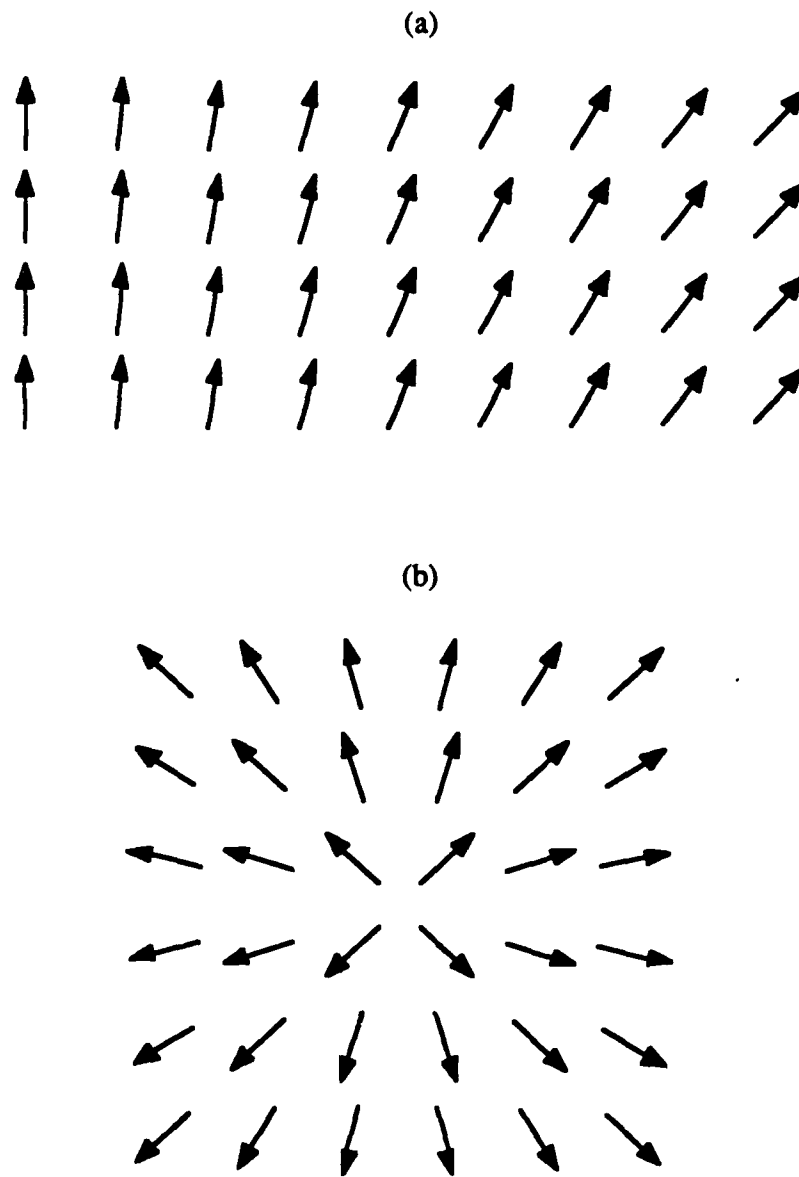
Figure 1.2   (a) Spin wave and (b) vortex excitations in a 2D XY magnet. In an array, arrows represent the phases θ_i.

$$E_1 = \pi J \ln(R/s) \tag{1.7},$$

where R is the sample size and s is the lattice spacing, while the energy of interaction of a vortex pair is

$$U_{12} = \pm 2\pi J \ln(r_{12}/s) \tag{1.8},$$

where r_{12} is the distance between the vortex centers. The key idea of the KT transition is that for $T < T_c$ these vortices are bound in dipole pairs of zero net vorticity, and since such pairs are not displaced by a small transport current, there is no dissipation. Above T_c the vortices become unbound, and can be displaced by a transport current, resulting in dissipation. However, even below T_c a finite current can cause vortex pairs to unbind, and this results in power-law current-voltage (I-V) characteristics,

$$V \sim I^{a(T)} \tag{1.9}$$

below T_c. It turns out that the measurable quantitiy $a(T)$ is related to the effective superfluid density, n_s, or spin wave stiffness, as is another measurable quantity, the kinetic inductance L_K:

$$a(T) - 1 \propto n_s(T) \propto L_K^{-1}(T) \tag{1.10}.$$

Nelson and Kosterlitz (1977) predicted that $n_s(T)$ should undergo a discontinuous jump at T_c, with $n_s(T_c)/T_c$ a universal quantity. In experiments this "universal jump" should be manifested in a discontinuity in $a(T)$, with $a(T_c^-)=3$ and $a(T_c^+)=1$. In practice finite voltage sensitivity and finite sample size lead to the measured discontinuity in $a(T)$ being

smeared out. Nevertheless, measurements of both $a(T)$ from dc I-V characteristics (Abraham $et\ al.$, 1982) and $L_K^{-1}(T)$ from ac impedance measurements (Leemann $et\ al.$, 1986) seem to be in reasonably good agreement with theory.

Above T_c the characteristic length for the decay of correlations was shown by KT to be

$$\xi_+(T) = cs \exp\left[b/(T-T_c)^{\frac{1}{2}}\right] \tag{1.11},$$

where c is a constant of order unity, and s is the vortex core size. Interpreting this length as the average distance between free vortices above T_c, so that the free vortex density $n_F \propto 1/\xi_+^2$, leads to a resistance $R \propto n_F$,

$$R(T) = R_o \exp\left[-2b/(T-T_c)^{\frac{1}{2}}\right] \tag{1.12}.$$

This unusual temperature dependence has been verified quite well in measurements on arrays (Voss and Webb, 1982; Resnick $et\ al.$,1982; Abraham $et\ al.$, 1982), as long as data are interpreted using the rescaled temperature T' mentioned earlier.

1.4 Junction arrays in a magnetic field – the frustrated XY model

In the presence of a perpendicular magnetic field the array Hamiltonian (1.6) becomes

$$H = -J \sum_{<i,j>} \cos(\theta_i - \theta_j - \psi_{ij}) \tag{1.13}$$

$$\psi_{ij} = \frac{2\pi}{\Phi_o} \int_i^j \mathbf{A} \cdot d\mathbf{l}$$ (1.14).

Here $\mathbf{A}$ is the magnetic vector potential and $\Phi_o = hc/2e$ is the superconducting flux quantum, and the ψ_{ij}'s satisfy the constraint

$$\sum \psi_{ij} = 2\pi(m+f) \qquad m=0,\pm1,\pm2,\ldots\ldots$$ (1.15),

where the summation is around any plaquette. This is the Hamiltonian of a uniformly frustrated XY magnet, with tunable frustration parameterized by $f = Bs^2/\Phi_o$, the number of flux quanta per plaquette. The ground state energy and transition temperature of this system have been shown to be extremely complicated discontinuous functions of f, as illustrated in Fig. 1.3 (Alexander, 1982; Rammal et al., 1982; Shih and Stroud, 1983). Measurements on both arrays of junctions (Webb et al., 1983; Tinkham et al., 1983; Kimhi et al., 1984; Brown and Garland, 1986; Van Wees et al., 1987) and wire networks (Pannetier et al., 1983) have shown this behavior, albeit somewhat smeared out by sample imperfections, in measurements of T_c, resistance, and apparent critical current, as a function of field. (By "apparent critical current" we mean the current at which the sample voltage exceeds some fixed threshold, usually limited by the sensitivity of the voltmeter. The theoretical zero-voltage critical current is zero at finite temperatures, in two dimensions, because there is no long-range order).

There has also been a great deal of interest in the nature of the phase-transition at particular values of the frustration f. For example, the ground state for a square array with $f=1/2$, the so-called "fully frustrated" case, has been shown to have the structure shown in Fig. 1.4a (Teitel and Jayaprakash, 1983), where + (−) designates a clockwise (counterclockwise) circulating supercurrent, of magnitude $i_c/\sqrt{2}$. The discrete degeneracy
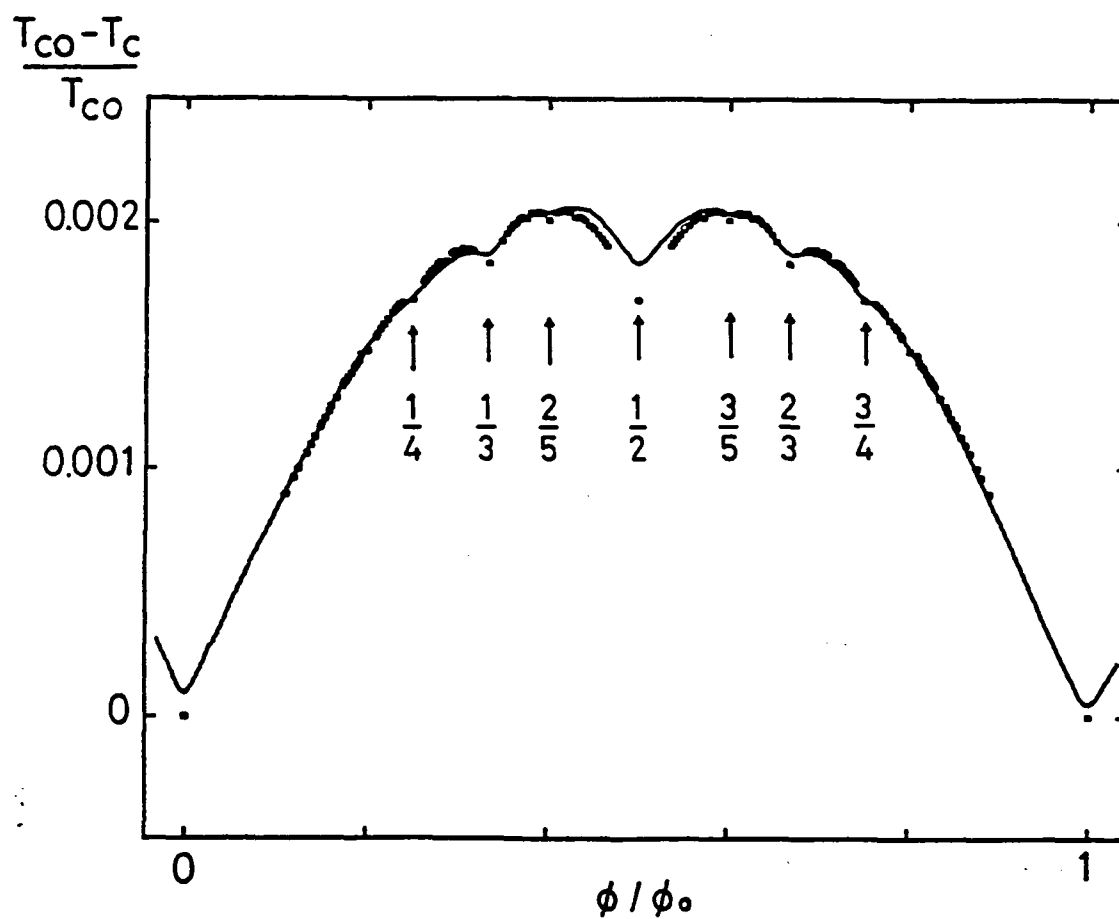
Figure 1.3 Transition temperature of a square superconducting network or Josephson junction array as a function of magnetic field, as computed from mean-field theory (points), and as measured (solid line) for an aluminum network (From Pannetier *et al.*, 1983).
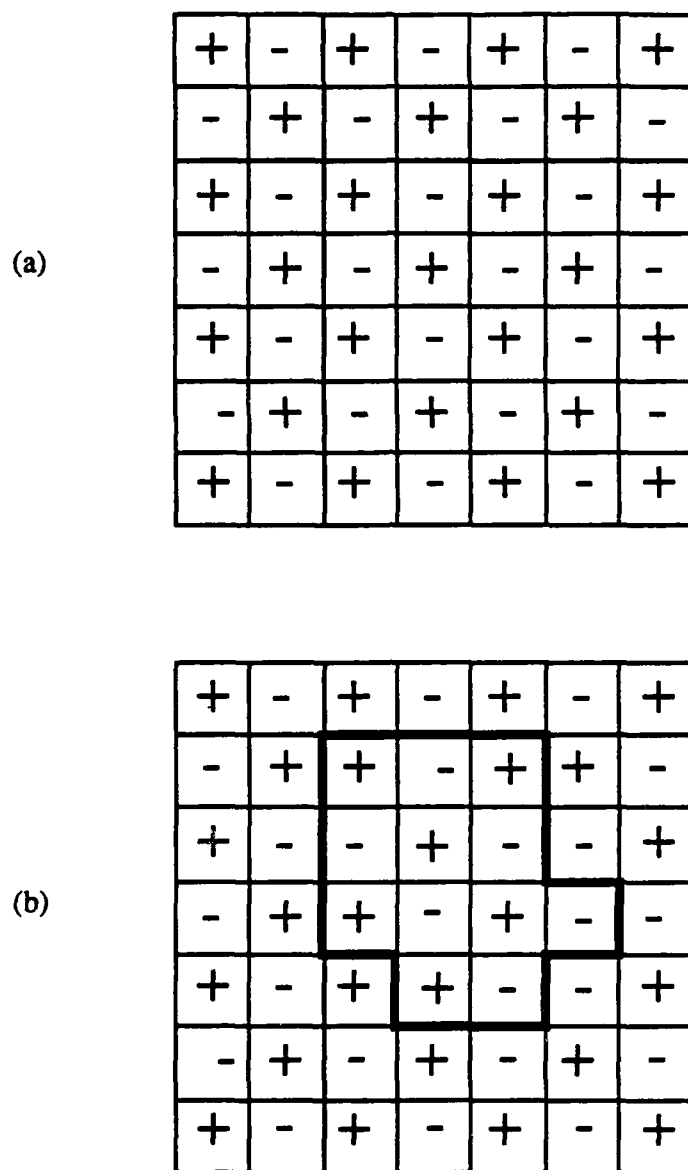
Figure 1.4 (a) Ground state for the uniformly frustrated array with f=1/2. Plus (minus) represents a clockwise (counterclockwise) circulating supercurrent of magnitude $i_c/\sqrt{2}$. (b) Domain wall excitation (dark outline) at finite temperature.

of this ground state suggests the possibility of an Ising-like transition, brought about by domain walls (Fig. 1.4b), perhaps in combination with vortices. Monte Carlo simulations have shown that the specific heat appears to diverge at the transition, consistent with an Ising transition (Teitel and Jayaprakash, 1983). Despite intensive theoretical study of this problem (Teitel and Jayaprakash, 1983; Halsey, 1985; Yosefin and Domany, 1985; Choi and Stroud, 1985; Granato and Kosterlitz, 1986a) the nature of the transition is still uncertain, except that it appears to have both Ising- and KT-like characteristics. Experiments have so far shed little light on this particular problem, most work being unable to distinguish any difference between the transitions at $f = 0$ and $f = 1/2$. However, recent results on proximity arrays suggest that excitations other than vortices, perhaps domain walls, may be responsible for additional voltage noise at $f = 1/2$ (Van Harlingen and Springer, 1987). Also, Van Wees *et al.* (1987) have reported evidence for a non-universal jump in fully frustrated tunnel junction arrays, with $a(T_c^-) \approx 4.5$ and $a(T_c^+) = 1$. These authors invoke theoretical work by Minnhagen (1985) to suggest that the transition is KT-like, despite the non-universal jump.

1.5 Junction arrays with disorder

So far we have been discussing arrays as perfect representations of the XY Hamiltonian. However, there are inherent limitations in sample design and fabrication which prevent an exact correspondence between actual arrays and the XY Hamiltonian in (1.13). For example, we have already mentioned that the coupling energy J is temperature-dependent, necessitating the use of a rescaled temperature $T'=TJ(T_c)/J(T)$ when comparing data to theory. In addition, real junctions are extended rather than point-like, so that J is also a function of magnetic field. This is evident in the data

presented in chapter three.

In addition to these fundamental limitations there are several ways in which samples can be disordered, inadvertently, or intentionally as a means to understand real systems such as random magnets or granular superconductors. Consider, for example, a slight generalization of (1.13),

$$H = -\sum_{<i,j>} J_{ij} \cos(\theta_i - \theta_j - \psi_{ij}) \qquad (1.16),$$

where we now allow the Josephson energy to vary from junction to junction. We refer to this as *bond disorder* because the strengths of the *bonds* (the junctions) between *sites* (the superconducting islands) vary. This kind of disorder is inevitable in any real array since it is impossible to fabricate samples with all junctions identical. It can been shown theoretically that "weak" bond disorder is irrelevant, and does not affect the critical behavior of the system (Harris, 1974), while strong enough disorder *can* affect critical exponents. The critical amount of disorder is not known for this system.

Another type of disorder is site or bond dilution, where superconducting islands or junctions are removed at random from the lattice. The case of site disorder has been studied theoretically (John and Lubensky, 1985), and it has been shown that weak dilution, where only a few percent of the sites are removed, is irrelevant to the critical behavior. On the other hand these authors showed that strong dilution, where the sample approaches the percolation threshold, can have a dramatic effect, possibly leading to glassy behavior, characterized by extremely slow relaxation to equilibrium. They also showed that in this limit one can formally have a *negative* spin wave stiffness. The experimental consequences of this are unknown, and this is probably the most intriguing experiment remaining to be done on arrays. Davidson and Tsuei (1981) attempted to study *bond* dilution in a tunnel junction array by destroying junctions at random with a laser.

Unfortunately the properties of the remaining junctions were so drastically modified by this process that their results could not easily be interpreted.

The third type of disorder one can introduce into the Hamiltonian (1.13) is randomness in the ψ_{ij}'s. The natural way to achieve this is to randomize the positions of the superconducting sites, as illustrated in Fig. 1.5. Clearly this leads to randomness in the plaquette areas (with correlations up to second-nearest neighbor plaquettes) and therefore to randomness in the frustration f, giving an XY model with non-uniform frustration. This kind of disorder is called *positional disorder* and is the main topic of this work.

We now review the most important results of the theoretical work on arrays with positional disorder. Our goal is not to describe the theory in detail, but simply to justify the main ideas, and describe the results.

1.6 Arrays with positional disorder

Granato and Kosterlitz (GK) (1986b) have considered an array with positional disorder as illustrated in Fig. 1.5, where the superconducting sites are diplaced from their average positions **r** by a random amount $\mathbf{u_r}$. They assumed a gaussian probability density per unit area for $\mathbf{u_r}$,

$$P(\mathbf{u_r}) = \frac{1}{2\pi\Delta^2} \exp\left(\frac{-\left|\mathbf{u_r}\right|^2}{2\Delta^2}\right) \tag{1.17}$$

where the parameter Δ thus defined quantifies the amount of positional disorder.

One can separate the Hamiltonian (1.13) into spin wave and vortex contributions, $H = H_{SW} + H_V$, where H_{SW} does not affect the critical behavior other than to change T_c (Ohta and Jasnow, 1979). As shown by José *et al.* (1977) one can transform the vortex
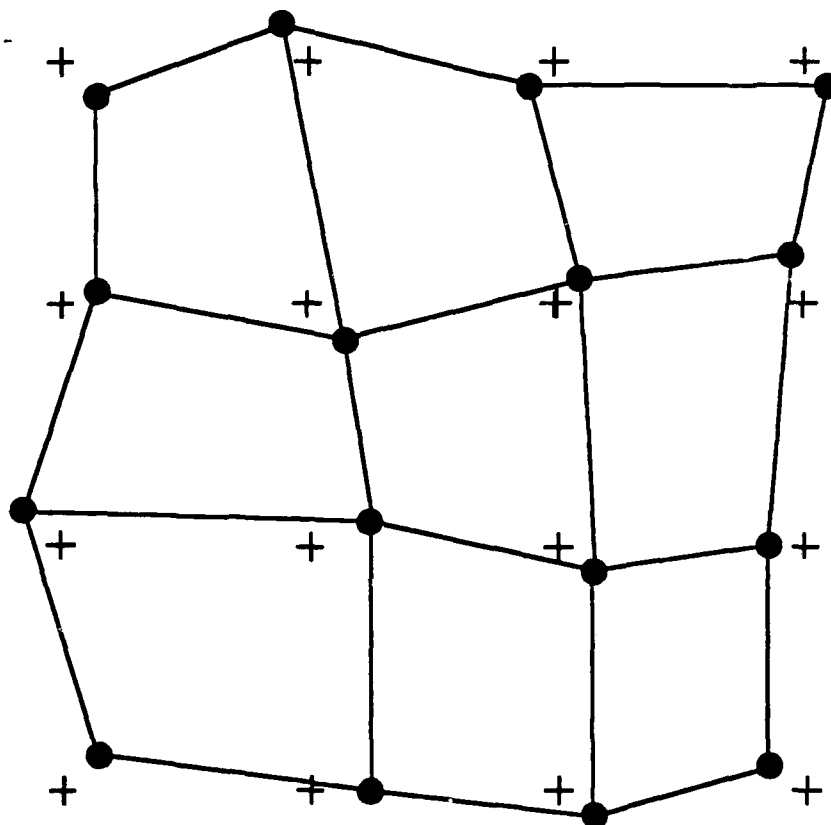
Figure 1.5   Schematic diagram of a junction array with positional disorder. Crosses mark the undisplaced positions and dark circles the actual positions of the superconducting islands.

part H_V into a sum over variables on a dual lattice, whose sites $\mathbf{R}_{ij}$ are at the centers of the plaquettes of the original lattice. This is not unreasonable since the vortices inhabit plaquettes rather than superconducting sites. Considering only the vortex contribution, one can write the temperature-reduced Hamiltonian $H/k_B T$ as

$$\frac{H}{k_B T} = 2\pi^2 K \sum_{\mathbf{R} \neq \mathbf{R}'} (M_\mathbf{R} - f_\mathbf{R}) \, G(\mathbf{R} - \mathbf{R}') \, (M_\mathbf{R} - f_\mathbf{R}') \qquad (1.18),$$

where $K = J/k_B T$, and $f_\mathbf{R}$ is the flux in the plaquette at $\mathbf{R}$. The $M_\mathbf{R}$ are integers analogous to m in (1.15), and obey the neutrality condition $\sum_\mathbf{R} (M_\mathbf{R} - f_\mathbf{R}) = 0$. The lattice Green's function $G(\mathbf{R} - \mathbf{R}')$ is given by (Spitzer, 1964)

$$G(\mathbf{R} - \mathbf{R}') = \frac{1}{2\pi} \log\left(\frac{|\mathbf{R} - \mathbf{R}'|}{s}\right) + \frac{c}{2\pi} \qquad (1.19),$$

where s is the vortex core size (in an array, the lattice parameter), $c = ((3/2)\log 2 + \gamma)$ $= 1.62... \approx \pi/2$ (Kosterlitz and Thouless, 1973) is a constant related to the chemical potential of a single vortex, and γ is Euler's constant. The form of the Hamiltonian in (1.18) explicitly shows the vortices to be equivalent to a set of charges $q \propto \sqrt{J} \cdot (M_\mathbf{R} - f_\mathbf{R})$, interacting through a logarithmic potential. This is the so-called "Coulomb gas analogy" for the XY model.

In the continuum limit, $s \to 0$, one does not distinguish between the original and dual lattices, and the area, $A_\mathbf{R}$, of a plaquette at $\mathbf{R}$ can be evaluated to lowest order in the displacements $\mathbf{u}_\mathbf{r} \to \mathbf{u}_\mathbf{R}$ as $A_\mathbf{R} = A_o(1 + \nabla_\mathbf{R} \cdot \mathbf{u}_\mathbf{R})$, where A_o is the area of an undisplaced plaquette. This means that the frustration $f_\mathbf{R}$ is given, to lowest order in the displacements, by

$$f_\mathbf{R} = f_o(1 + \nabla_\mathbf{R} \cdot \mathbf{u}_\mathbf{R}) \qquad (1.20),$$

17

where f_o is the *average* flux per plaquette. Substituting (1.20) into the Hamiltonian (1.18) one has

$$\frac{H}{k_B T} = 2\pi^2 K \sum_{R \neq R'} (M_R - f_o - f_o \nabla_R \cdot u_R) \, G(R-R') \, (M_{R'} - f_o - f_o \nabla_{R'} \cdot u_{R'})$$

$$= \; 2\pi^2 K \sum_{R \neq R'} (M_R - f_o) \, G(R-R') \, (M_{R'} - f_o)$$

$$- 2\pi^2 K f_o \sum_{R \neq R'} \nabla_R \cdot u_R \, G(R-R') \, (M_{R'} - f_o)$$

$$- 2\pi^2 K f_o \sum_{R \neq R'} (M_R - f_o) \, G(R-R') \, \nabla_{R'} \cdot u_{R'}$$

$$= \; 2\pi^2 K \sum_{R \neq R'} (M_R - f_o) \, G(R-R') \, (M_{R'} - f_o)$$

$$- 4\pi^2 K f_o \sum_{R'} \int \frac{dR}{s^2} \nabla_R \cdot u_R \, G(R-R') \, (M_{R'} - f_o) \tag{1.21},$$

where the integral over R is understood to have a short range cutoff at $|R-R'| = s$. Substituting the expression (1.19) for $G(R-R')$ into (1.21) we obtain

$$\frac{H}{k_B T} \; = \; \pi K \sum_{R \neq R'} (M_R - f_o) \, \log\!\left(\frac{|R-R'|}{s} \right) (M_{R'} - f_o)$$

$$+ \pi c K \sum_{R \neq R'} (M_R - f_o) \, (M_{R'} - f_o)$$

$$- 2\pi K f_o \sum_{R'} \int \frac{dR}{s^2} \nabla_R \cdot u_R \, \log\!\left(\frac{|R-R'|}{s} \right) (M_{R'} - f_o)$$

$$- 2\pi K f_o \sum_{R'} \int \frac{dR}{s^2} \nabla_R \cdot u_R \, (M_{R'} - f_o) \tag{1.22}.$$

18

Because of the neutrality condition $\sum_{\mathbf{R}}(M_{\mathbf{R}}-f_{\mathbf{R}}) = \sum_{\mathbf{R}}(M_{\mathbf{R}}-f_o) = 0$ the fourth term in (1.22) is zero, while the second term simplifies as follows:

$$\sum_{\mathbf{R}\neq\mathbf{R'}} (M_{\mathbf{R}}-f_o)(M_{\mathbf{R'}}-f_o) =$$
$$\sum_{\mathbf{R},\mathbf{R'}} (M_{\mathbf{R}}-f_o)(M_{\mathbf{R'}}-f_o) - \sum_{\mathbf{R}} (M_{\mathbf{R}}-f_o)^2$$
$$= -\sum_{\mathbf{R}} (M_{\mathbf{R}}-f_o)^2$$

The Hamiltonian thus reduces to

$$\frac{H}{k_B T} = \pi K \sum_{\mathbf{R}\neq\mathbf{R'}} (M_{\mathbf{R}}-f_o) \log\left(\frac{|\mathbf{R}-\mathbf{R'}|}{s}\right)(M_{\mathbf{R'}}-f_o)$$
$$-\pi c K \sum_{\mathbf{R}} (M_{\mathbf{R}}-f_o)^2$$
$$-2\pi K f_o \sum_{\mathbf{R'}} \int \frac{d\mathbf{R}}{s^2} \nabla_{\mathbf{R}}\cdot\mathbf{u}_{\mathbf{R}} \log\left(\frac{|\mathbf{R}-\mathbf{R'}|}{s}\right)(M_{\mathbf{R'}}-f_o) \quad (1.23)$$

Finally, an integration by parts in the last term gives

$$\frac{H}{k_B T} = \pi K_o \sum_{\mathbf{R}\neq\mathbf{R'}} (M_{\mathbf{R}}-f_o) \log\left(\frac{|\mathbf{R}-\mathbf{R'}|}{s}\right)(M_{\mathbf{R'}}-f_o)$$
$$+ \log y_o \sum_{\mathbf{R}} (M_{\mathbf{R}}-f_o)^2$$
$$+2\pi K_o \sum_{\mathbf{R'}} \int \frac{d\mathbf{R}}{s^2} f_o \mathbf{u}_{\mathbf{R}}\cdot\frac{(\mathbf{R}-\mathbf{R'})}{|\mathbf{R}-\mathbf{R'}|^2}(M_{\mathbf{R'}}-f_o) \quad (1.24),$$

where, for the discussion in the next section, we have added a subscript o to K, to indicate that it is the unrenormalized stiffness, and have defined $y_o \equiv \exp(-\pi c K_o) \approx \exp(-\pi^2 K_o/2)$.

The quantity y_o is called the vortex fugacity, while K_o will ultimately be identified with the temperature-reduced spin wave stiffness, and is a measure of the vortex interaction strength or the effective superfluid density. The Hamiltonian (1.24) can be viewed as describing a gas of fractional charges $q \propto (M_R - f_o)$, interacting with a quenched distribution of dipoles $p_R \propto f_o u_R$. For the case of f_o an integer one has a gas of *integral* charges perturbed by a random dipole distribution. The first term in (1.24) is the vortex-vortex interaction, the second term the vortex self-energy, and the third the vortex-dipole interaction.

$$\xrightarrow{\;\delta\;}$$

$$+f_o \delta/s \qquad \vdots \qquad -f_o \delta/s$$
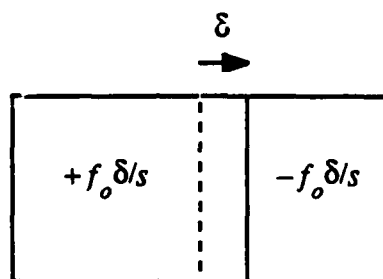
Figure 1.6 An example of an elementary "dipole".

The nature of these quenched dipoles can be understood by considering the pair of neighboring plaquettes illustrated in Fig. 1.6, where one bond has been moved a distance δ to one side. This produces an area increase (decrease) in the left (right) plaquette proportional to δ, and thus, in the Coulomb gas analogy, a pair of charges $\pm f_o \delta/s$, constituting an electric dipole of strength $f_o \delta$ (to lowest order in δ).

The problem of a Coulomb gas of *integral* charges perturbed by a random background of dipoles has been studied in another context by Rubinstein, Shraiman, and Nelson (RSN) (1983). We now describe the results of their analysis, couched in terms of junction arrays with positional disorder.

1.7 The Coulomb gas in a random background of dipoles

In the Hamiltonian (1.24) the stiffness K is a measure of the vortex interaction strength, and in an array is proportional to the superfluid density, divided by temperature, while y, the vortex fugacity, is related to the density of vortices (Kosterlitz and Thouless, 1973). For the pure case, with no disorder, KT demonstrated the length dependence of these quantities due to the screening of the vortex-vortex interaction by other *bound* vortex pairs. Considering only the first two terms in (1.24) they derived the recursion relations for K and y:

$$\frac{dK^{-1}(l)}{dl} = -4\pi^3 y^2(l) \tag{1.25a}$$

$$\frac{dy(l)}{dl} = \left[2 - \pi K(l) \right] y(l) \tag{1.25b}$$

where $l = \log(r/s)$, and r is the separation of the pair of vortices under consideration. These relations tell how the interaction of a pair of vortices of separation r is "renormalized" by other vortex pairs. The values of K and y in (1.24) are actually the "bare" or unrenormalized quantities $K_o = K(l=0) = J/k_B T$ and $y_o = y(l=0) \approx \exp(-\pi^2 K_o/2)$, and provide the initial conditions from which the renormalization in (1.25) begins.

The physical significance of the renormalization can be seen in the flows of (1.25) in the (K^{-1}, y) plane. Near $K=2/\pi$, (1.25) has the approximate solution

$$\left(\frac{2}{\pi} K^{-1} - 1 \right)^2 - 4\pi^2 y^2 = C(T) \tag{1.26}$$

where $C(T)$ turns out to be linear in T, $C(T) \approx C_o(1-T/T_c)$. The curves (1.26) are
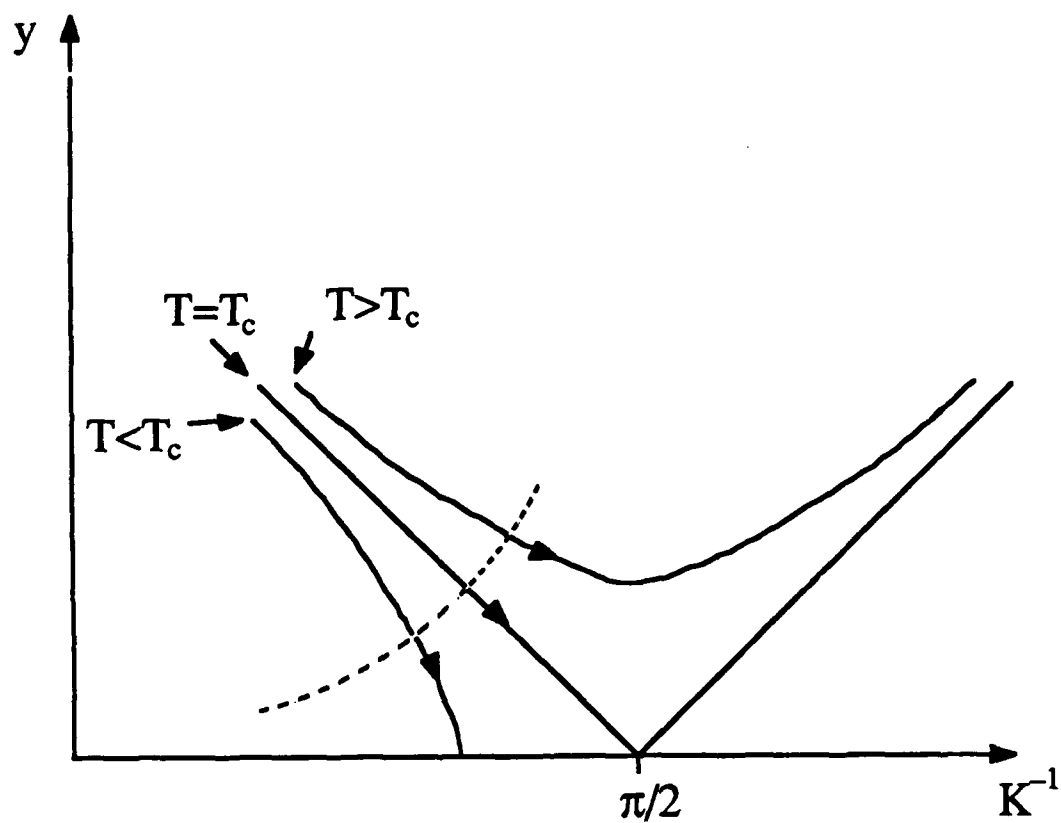
Figure 1.7   Renormalization group flows for the pure XY model. The dotted curve is the locus of initial conditions, while the arrow heads denote the direction in which the renormalization proceeds.

hyperbolas, three of which are sketched in Fig. 1.7, along with the curve of initial values $y_o \approx \exp(-\pi^2 K_o/2)$. The arrows mark the direction of increasing l, indicating the direction in which the renormalization proceeds. For $C > 0$ ($T < T_c$) the flows terminate on the line $y = 0$, at a finite value of K^{-1}, so that there are no vortex pairs of infinite separation (i.e. no free vortices), and the superfluid density $n_s \propto K \cdot T$ is finite. For $C < 0$ ($T > T_c$) the flows go towards $y = \infty$ and $K^{-1} = \infty$, so that vortices are unbound and the superfluid density is zero. The degenerate hyperbola with $C=0$ corresponds to $T = T_c$, where $K(l=\infty,T_c) \equiv K_R(T_c) = 2/\pi$, a universal value, independent of the details of the system (Nelson and Kosterlitz, 1977).

RSN have derived the recursion relations for the full Hamiltonian (1.24), taking account of the effect of the quenched random background of dipoles on the vortex-vortex interaction. Their results can be expressed in terms of arrays with positional disorder as

$$\frac{dK^{-1}(l)}{d} = -4\pi^3 y^2(l) \tag{1.27a}$$

$$\frac{dy(l)}{d} = y(l)\left[2 - \pi K(l) + 4\pi^3 f_o^2 \Delta^2 K^2(l)\right] \tag{1.27b},$$

where Δ is the disorder parameter defined by (1.17). When $f_o = 0$ (1.27) reduces to the result for the pure case (1.25). The quantity $f_o\Delta$ is effectively the measure of disorder, so that for a sample with fixed Δ one can tune the effective disorder by adjusting the magnetic field.

From (1.27b) we see that there are two special points $K_{\pm}^{-1}$ where the eigenvalue of y vanishes,

$$K_{\pm}^{-1} = \frac{\pi}{4}\left[1 \pm (1 - 32\pi f_o^2 \Delta^2)^{\frac{1}{2}}\right] \tag{1.28}$$

For K near K_+ (1.27b) simplifies to

$$\frac{dy(l)}{d} = \text{const.} \cdot (K^{-1} - K_+^{-1}) \, y(l)$$

With (1.27a) this gives

$$\frac{dy}{dK^{-1}} = \text{const.} \cdot \frac{(K^{-1} - K_+^{-1})}{y} \quad ,$$

whose solutions are hyperbolas, as was the case for the pure system shown in Fig. 1.7, but centered at $K^{-1} = K_+^{-1}$ instead of $K^{-1} = \pi/2$. For K near K_- one has

$$\frac{dy}{dK^{-1}} = -\text{const.} \cdot \frac{(K^{-1} - K_-^{-1})}{y}$$

so that the Hamiltonian flows are elliptical near K_-.

The Hamiltonian flows are sketched in Fig. 1.8, along with the line of initial conditions $y \approx \exp(-\pi^2 J/2 k_B T)$. The bold line shows a special trajectory which leaves the $y = 0$ fixed line at K_o^{-1} and terminates exactly at K_+^{-1}. The flows inside this boundary iterate to $y(l=\infty) = 0$, and $K^{-1}(l=\infty)$ finite, so that there are no free vortices and the stiffness is finite, just as for $T < T_c$ in the ordered array. This region is characterized by algebraic decay of correlations (1.4), or QLRC. Outside this region all flows lead to $y = \infty$ and $K^{-1} = \infty$ as $l \to \infty$, so that vortices are unbound and the *fully renormalized* stiffness $K_R = K(l=\infty)$ is zero. Actually the recursion relations (1.27) were derived using a perturbation expansion in y, so that they are not valid as $y \to \infty$, but it can be shown that one can integrate out to a finite value of l, still at small y, and then use a high-temperature
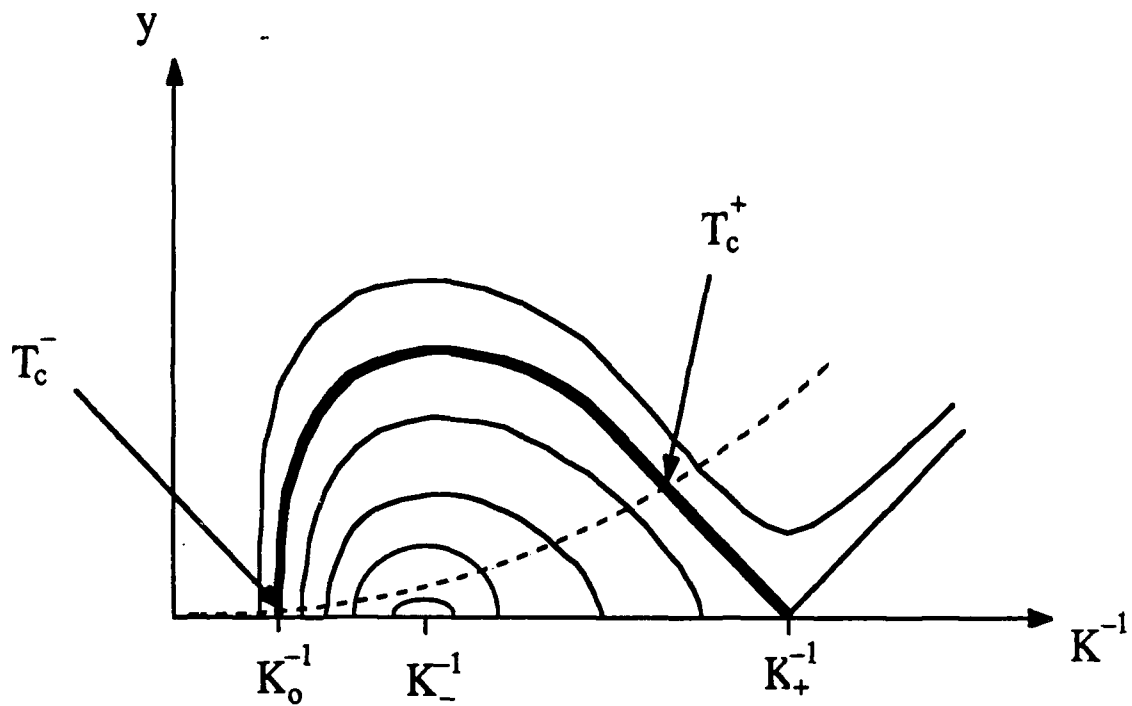
Figure 1.8   Renormalization group flows for an array with positional disorder. Flows
inside the critical trajectroy (dark boundary) terminate on the critical line $y=0$,
where there are no free vortices, while those outside diverge towards $y=\infty$.
There are two vortex-unbinding transitions, T_c^+ and T_c^-, the two points where
the critical trajectory intersects the line of initial conditions (dashed line).

Debye-Hückel approximation (Rubinstein, Shraiman, and Nelson, 1983). In this way one can rigorously show that correlations decay exponentially with the same length ξ_+ (1.11) as in the pure case.

Evidently there are now two transition temperatures, $T_c^-(f_o)$ and $T_c^+(f_o)$, as indicated in Fig. 1.8, at the two points where the locus of initial conditions intersects the critical trajectory (the dark line in Fig. 1.8). Below $T_c^-(f_o)$ the quenched dipoles weaken the interaction between the mobile vortices, so that some of the vortices are unbound, and there is no QLRC. For $T_c^-(f_o) < T < T_c^+(f_o)$, the increased density of mobile vortices is sufficient to screen the quenched dipoles, so that all of the vortices are bound. Finally, for $T > T_c^+(f_o)$, the vortices are thermally unbound, as in a uniform array.

From (1.28) it is also evident that, for a sample with fixed Δ, the special values $K_\pm^{-1}$ merge when f_o reaches a critical value f_c given by

$$f_c = \frac{1}{\sqrt{32\pi}} \frac{1}{\Delta} \approx \frac{0.10}{\Delta} \qquad (1.29)$$

For fields $f_o \geq f_c$ the ordered region (inside the dark line in Fig. 1.8) shrinks to zero, and QLRC is destroyed at all temperatures. From Fig. 1.8 it is also clear that the fully–renormalized stiffness, K_R, approaches K_+ at both transitions. In contrast to the uniform case this value is *not* universal, depending on the magnetic field, f_o. For $f_o = 0$, one has $K_+ = 2/\pi$, as for the uniform case, while for $f_o \to f_c$, K_+ approaches the value $4/\pi$. For a junction array this means that the IV exponent a should approach a value of 5 at both transitions, as $f_o \to f_c$, if the relationship between a and K (or a and n_s) is generalizable to finite fields.

1.8 Summary

In summary, there are two striking predictions for the behavior of a Josephson junction array with positional disorder, in a magnetic field such that the average number of flux quanta per plaquette, f_o, is an integer. First, there should be two vortex unbinding transitions, at $T_c^{\pm}(f_o)$, with the system exhibiting QLRC only for $T_c^{-}(f_o) < T < T_c^{+}(f_o)$. Second, for fields f_o greater than a critical value f_c, given by (1.29), the two transitions merge, and there is no QLRC at any temperature. These predictions are summarized in the qualitative phase diagram of Fig. 1.9, where the region marked S (for "superconducting") is characterized by QLRC, and the region marked N (for "normal") exhibits no long-range or quasi-long-range order. In addition, the magnitude of the superfluid jump at both transitions is nonuniversal, depending on the magnetic field f_o.
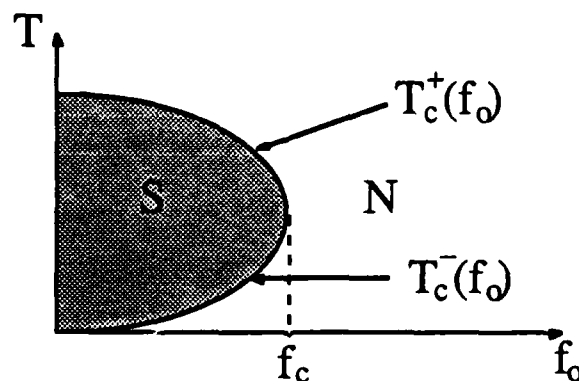
Figure 1.9   Schematic phase diagram for a 2D array with positional disorder. Vortex-unbinding transitions occur at $T_c^{+}(f_o)$ and $T_c^{-}(f_o)$. In the region marked S (for "superconducting") the sytem shows quasi-long-range phase coherence. In the region labeled N (for "normal") this phase coherence is destroyed.

CHAPTER TWO
EXPERIMENTAL DETAILS

2.1 Sample design

Josephson junction arrays have now been made by a number of groups, for studies of the KT transition and of the properties of a weak superconducting network in a magnetic field. Both tunnel junction (Voss and Webb, 1982: Van Wees *et al.*, 1987) and proximity effect arrays (Sanchez and Berchier, 1981: Resnick *et al.*, 1982: Abraham *et al.*, 1982: Tinkham *et al.*, 1983: Kimhi *et al.*, 1984: Leemann *et al.*, 1986: Brown and Garland, 1986) have been studied, but with proximity effect arrays in the majority due to their relative ease of fabrication. They can be fabricated with only one critical level of photolithography and therefore only one complex photomask.

The usual design is an array of superconducting islands, either on top of, or under, a continuous layer of normal metal (or a superconductor above its transition temperature). For a square array the simplest design is to have square superconducting islands, as illustrated in Fig. 2.1a. This design has the disadvantage that the junctions are extended, rather than point-like. The junction area is an appreciable fraction of the unit cell area, so that the junction critical current is strongly modulated by an applied magnetic field. Also, using this design it is impossible to introduce positional disorder without bond disorder, since displacing the islands also changes the junction lengths. Cross-shaped islands (see Fig. 2.1b) form smaller area junctions and allow the introduction of positional disorder without bond disorder. Figure 2.1c shows the natural generalization of this idea to the triangular lattice, where one has "asterisk" islands (Brown and Garland, 1986). This design is the basis for the Sierpinski gasket arrays, preliminary results from which will be
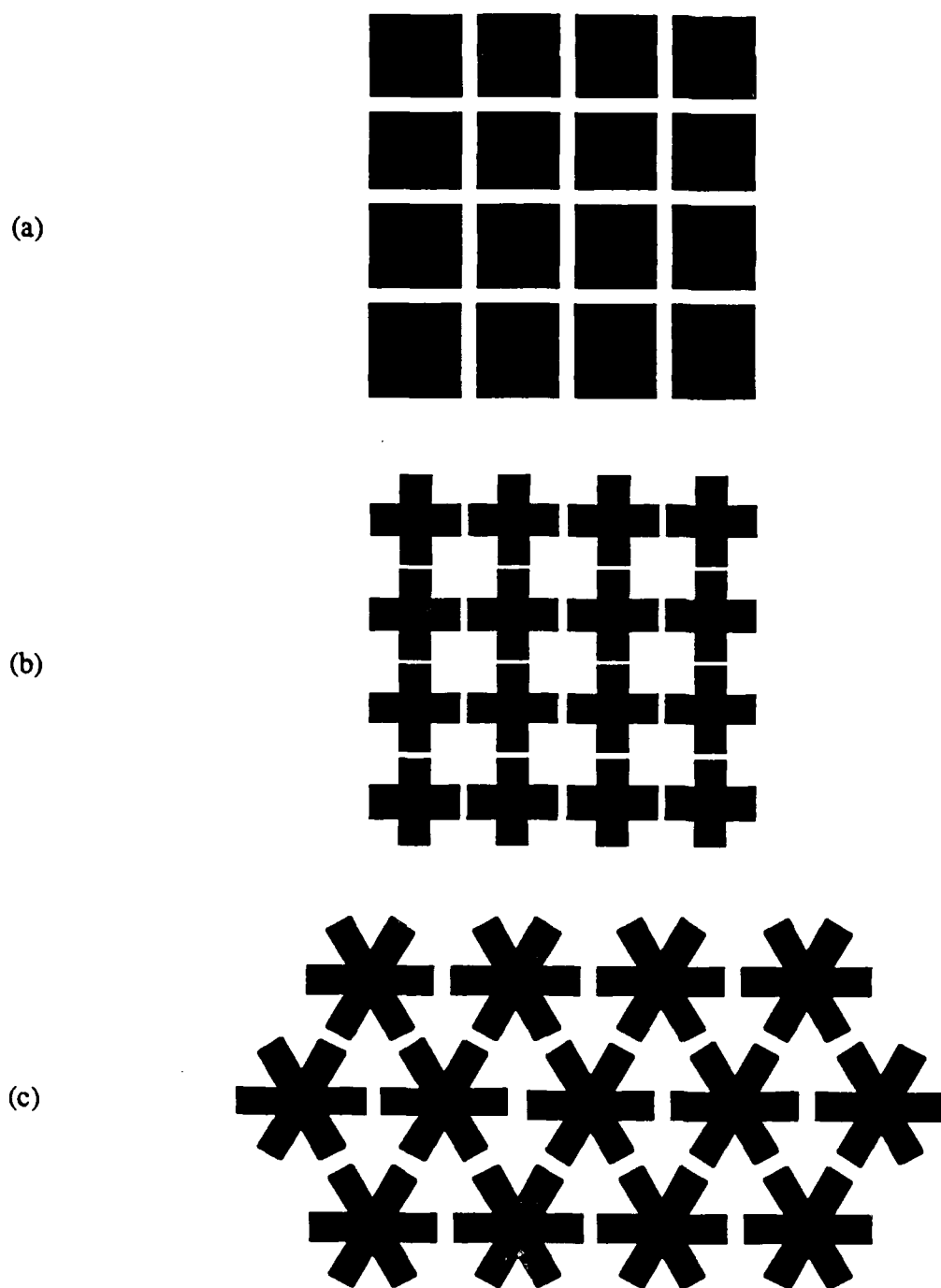
Figure 2.1 (a) Simple square proximity effect array, with square islands. (b) Square array with cross-shaped islands. (c) Generalization of (b) to a triangular lattice.
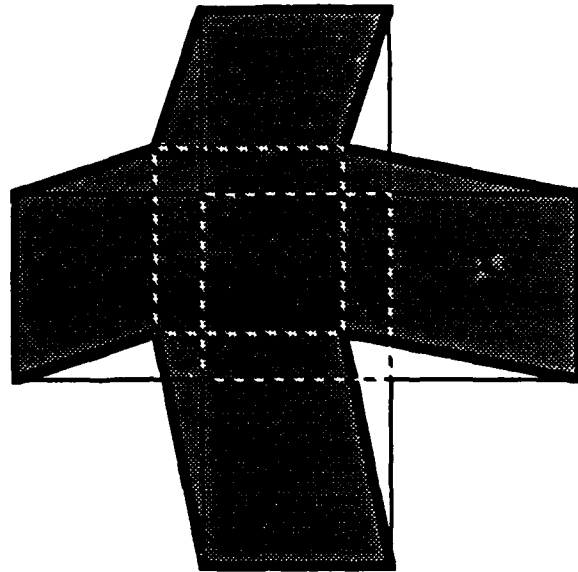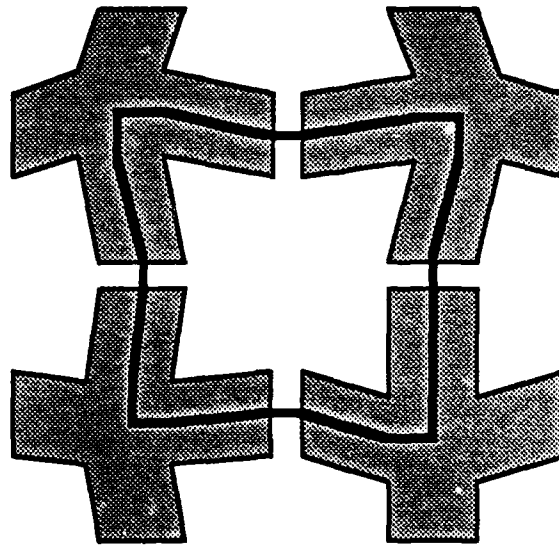
Figure 2.2 (a) Distortion of a superconducting island to introduce positional disorder. The center portion of the island (dotted outline) is displaced, while the tips of the cross are held fixed. (b) An example of a plaquette shape (bold outline) generated by this procedure.

discussed at the end of chapter three.

Given the cross design of Fig. 2.1b we can introduce controlled positional disorder, without bond disorder, by the scheme illustrated in Fig. 2.2a. We displace the center portion of each island (shown by the dotted outline in Fig. 2.2a) by a random amount $\mathbf{u}_{ij}$, determined by some probablilty distribution $P(\mathbf{u}_{ij})$, while leaving the tips of the crosses, and therefore the junctions, undisplaced. Since the junction lengths are preserved we do not change the critical currents and therefore introduce no deliberate bond disorder. Fig. 2.2b illustrates a typical plaquette formed by this scheme. The dotted outline follows the path of strongest superconductivity, where the magnitude of the superconducting wave function is maximum. The plaquettes are quite different from those envisioned by GK (see Fig.1.5) because the *junctions* are constrained to be on a regular lattice, rather than simply falling on a straight line between the centers of neighboring sites. This difference actually turns out to be unimportant, as will be discussed below.

The finite width of the superconducting crosses clearly imposes a limit on how large a positional displacement one can have, and still leave a well-formed island. Clearly, if the center of the island is moved far enough, the arms of the cross will be "pinched off". The absolute maximum displacement, as a fraction of the lattice parameter a, is $(a - d - w)/2a$, where d is the length of the junction, and w its width. For our samples we have $a \approx 13.5$ μm, $d \approx 2$ μm, and $w \approx 3.75$ μm, leading to a maximum displacement of approximately 30%. Even for somewhat smaller displacements limitations in the mask making procedure can lead to a decrease in the junction width when the displacement is close to 30%. This leads to weak bond disorder -- weak in the sense that changes in w lead to *linear* changes in i_c, as compared to changes in d, which give *exponential* changes in i_c. For these reasons we have used a *uniform* distribution of site displacements, with half-width Δ^*,

$$P(u_{ij}^x) = P(u_{ij}^y) = \begin{cases} \dfrac{1}{2\Delta^*} & -\Delta^* < u_{ij}^x, u_{ij}^y < \Delta^* \\ 0 & \text{otherwise} \end{cases} \qquad (2.1)$$

and have, in practice, limited Δ^* to 20% of the lattice parameter. In particular, we have made samples with $\Delta^* = 0.20, 0.15, 0.10, 0.05$, and nominally zero.

In order to compare our results with theory, in chapter three, we need to relate our disorder parameter Δ^*, which is the half-width of a *uniform* distribution of site displacements, to the parameter Δ used in the theory of GK and RSN, which is the width of a *gaussian* distribution of site displacements. In order to do this we recall that, from chapter one, the strength of the disorder is characterized by the strengths of the dipoles $\mathbf{p_r}$, with $\mathbf{p_r} \propto f_o \, \mathbf{u_r}$. Since the mean value of $\mathbf{p_r}$ is zero for both distributions, we compare the root-mean-square values for the two types of disorder. Since the rms width of a uniform distribution of half-width Δ^* is $2\Delta^*/\sqrt{12} = \Delta^*/\sqrt{3}$, while that of the gaussian distribution is simply Δ, consideration of only this first non-zero moment for each distribution leads to the relation

$$\Delta \approx \frac{\Delta^*}{\sqrt{3}} \qquad ,$$

relating the two disorder parameters, to lowest order. In chapter four we will show that this relation is verified quite well in our Monte Carlo simulations, which can consider both types of disorder.

2.2 Sample Fabrication

In previous work in this group (Abraham *et al.*, 1982: Tinkham *et al.*, 1983), large
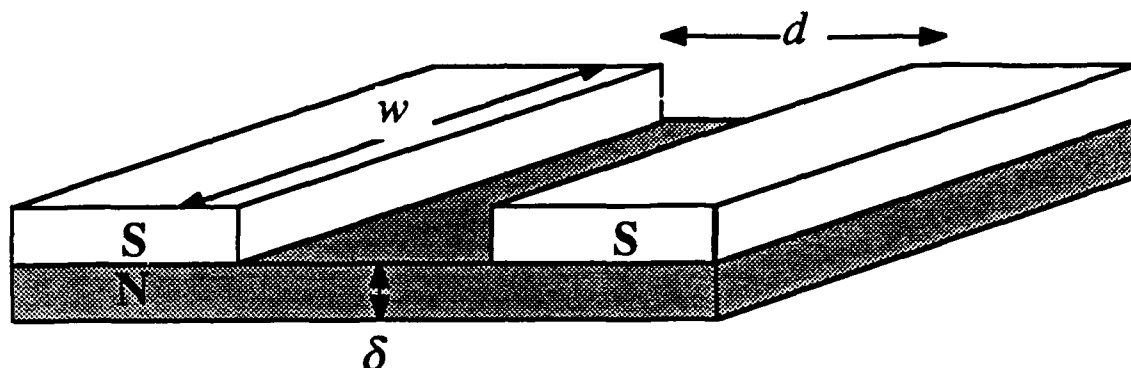
Figure 2.3   Schematic diagram of a bridge-type SNS junction, of the type in our arrays, defining the various lengths of interest.

square arrays like those in Fig. 2.1a were fabricated without the aid of photolithography, by evaporating Pb through a fine Ni mesh, onto a continuous Cu film. The junction length, d, (see Fig. 2.3) was defined by the diameter of the mesh wire and was no smaller than 5 µm. Such long junctions were so weakly coupled that array transition temperatures tended to be lower than could be reached in a pumped ^{4}He cryostat. To increase the coupling strength the mesh was lifted above the surface of the Cu film by a Mylar spacer, so that the islands became "feathered", reducing the effective junction lengths. Unfortunately, the feathering tended to be non-uniform, often giving a gradient in coupling energy across the sample. This was sometimes quite noticeable under the optical microscope, and was probably responsible for the poor results of measurements of resistance vs. magnetic field. Such measurements generally showed few oscillations and little fine structure compared to the results of this work and results from other groups.

    To improve the quality of our samples we have turned to the use of photolithography. This not only improves the uniformity and reproducibility of the samples, but also allows

the fabrication of a wide variety of array geometries. We have generated masks using electron-beam lithography and then used such masks to define arrays using a photolithographic process. We now discuss some of the details of mask making, and then sample fabrication.

2.2.1 Mask making--Generalities

Electron-beam lithography has now become the most flexible method for producing masks, both for the semiconductor industry, and for research, and is gradually replacing the use of optical pattern-generators for this purpose. The e-beam writer offers several distinct advantages over the optical pattern-generator, including higher resolution (< 0.2 μm compared to 2 μm), the ability to expose arbitrary shapes, with lines at arbitrary angles, and the capability of reversing tone or inverting patterns in software.

Lacking a commercial e-beam writer (typical cost > $1,000,000), we have used a general-purpose scanning electron microscope (a Jeol JSM 35u), controlled by a microcomputer, with two 16-bit digital-to-analog converters to control the x and y position of the beam, and a single TTL output to control a beam blanker. The blanker switches off the beam when not writing, by rapidly deflecting the beam off the sample.

To minimize writing time we have used a technique known as "brushfire lithography", which allows the generation of a pattern by writing only its outline rather than exposing areas. A simple example will illustrate the technique.

Figure 2.4a shows a simple pattern consisting of a rectangle of Cr on a glass mask blank. The conventional technique is to coat a Cr-covered plate with e-beam sensitive

(a)

(b)
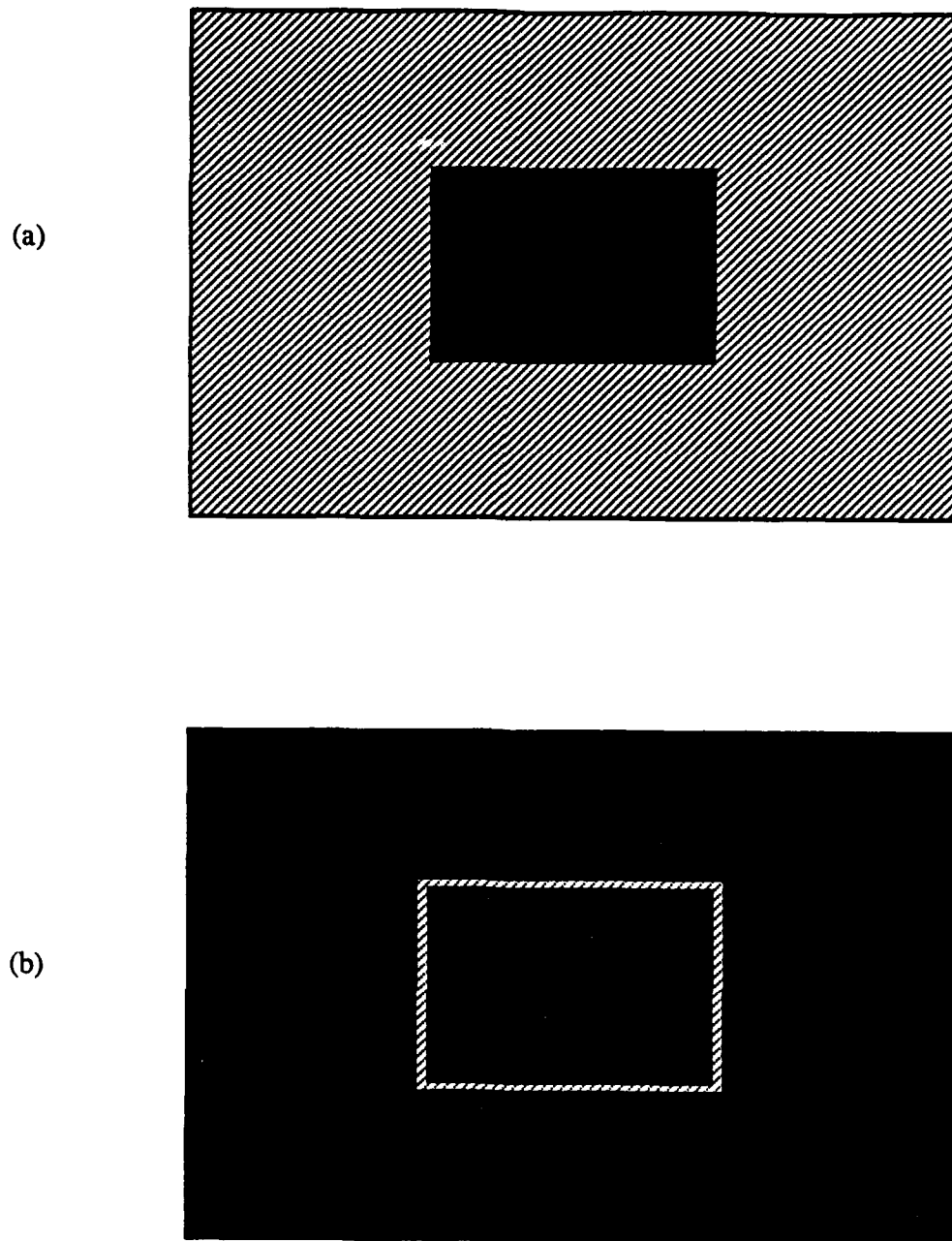
Figure 2.4 Comparison of areas to be exposed (hatched areas) to form a simple Cr rectangle using (a) conventioanl e-beam exposure, and (b) the brush fire technique.

resist and then expose the area where the Cr is to be removed, by rastering the beam across it. The resist is then removed from the exposed area by a chemical developer, and the Cr etched away with a chemical etch. The brushfire method produces the same pattern by exposing only the outline of the rectangle. By etching the Cr in this narrow "moat", as illustrated in Fig. 2.4b, the desired pattern is isolated from the surrounding Cr. After removing the resist, the mask is placed in a weak solution of HCl. Touching any point on the unwanted Cr with a piece of Al starts a chemical reaction which then propagates throughout all the contiguous Cr, thereby removing it, but preserving the area which is isolated by the moat. Obviously the technique is limited to "open" patterns, where there is a continuous path along which the reaction can propagate. The technique can be extended to patterns where a limited number of isolated Cr areas are to be removed, by selective deposition of Al "seeds" by photolithographic means. Using the brushfire technique we were able to write a mask for a 50×50 array in approximately 1 hour and 45 minutes, a short enough time that instability of the beam current was not a problem.

2.2.2 Mask making--Specifics

We started with a 2.5" $\times$ 2.5" $\times$ 0.060" Cr/CrOx coated mask plate, available from several suppliers (Electronic Materials Corp., Balzers, Hoya). The flatness specification was generally 2 μm ("Ultra" grade), with the exception of the EMC masks, which were 5 μm ("Master" grade). The blanks were coated with 6% polymethylmethacrylate (PMMA) in chlorobenzene (available from KTI), spun at 8000 rpm for 45 seconds, and baked for one hour at 180±5 °C. The resulting PMMA layer had a thickness of approximately 0.1 μm, according to data sheets provided by the Cornell Submicron Facility.

The resist was exposed in the SEM, at a magnification of 60 x, with a beam voltage of 25 kV, and a beam current of 90-100 pA, as measured by a Keithley electrometer. Exposure times were generally 1.2 msec/pixel, with a settling time (at the beginning of each line) of 16 msec. To allow the beam to stabilize before writing the pattern, we exposed a small rectangle (total exposure time ≈ 30 sec) close to the desired starting point. The microscope working distance was 15 mm and the aperture was number two.

The PMMA was developed for 45 sec in 1:3 methylisobutylketone:isopropanol (MIBK:IPA) and then inspected under the optical microscope. The goal was to ensure that all the exposed lines were fully developed at their centers, so that the Cr could be removed cleanly. Any residual resist would result in a Cr short, which would allow the brushfire reaction to propagate across the moat and remove the Cr which was to be preserved. To ensure complete development we alternately immersed the mask in MIBK:IPA for 10 additional seconds and inspected under the microscope, until all lines were clear.

To remove the Cr in the exposed lines the mask was immersed in a standard Cr etch (396 ml H_2O, 24 ml HNO_3, 63g cerrium ammonium nitrate) until a small test area, where the resist had been scraped away with a razor blade, appeared completely etched. After inspection the mask was further etched for 10-second intervals until all lines were clear of Cr. The resulting moats typically were 0.2 to 0.5 μm wide.

To ensure smooth propagation of the brushfire reaction it was *essential* that the PMMA be completely removed from the Cr surface. We found that solvents such as acetone and methylethylketone (MEK) left enough residual PMMA to inhibit the brushfire reaction or even stop it completely. Tests showed that even after several hours soaking in acetone there was enough PMMA residue to protect Cr from chemical etch. This residue was usually visible to the naked eye, making the Cr surface appear mottled.

The best method for PMMA removal turned out to be an RF oxygen plasma etch. This was performed in a small reactive-ion-etching chamber, in an O_2 pressure of 70-100 mtorr,

etching for about five minutes (although the resist was probably removed within the first minute). After this, tests showed that masks which had been coated with PMMA could be etched in Cr etch as well as could virgin masks, and, most importantly, the brushfire reaction was found to propagate smoothly through the Cr.

After the O_2 plasma cleaning we could perform the brushfire etch by immersing the mask in dilute HCl and touching the unwanted Cr with an Al pellet. We found that the etch could be started most easily by using a wire bonder to bond small hoops of Al wire in several locations around the perimeter of the mask, and then immersing the mask in a 2:1 solution of "concentrated" (37%) HCl in water, agitating by sharp blows with a tweezer to dislodge bubbles. Since preliminary tests had shown that the reaction was more easily started when the CrOx surface layer was thinner, we assume that the bonder punched the Al wire through the oxide layer and started the reaction in the Cr itself. As for the concentration of HCl, it was found that higher concentrations tended to cause excessive bubbling and that the bubbles clinging to the Cr would locally prevent etching. Lower concentrations simply made the brushfire reaction harder to start and maintain.

After rinsing and drying we now had the basic mask, consisting of an array of Cr islands on an otherwise blank field. Figure 2.5 shows sections of two masks, one for a uniform square array (a), and one for a disordered array with $\Delta^* = 0.10$ (b). Figure 2.6 shows another example -- a Sierpinski gasket array of sixth order. The masks show sharp features and excellent linewidth control.

To simplify sample fabrication we decided to make the electrical contact pads an integral part of the structure, rather that adding them subsequent to fabrication. To this end we used an emulsion mask to add Cr bus bars to the e-beam-generated masks, using photolithography in the Karl Süss aligner, depositing Cr, and lifting off. The resulting working mask, illustrated in Fig. 2.7, has Cr areas to define both the superconducting islands and the electrical contact pads. The pads are approximately 20 μm wide. Larger

$- 10\ \mu m$
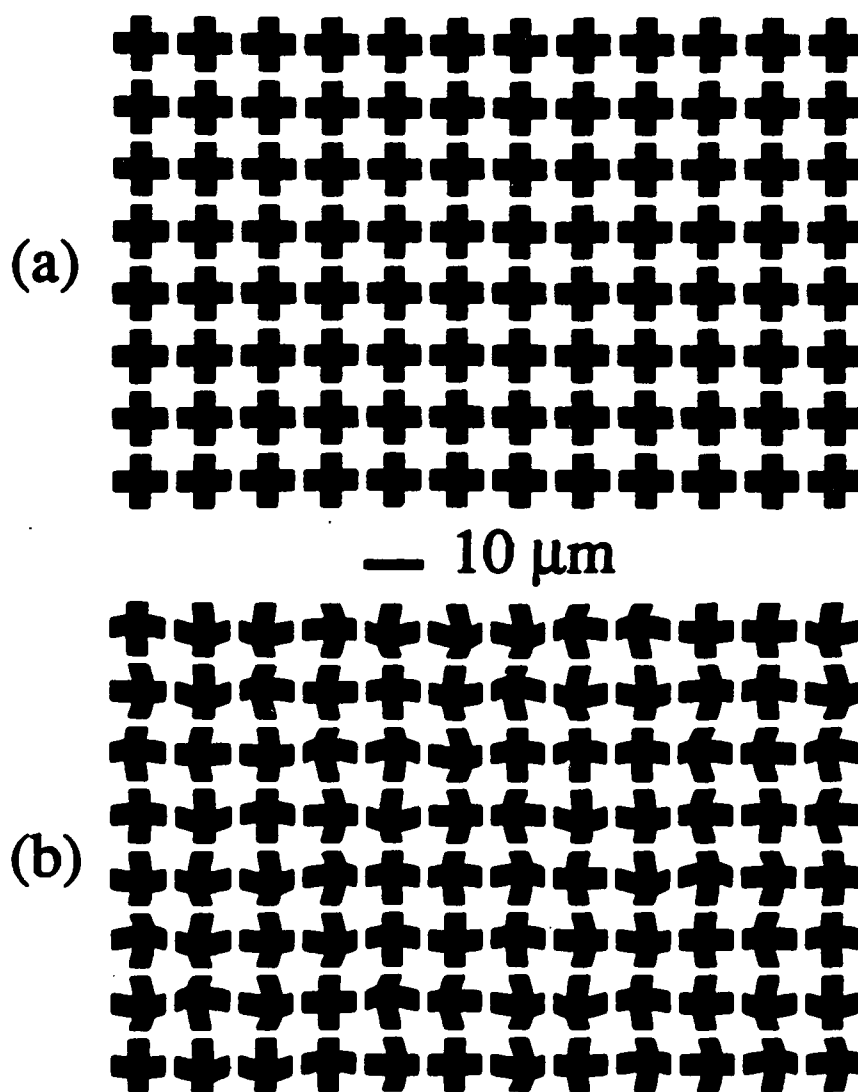
Figure 2.5 Sections of lithographic masks used to prepare arrays with (a) $\Delta^* \approx 0$ and (b) $\Delta^* = 0.10$.

10 μm

10 μm
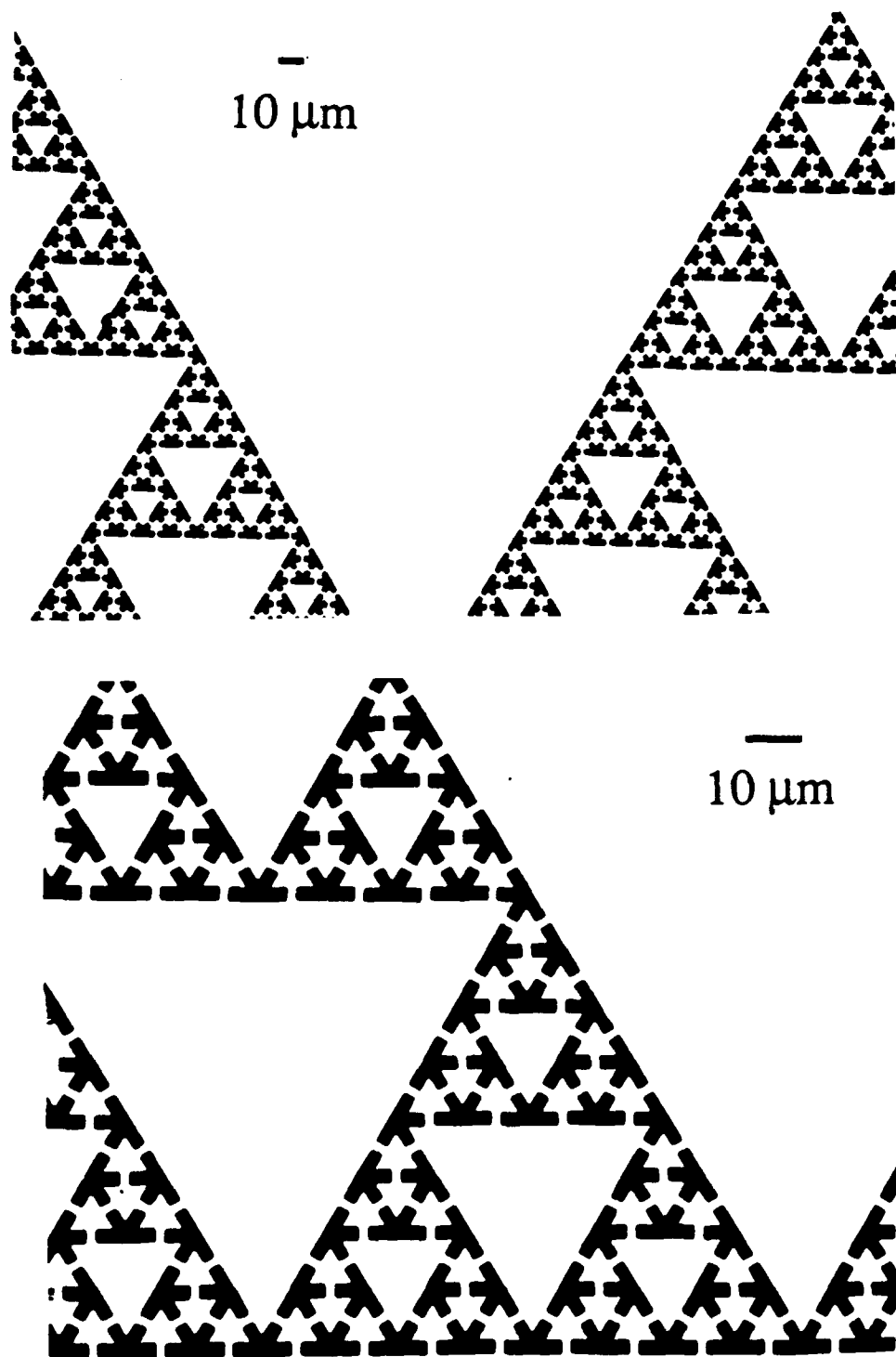
Figure 2.6   Sections of a lithographic mask used to produce Sierpinski gasket arrays of
proximity effect junctions.
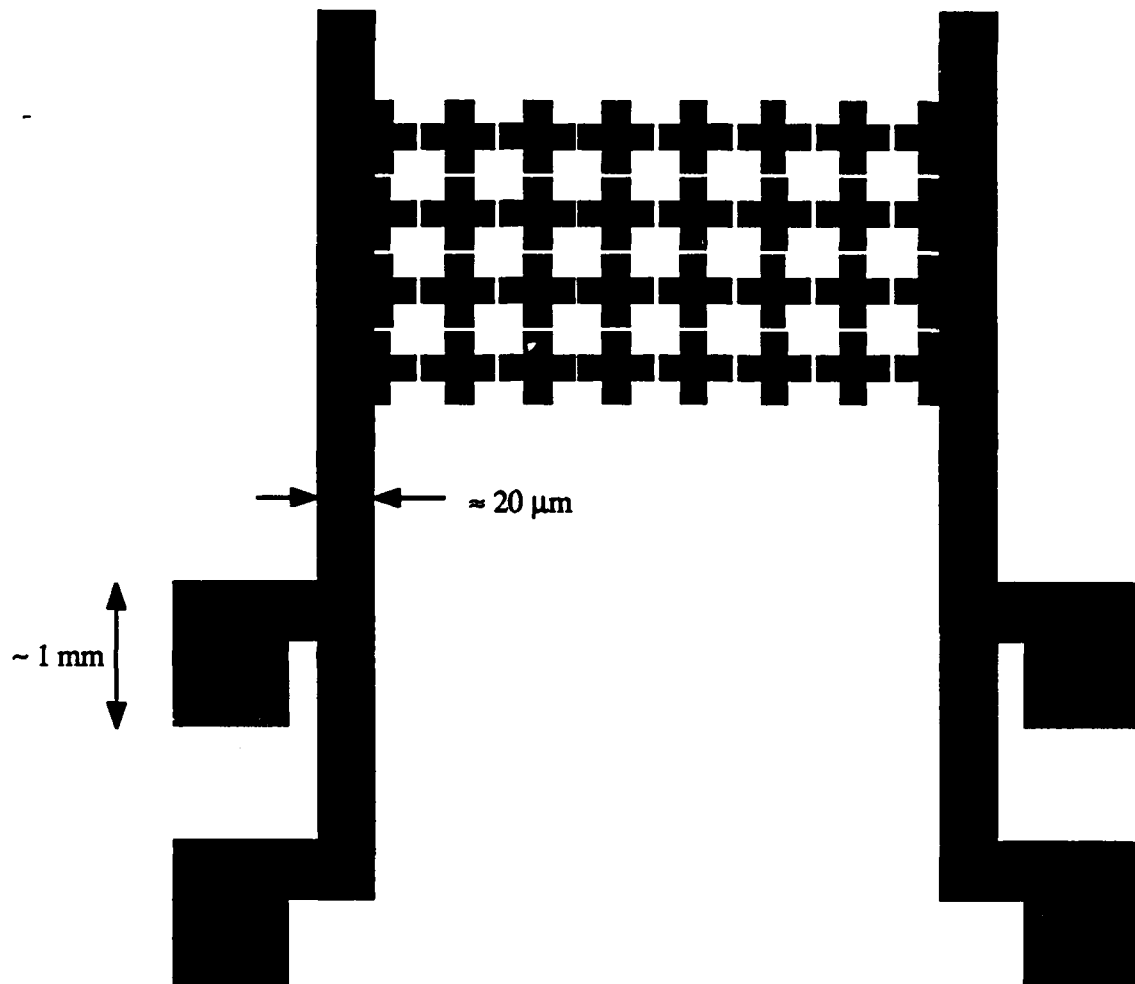
Figure 2.7   Schematic diagram of an e-beam-generated mask, with contact pad structures added by photolithography.

pads are known to cause flux trapping (Mooij, 1986), resulting in hysteresis in measurements of resistance vs. magnetic field, and might also contribute to magnetic field inhomogeneity due to their partial exclusion of flux.

It was also necessary to make a mask to define the shape of the Cu/Pb bilayer, so that the array would not be shunted by, for example, a normal metal strip. Given the array mask this was easily achieved by a two-stage process. First the array mask was copied in reverse tone, using Hunt HNR-120 negative resist, to give a mask with "windows" where the islands and pads would be. Second, this mask was duplicated using *positive* resist, but drastically overexposing (~ 1 minute), in the "soft contact" mode of the Karl Süss. This caused the islands to "spread out" and fill the entire array area, leaving a rectangle slightly larger (≈ 1 array period) than the actual array. Finally, a small square (~ 2 mm on a side) was etched in the Cr, to provide a test area on the sample which would *not* be covered with resist, and would allow us to determine when the ion-etching of the sample was complete.

2.2.3 Array Fabrication

The basic fabrication scheme was to prepare a bilayer of Cu and Pb on a sapphire substrate, pattern the bilayer with photoresist (PR) using the working mask, and remove unwanted Pb by ion-etching, as summarized in Fig. 2.8. We now discuss some of the details of this process. A step-by-step description can be found in the appendix.

The first step was to define the area of the bilayer, which consists of the array and the pads. We used a three-layer resist (PR-Al-PR) technique previously described by Danchi (1983), to form a resist structure with an undercut profile appropriate for liftoff. The resist was exposed using the bilayer mask described in the last section.

1) Deposit Cu-PbBi-Ge trilayer without breaking vacuum

Ge (100 Å)
PbBi(5%) (2000 - 4000 Å)
Cu (2500 - 4000 Å)
Sapphire substrate
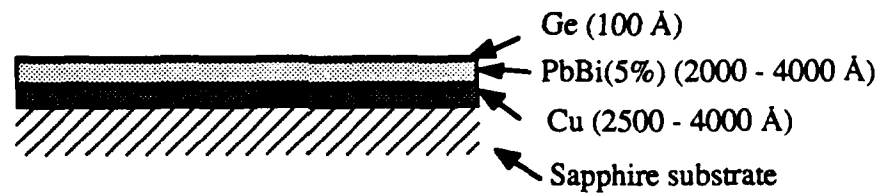
2) Deposit and pattern photoresist
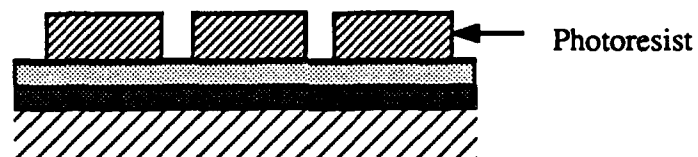
Photoresist

3) Ion etch exposed Ge and PbBi

Argon ions
(35 eV)
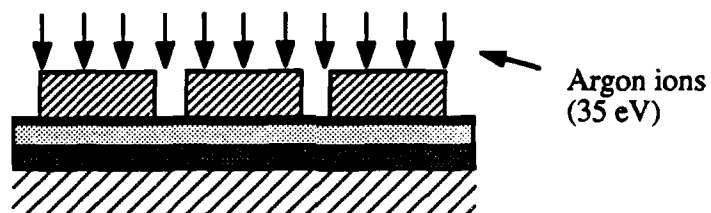
4) Remove photoresist
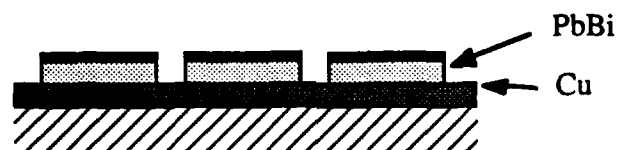
PbBi
Cu

Figure 2.8   Outline of array fabrication process.

Evaporation of the Cu/Pb bilayer was done in a diffusion-pumped thermal evaporator, at a base pressure of less than 2×10^{-7} torr. Separate power supplies were used to heat the Cu and Pb sources. This allowed us to have the materials evaporating concurrently, and to deposit Cu and then Pb in rapid succession by manipulating a three-way shutter, which could uncover either the Cu or Pb source, or neither. In addition we had a shutter to cover the sample stage while leaving the crystal thickness monitor uncovered, to set evaporation rates. After melting the Cu and setting a low evaporation rate we left the shutters closed for two minutes or more to allow lower melting point impurities to evaporate. We then evaporated typically 2500 - 4000 Å of Cu at 300 Å/sec or more, followed by 2000 - 4000 Å of Pb, typically at a rate of 100 Å/sec. The delay between Cu and Pb evaporations was a small fraction of a second, so that the Cu/Pb interface should be free of oxygen contamination.

After bilayer deposition we used an acetone spray to lift off the PR, leaving the bilayer pattern. We then deposted 100 Å of Ge over the entire substrate to protect the Pb from the PR developer in subsequent processing. (Microposit 351 PR developer etches Pb and Al, leaving pits in the surface). The sample was then coated with a layer of Shipley 1400-25 or -27 resist (of thickness 0.6 or 0.8 μm), and baked for 30 minutes at 90 °C. Using the working array mask we then exposed the resist-coated bilayer in the Karl Süss mask-aligner, usually for five seconds. We then developed in Microposit 351 developer (5:1 H_2O:Microposit) for 30 - 45 seconds, and post-baked for 30 minutes at 110 °C. This left PR protecting the Pb for the islands and pads, leaving the rest unprotected.

The next stage was to remove the unwanted Pb by ion-etching. We used a 3 cm Kauiman-type ion gun, from Commonwealth Scientific, with non-focussed grids, and Ar gas. Typical beam parameters are listed in table 2.1 We found that etching at beam voltages higher than 50 - 100 V would melt the Pb under the PR, causing it to agglomerate into large (~ 2 μm) grains, even if the substrate was water cooled. Using the parameters
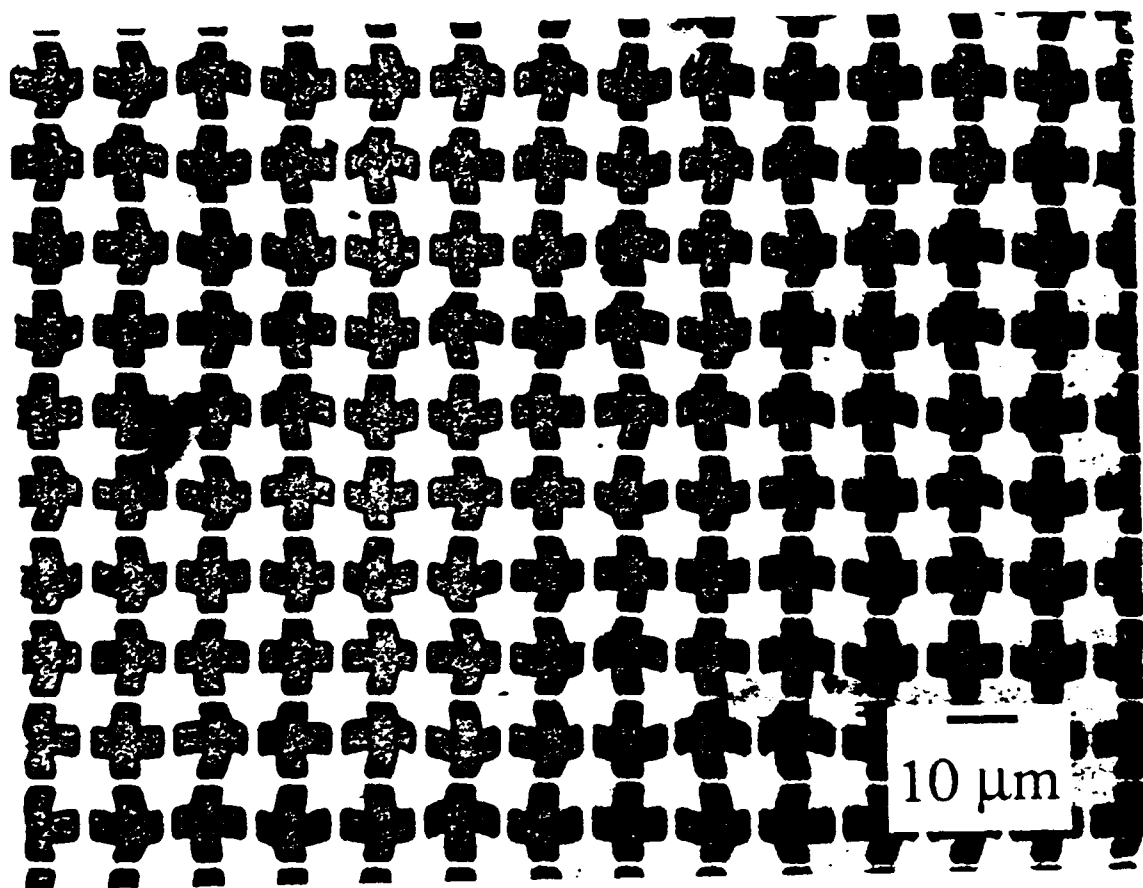
Figure 2.9 Optical micrograph of a completed disordered array, with $\Delta^*=0.10$.

of table 2.1 we obtained controlled etching at rates of 100 - 200 Å/minute. The abnormally high accelerator voltage ($V_A \approx 5\ V_B$, compared to the usual $V_A \sim 0.25\ V_B$ (Kaufman, 1984)) was necessary to avoid excessive ion impingement on the grids (accelerator currents > 10 mA), which causes excessive wear on the grids and power supply. During ion-etching the sample was observed through a glass window, and etching was stopped approximately two minutes after the large test area appeared to be clear of Pb.

Table 2.1 Ion etching parameters. Commonwealth 3 cm ion gun.

V_B	Beam voltage	35 V
I_B	Beam current	7-15 mA
V_D	Discharge voltage	35 V
I_D	Discharge current	0.5 - 2.0 A
V_A	Accelerator voltage	150 - 170 V
I_A	Accelerator current	< 9 mA
I_{NF}	Neutralizer filament current	< 15 A
I_E	Neutralizer emission current	$\approx I_B$

The final stage in sample fabrication was to remove the PR by squirting (and soaking, if necessary) with acetone. The resist on the islands was usually reluctant to dissolve, but that on the pads dissolved easily, allowing clean electrical contact for the measurements. Figure 2.9 shows an optical micrograph of a completed sample.

2.3   Measurement apparatus

When making transport measurements on Josephson junction arrays it is important to realize that the act of applying a transport current changes the properties of the system. For example, as discussed in chapter one, the KT transition is due to the *thermal* unbinding of vortices, but a measuring current can also unbind vortex pairs since it exerts opposite

forces on the vortices in a pair. If the number of current-induced free vortices is comparable to the number of thermally unbound vortices then the details of the phase transition can be obscured. Similarly, the complex modulation of array resistance by a perpendicular magnetic field is due to delicate phase coherence, which can be destroyed by large measuring currents. This sensitivity to measuring currents, along with the low normal resistance of proximity effect arrays (~ 1 mΩ), necessitates the measurement of quite small voltages. To this end we have used either a conventional lock-in amplifier or a SQUID to make all our measurements. Using a lock-in amplifier we have made ac measurements with sensitivity ~ 1 nV, while the SQUID has enabled us to make dc measurements with sensitivity ~ 1pV. In this section we briefly describe the main features of the cryogenic apparatus, and some of the details of the lock-in and SQUID measurement techniques.

The cryogenic probe used for the conventional measurements has been described in detail by Abraham (1983), and only its main features will be reviewed here. It has a vacuum can and a heater, so that the temperature of the sample can be raised above that of the He bath. Using a proportional-integral-derivative feedback system from a germanium resistance thermometer to the heater we could maintain temperature stability of approximately 1 mK, from the bath temperature up to approximately 15 K. The thermal circuit appeared to be well designed, with no appreciable thermal lag between thermometer and sample, and no evidence for differences in thermometer and sample temperatures in the steady state. A magnetic field perpendicular to the sample was provided by a home-made Cu solenoid, of length 10 cm and diameter 5.5 cm.

Because of concerns about magnetic field inhomogeneity some precautionary changes were made over the design described by Abraham. Our goal was to eliminate all unnecessary solder joints and other superconducting materials, which could distort the solenoid's magnetic field. The original Cu sample mount had two circular solder joints, of

diameter ≈ 3 cm, quite close to the sample. This piece was rebuilt, eliminating one joint entirely and replacing the other with a friction fit secured by brass screws. In addition, the original vacuum can, which was made of ordinary brass (which contains Pb to facilitate machining), and had solder joints at top and bottom, was replaced by a one-piece design made from Pb-free "Naval Brass". The full benefit of these measures would most likely be felt in measurements of larger arrays than those studied in this work, but we believe that the elimination of unnecessary solder joints is a prudent precaution in the design of cryogenic probes.

The design of the SQUID probe was also modified over that used previously by Lobb (1980). The sample voltage leads are Cu-clad Nb-Ti of approximately 40 gauge, instead of the Nb_3Sn tape used previously, while the current leads are #40 Cu. The Nb_3Sn tape had been uninsulated and therefore difficult to heat-sink without electrical shorts. The sample is mounted on a copper block which is connected to the He bath by a two-stage thermal link. This was intended to reduce thermal gradients and thereby reduce thermal emf's, which can be very significant in SQUID measurents. In practice the rig suffered from thermometry problems, probably due to insufficient heat-sinking of the thermometer and heater leads coming from room temperature. Compared to the conventional probe there was very little area for heat-sinking these leads. Because of these problems we made all our SQUID measurements with the sample and thermometer in the He bath, with temperature controlled by a Walker type pressure regulator. Since all our samples had T_c below 3.0 K this did not prove to be a limitation.

For conventional measurements we used a Princeton Applied Research model 140 lock-in amplifier with a model 119 1:100 step-up transformer. The lowest noise and greatest stability were obtained by operation at frequencies of order 400 Hz, usually 437 Hz, while operation at lower frequencies generally resulted in larger drift and somewhat greater noise. We had no difficulty measuring signals down to 1 nV, with noise
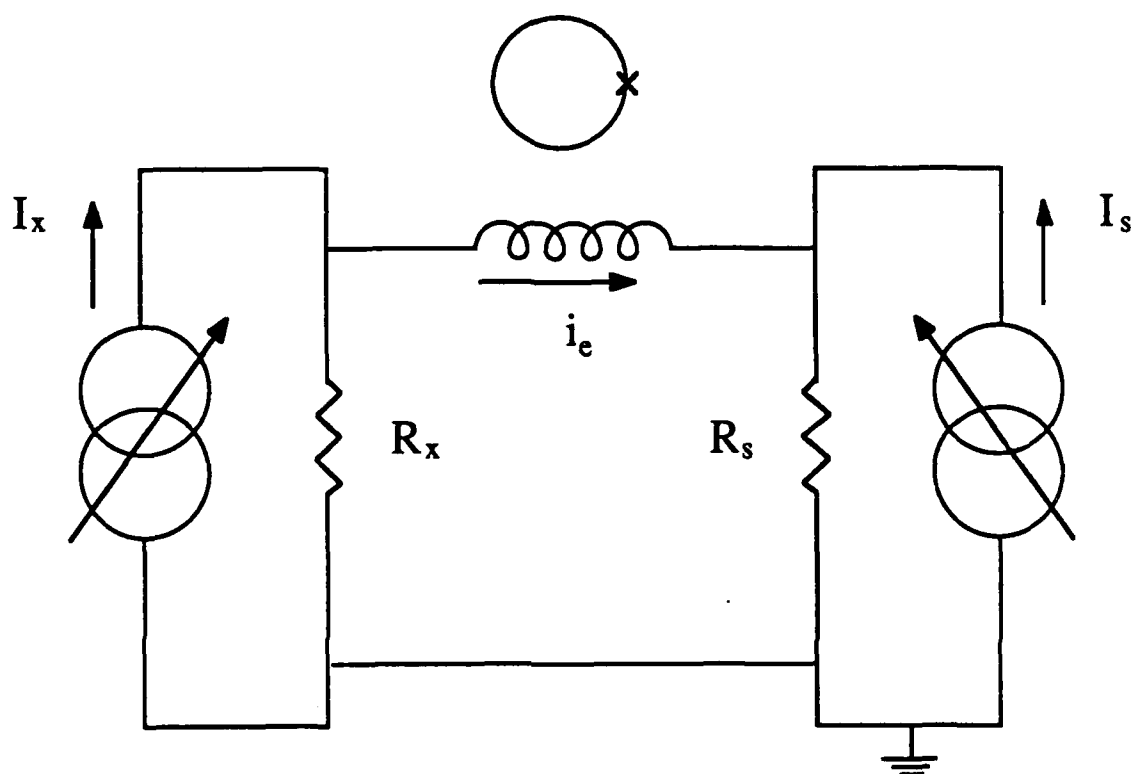
$$i_e = 0 \quad \Rightarrow \quad I_x R_x = I_s R_s$$

Figure 2.10 Schematic diagram of the bridge circuit used for SQ'JID measurements. R_x is the sample resistance and R_s is the standard resistor (3×10^{-5} Ω) in the S.H.E. PVP or MFP unit.

typically of order 0.2 nV with time constants of 3 secs or less. We usually set the Q of the signal channel to its maximum value of 100, for maximum noise rejection.

The SQUID measurements were made using a S.H.E. model 330 rf-SQUID as a null detector in a bridge circuit, as shown in Fig. 2.10. The sample, R_x, and its current supply are connected in parallel with a standard resistor, R_s, and current supply, with the SQUID magnetometer input between them. The procedure was to "reset" the SQUID with both currents set to zero, turn up the sample current to the desired level, and then adjust the standard's current supply until the bridge was "in balance" and the SQUID output was zero. In the balanced state the sample resistance is then determined by the condition $I_x R_x = I_s R_s$. To reduce noise, both current supplies were battery-powered, as were the voltmeters used to monitor currents. The sample current was monitored by a PAR 113 amplifier and then a voltmeter, which seemed to decrease the noise appreciably. Our standard resistor R_s was actually the $3 \times 10^{-5}\,\Omega$ resistor in the S.H.E. MFP or PVP unit, which is part of a voltmeter circuit. We did not use the voltmeter circuit as such because it was found to have uncontrollable offset currents ($\sim 1\,\mu A$), making it impossible to determine the absolute current level in the sample.

When the bridge is balanced the contact resistances between leads and sample are irrelevant, but these resistances can degrade the sensitivity of the measurement. Contact to the sample was usually made by pressed In contacts, with the tip of the Cu-clad Nb-Ti wire stripped of Cu before making contact. Ideally the contact should be completely superconducting but we found no noticeable difference between sensitivity above and below the In transition at 3.4 K. Our voltage sensitivity was approximately 1 pV.

CHAPTER THREE

EXPERIMENTAL RESULTS

3.1   Introduction

As discussed in chapters one and two, when making transport measurements on arrays it is important to use as small a current as possible. For example, to observe a discontinuous jump in the exponent $a(T)$, one must extract $a(T)$ from the local logarithmic slope, $(I/V)dV/dI$, at total sample currents, I, such that the current per junction, i, is small compared to the critical current of an isolated single junction, i_c. At higher current levels the discontinuity is smeared out and a falls to a value of one at a temperature higher than T_c. As discussed by Halperin and Nelson (1979) and Kadin *et al.* (1983), this can be understood in terms of a current-dependent length scale, $l_i \propto i_c/i$, corresponding to the separation of the tightest-bound vortex pairs which can be unbound by the current i. In effect, the length l_i provides an upper cutoff on the renormalization procedure described in chapter one, so that measurements do not probe the fully renormalized properties of the array.

Since the I-V characteristics are still non-linear above T_c, at currents $i >> i_c$, the extraction of a resistance for comparison with the theoretical result,

$$R(T) \; = \; R_o \exp\left[-2b/(T-T_c)^{\frac{1}{2}}\right] \qquad (1.12),$$

becomes problematic. If one defines resistance as V/I or dV/dI in this non-linear regime, one can see appreciable deviations from the behavior in (1.12) as one approaches T_c (Abraham *et al.*, 1982).

In this work we have studied small arrays, typically 50 × 50, compared to the

1000×1000 arrays in earlier work (Abraham *et al.*, 1982). This small size necessitates the use of smaller total sample current, I, to maintain comparable current per junction, i. Since the resistance is independent of size for a square sample the resulting voltages will be twenty times lower for the 50×50 samples, given the same resistivity. Given a fixed voltage sensitivity one must use currents, i, twenty times larger in our small arrays, exacerbating the finite current effects discussed above.

The point of this discussion is simply that our small arrays are not ideal systems for sudying the *details* of the KT transition. Therefore, any effects associated with positional disorder must be obvious enough that we do not have to rely on detailed analysis of, for example, the temperature dependence of the resistance, or subtle changes in the I-V exponent $a(T)$. Our measurements emphasize the destruction of oscillations in resistance vs. magnetic field, as a signature of the destruction of phase coherence in arrays with positional disorder. Most of this chapter is concerned with the analysis of such data. We also present some data on the critical current and resistance as a function of temperature. In the final section of this chapter we present some preliminary results from measurements on Sierpinski gasket arrays of Josephson junctions, which provide a realization of an XY model on a fractal lattice.

3.2 Critical currents

The critical current of a long, narrow, proximity effect or superconductor-normal-superconductor (SNS) junction is given by (De Gennes, 1964)

$$i_c(T) = i_c(0)\left(1-\frac{T}{T_{cs}}\right)^2 \exp\left(\frac{-d}{\xi_N(T)}\right) \tag{3.1}$$

where d is the length of the junction (see Fig. 2.3), and $\xi_N(T)$, the normal metal coherence length, is given by (Deutscher and De Gennes, 1969)

$$\xi_N(T) = \begin{cases} \left(\dfrac{\hbar v_F l}{6\pi k_B T}\right)^{\frac{1}{2}} & l << \xi_N(T) \quad \text{(3.2a)} \\[4mm] \dfrac{\hbar v_F}{2\pi k_B T} & l >> \xi_N(T) \quad \text{(3.2b),} \end{cases}$$

where v_F is the Fermi velocity and l the mean free path. By "long" we mean $d >> \xi_N$, while "narrow" means that the width w is small compared to the Josephson penetration depth, λ_J (Tinkham, 1975):

$$\lambda_J(T) = \left(\frac{\Phi_0 c}{8\pi^2} \frac{\delta}{j_c d_{eff}}\right)^{\frac{1}{2}} \tag{3.3},$$

where j_c is the critical current per unit width, δ is the thickness of the normal metal, and d_{eff} is the effective length of the junction. [For an SIS junction with a simple "sandwich" geometry (Tinkham, 1975, Fig. 6-6) $d_{eff} = d + 2\lambda_L$, where d is the distance between the superconducting electrodes, while for an SNS sandwich d_{eff} is probably less than d, due to the proximity effect in the N layer. The correct definition for our "bridge"-type SNS junctions is not obvious. For the sake of this discussion we simply assume $d_{eff} \approx d$]. As observed by Abraham et al. (1982), the critical current of an SNS array at low temperatures is well fit by the form (3.1), using the dirty limit form of $\xi_N(T)$, (3.2a).

Experimentally we defined the critical current $I_c(T)$ as the current at which the sample voltage exceeded some threshold, usually one picovolt when using the SQUID. Figure 3.1 shows results for sample DA1B-00 (with $\Delta^* \approx 0$), in zero field. Since the
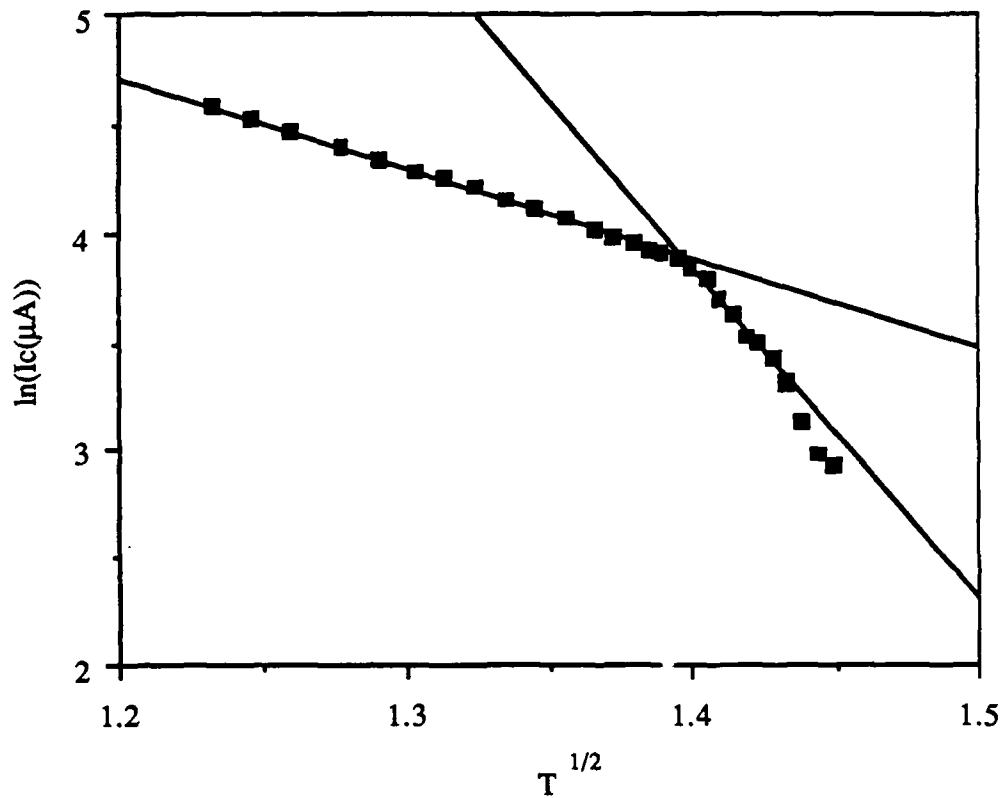
Figure 3.1 Natural logarithm of the measured critical current I_c (in μA), plotted vs. $\sqrt{T}$, for sample DA1B2-00. On such a plot the theortetical prediction of DeGennes, (3.1) is a straight line. The two linear regimes observed may be explained by non-uniform current flow in the sample, as discussed in the text.

measurements cover a small temperature range, far below $T_{cs} \approx 7$ K, the temperature dependence of I_c due to the prefactor in (3.1) is insignificant compared to the exponential. When plotted as $\ln[I_c(T)]$ vs. $T^{1/2}$ the data should then fall on a straight line. The data actually show two linear regimes, similar to data in other work (Clarke, 1969; Abraham, 1983). Following Clarke's work on single SNS junctions, Abraham suggested that, in his arrays, the crossover between the two linear regimes occured when λ_J became comparable to w, the width of the junction. According to (3.3), as temperature decreases, and $j_c(T)$ increases, λ_J decreases. When $2\lambda_J < w$, and assuming there are no vortices in the junction (which will almost always be true in an array at low temperature), the current does not flow uniformly but rather decays exponentially from each edge of the junction towards the center, with characteristic length λ_J. In this limit one has $i_c \propto j_c \cdot \lambda_J \propto \sqrt{j_c}$, so that, on a plot of $\ln(i_c)$ vs. $\sqrt{T}$, the slope should decrease by a factor of two as temperature decreases and the current becomes non-uniform in this so-called "self-field limited" regime. Abraham's data showed roughly a factor of two change in slope, occuring at a current level consistent, within a factor of five, with the approximate crossover condition, $2\lambda_J = w$. For our samples, using $\delta \approx 4000$ Å, $d_{eff} \approx d \approx 2$ μm, and $w \approx 4$ μm, this crossover should occur at $I_c \approx 2.6$ mA, compared to the observed $45 - 50$ μA.

We believe that the crossover in our samples may be due not to current nonuniformity in individual junctions, but rather in the sample as a whole. The appropriate penetration depth for the entire sample is $\lambda_\perp$, the perpendicular penetration depth. For a thin film this is given by λ_L^2/t (Pearl, 1964), where λ_L is the London penetration depth and t is the film thickness, while for an array it is given by (Lobb et al., 1983)

$$\lambda_\perp(T) = \frac{\Phi_o c}{8\pi^2 i_c^R(T)} \approx \frac{26 \text{ nA·cm}}{i_c^R(T)} \tag{3.4},$$

where $i_c^R(T)$ is the *fully renormalized* critical current. Although $\lambda_\perp$ can be several centimeters near T_c (Lobb *et al.*, 1983), as temperature decreases $\lambda_\perp$ can become less than the sample size, so that current will flow only within a distance of order $\lambda_\perp$ from each edge of the sample. Just as for the case of λ_J in a single junction we can set an approximate crossover criterion as $2\lambda_\perp = W$, where W is now the width of the entire sample, which for our 50 x 50 samples is approximately 0.065 cm. Using the *measured* critical current per junction, $i_c(T) = I_c(T)/50$, in place of the fully renormalized critical current in (3.5), we find that the condition $2\lambda_\perp = W$ is satisfied when $I_c(T) \approx 40~\mu A$. This is quite close to the observed crossover current of 49 μA.

This argument, however, fails to predict the temperature dependence of i_c at temperatures below the crossover, and in fact predicts that $I_c \propto i_c \cdot \lambda_\perp$ will be independent of temperature below the crossover, contrary to what is observed experimentally (Fig. 3.1). We presently have no other explanation for this crossover behavior.

Given the uncertainty in the nature of the crossover in $I_c(T)$ we have used a fit to the data closest to T_c to define $T' = TJ(T_c)/J(T) = TI_c(T_c)/I_c(T)$ in our analysis of the temperature dependence of the resistance. Using this data we can also compare our results to the theoretical value of $i_c^R(T_c)/T_c \approx 27$ nA/K (Lobb *et al.*, 1983). Defining T_c as the temperature at which the zero-field I-V exponent $a(T)$ equals three, we find $T_c = 2.385$ for the sample of Fig. 3.1, and $i_c(T_c)/T_c \approx 104$ nA/2.385 ≈ 44 nA/K. Assuming the approximate relationship $i_c(T_c) \approx (\varepsilon_c + \pi/8)~i_c^R(T_c)$ (Abraham, 1983), we find that the vortex dielectric constant $\varepsilon_c = \varepsilon(T_c)$ should have a value of 1.1 to obtain agreement with theory. This value is slightly lower than the results $\varepsilon_c = 1.3$ found by Kadin *et al.* (1983) in Hg-Xe films, and $\varepsilon_c = 1.5$ found by Leeman *et al.* (1986) in proximity arrays, but is not unreasonable.

It is worth noting that Abraham's (1983) analysis of critical current data *may* have been misguided in that all data appear to be in the regime where $\lambda_\perp$ is appreciably less than

the sample size. This would have lead to an underestimate of the rate of decrease of I_c with increasing temperature, leading to an overestimate of $i_c(T_c)/T_c$. The average value from several samples was $i_c(T_c)/T_c \approx 84 \pm 40$ nA/K, which requires $\varepsilon_c = 2.75 \pm 1.5$ to obtain agreement with theory. This value seems unreasonably large compared to others in the literature. Bunching of current near the sample edges may provide the explanation for this discrepancy.

3.3 Resistance versus temperature

Figure 3.2 shows $R(T)$ measured with a lock-in amplifier, with an rms sample current of $I=10$ μA. The sharp transition at $T \approx 6.9$ K is the superconducting transition of the Pb islands. The transition temperature is depressed from the bulk value 7.2 K by the proximity effect, which is particulary strong in this sample, which has 4000 Å of Cu and 2500 Å of Pb. The solid line is a fit to the proximity effect model of Abraham *et al.* (1982), which describes the spreading of superconductivity from the Pb into the Cu. The drop at $T = 2.0 - 3.5$ K is the KT transition, depressed somewhat by the high sample current.

Using the critical current data from the previous section to define the effective temperature T', we can fit the tail of the transition to the theoretical form (1.12), which we restate here using T' instead of T:

$$R(T) = c_1 R_o \exp\left[\frac{-2b}{\sqrt{\dfrac{T'}{T_c'} - 1}} \right] \tag{3.5}.$$

Figure 3.3 shows $V(T)$ taken with a SQUID, with $I = 0.5$ μA, and plotted as $\log(V)$
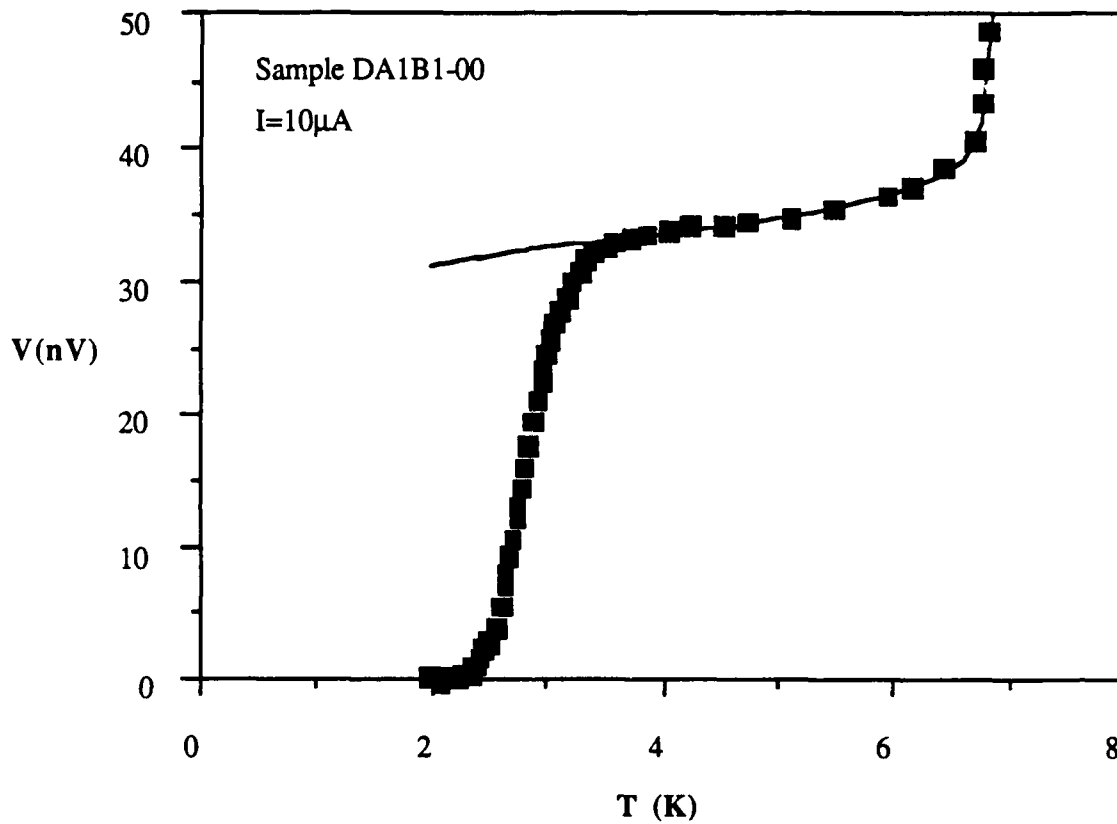
Figure 3.2   Sample voltage vs. temperature for a uniform sample, measured with a lock-in amplifier. The solid line is a fit to the proximity-effect model, which describes the initial drop in resistance due to the gradual spreading of superconductivity from the Pb into the Cu.
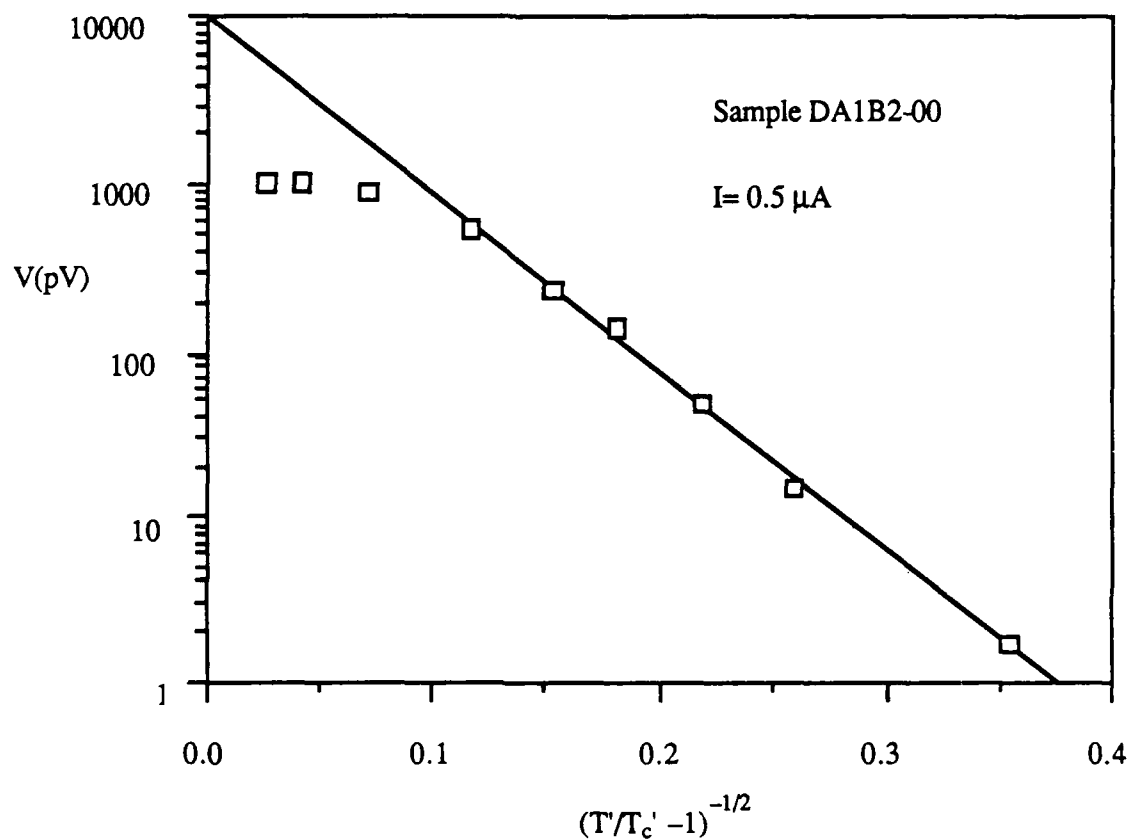
Figure 3.3 Voltage vs. temperature, measured with a SQUID, and plotted in such a way that the theoretical prediction of Halperin and Nelson, (1.12), is a straight line. The solid line is a fit to the data. The deviation at high temperature (to the left) occurs as the data enter the proximity-effect regime.

vs. $(T'/T_c' - 1)^{1/2}$, so that the theoretical prediction (3.6) is a straight line. The data agree with (3.6) over more than two decades, using fitting parameters $c_l = 5.0$ and $b = 12.3$. The deviation at high temperature (to the left) occurs as the data enter the proximity effect regime. Our value for c_l, which should be of order one, seems large but is not too unreasonable. To obtain greater dynamic range in such a measurement requires a larger sample, such as 1000×1000.

3.4 Resistance versus magnetic field

As discussed in section 1.3, the ground state energy and transition temperature of a Josephson junction array are complicated oscillatory functions of magnetic field strength, with a fundamental period corresponding to one flux quantum per unit cell of the array. In addition to the fundamental period there are higher-order oscillations with periods corresponding to rational values $f=p/q$, (p and q integers). This complicated structure has been demonstrated in both Monte Carlo simulations, where one usually computes the ground state energy, and in mean-field calculations, where one calculates $T_c(f_o)$ (Rammal *et al.*, 1982; Shih and Stroud, 1983).

Since the resistive transition is usually quite broad (sometimes several degrees) in a junction array (as distinct from wire arrays, which have sharp mean-field-like transitions), it is impossible to measure $T_c(f_o)$ directly. However, one can indirectly measure the modulation of T_c with field through the resistance vs. field, $R(f_o)$, or, given the difficulty in defining R at finite current levels, in sample voltage $V(f_o)$, or dynamic resistance, $dV(f_o)/dI \big|_{I=0}$. Ignoring the possiblility of a change in the nature of the phase transiton at particular values of f_o (section 1.3) one can simply view the modulation of T_c as a wholesale shift of the resistive transition. At a fixed temperature one then has (Tinkham *et*
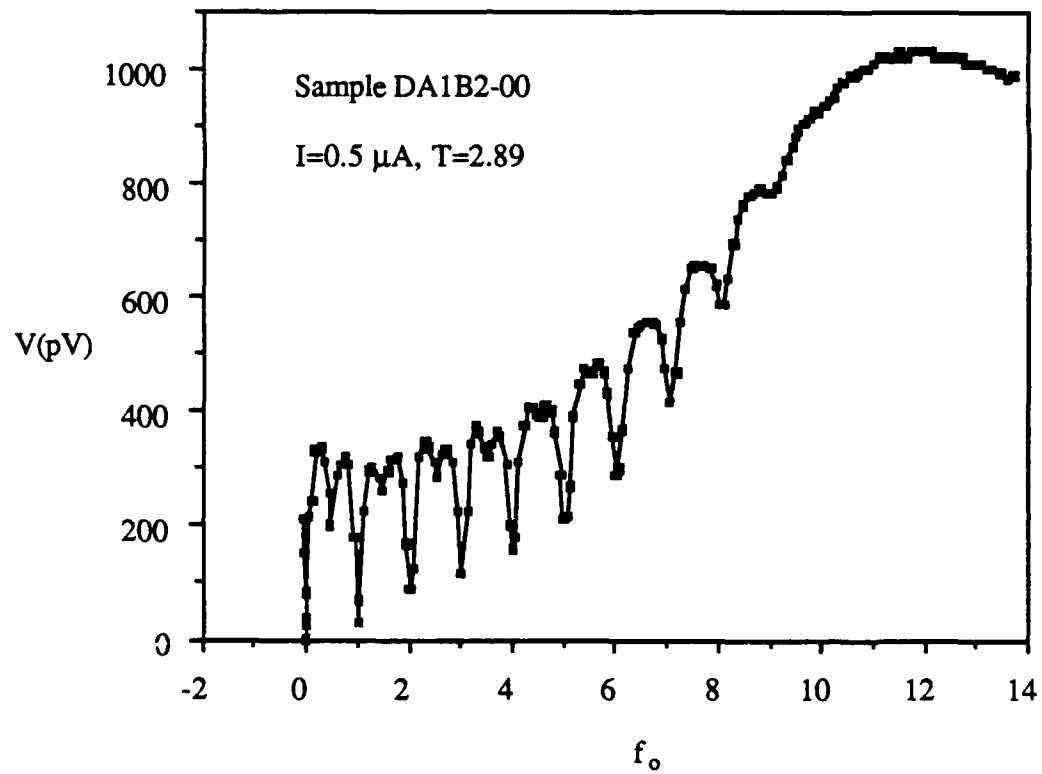
Figure 3.4 Sample voltage vs. magnetic field for a uniform array, showing principal oscillations and some structure at half-integer flux. The background is due to single-junction effects.

al., 1983)

$$V(f_o,T) - V(0,T) \equiv \Delta V(f_o,T) \approx (T_c(f_o) - T_c(0)) \cdot \left. \frac{dV}{dT} \right|_T$$

$$\equiv \Delta T_c(f_o) \cdot \left. \frac{dV}{dT} \right|_T \qquad (3.6).$$

Figure 3.4 shows $V(f_o)$, measured with a SQUID, for one of our uniform samples. One clearly sees the principal oscillations of period $\Delta f_o = 1$, as well as some fine structure at low fields. The data also demonstrate an effect alluded to in section 1.4, that is, the modulation of single junction critical currents by the magnetic field. For a finite area junction in a magnetic field the critical current is given by (Tinkham, 1975)

$$i_c(B) = i_c(B=0) \frac{\sin(\pi\Phi/\Phi_0)}{\pi\Phi/\Phi_0} \qquad (3.7),$$

where Φ is the flux in the junction area. This is the familiar Fraunhofer diffraction pattern, which has zeros at $\Phi=n\Phi_0$ ($n\neq0$). In real junctions one frequently has minima rather than zeros at these points, perhaps due to non-uniform current flow in the junction, which can result from asymmetries in the junction geometry, or self-field limiting (Miller and Finnemore, 1984). The resistance maximum at $fo \approx 12$ in Fig. 3.4 presumably corresponds to the first minimum in $i_c(B)$, where each junction contains one flux quantum. For this particular sample the area of the unit cell is roughly $(12 \ \mu m)^2$, while the area of a junction is approximately $2 \ \mu m \times 3.75 \ \mu m$, so that, assuming a uniform flux distribution, one would expect this first minimum to occur at $fo \approx 144/(2 \times 3.75) \approx 19$. However, due to the screening of the magnetic field by the superconducting islands, the flux is not uniform on the scale of a single juntion but rather is "squeezed" into the areas between the islands, including the junction areas, so that the junctions contain more flux than naively expected.
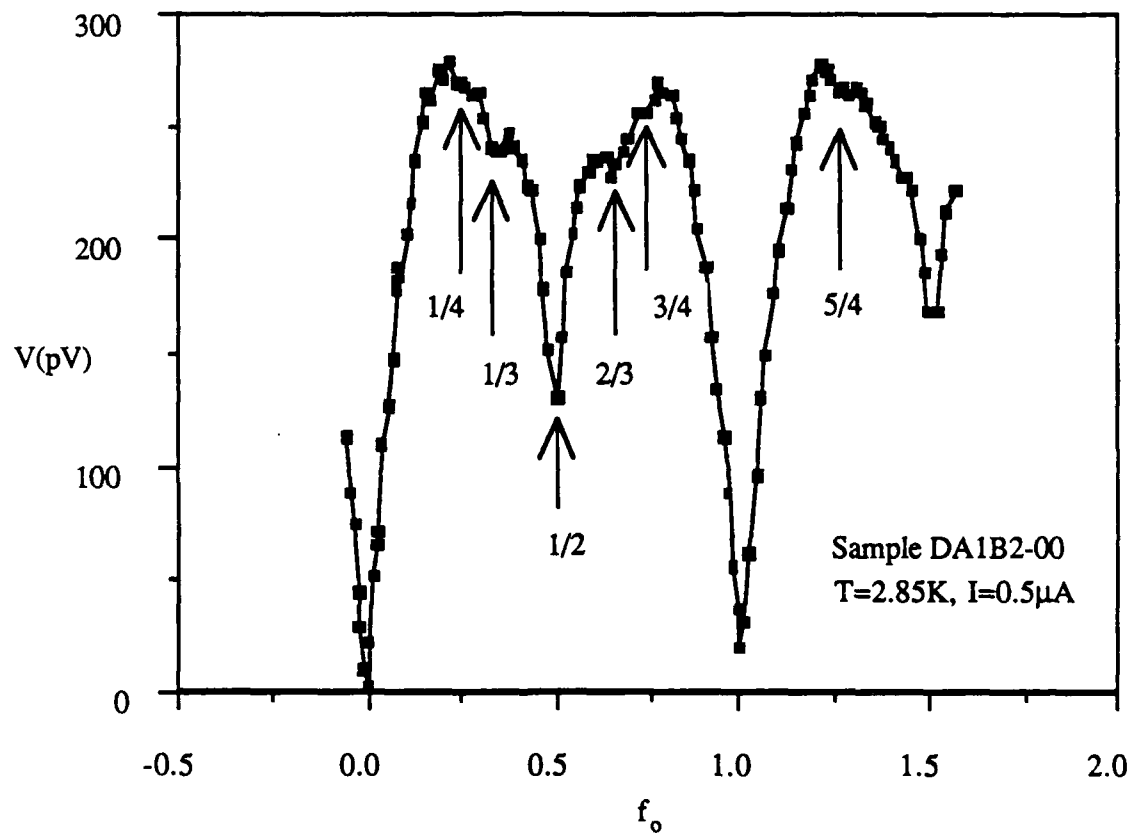
Figure 3.5 Detail of sample voltage vs. magnetic field for a uniform array, showing higher-order structure.

Figure 3.5 shows a more detailed measurement of $V(f_o)$ over approximately one flux quantum. The data show a strong minimum at $f_o =1/2$, as well as secondary minima at f_o = 1/3 and 2/3, and recognizable features at f_o = 1/4, 3/4, and 5/4. The principal oscillations require phase coherence over a distance of order the latttice parameter s, while structure at rational values $f_o =p/q$ requires phase coherence over a distance of order $q \cdot a$. This can be understood theoretically from the structure of the ground states for $f_o =p/q$, which consist of $q \times q$ primitive cells (Teitel and Jayaprakash, 1983b). For the array resistance to show structure at $f_o =p/q$ these $q \times q$ cells must intefere coherently. Experimentally, Van Harlingen and Springer (1987) have fabricated arrays with $n \times m$ plaquettes, with $n \sim 1000$ and $m = 1,2,3...$, and have demonstrated that $R(f_o)$ only shows structure for $q \leq m$. That is, an $n \times 1$ plaquette array only shows principal oscillations while an $n \times 2$ shows structure at integer and half-integer flux, and so on.

The rich structure in $V(f_o)$ provides information about relatively short-range coherence, over distances of a few lattice parameters, in an array above T_c. Since we are interested in the destruction of phase coherence in arrays with positional disorder we have taken such data for samples with various amounts of disorder. Figure 3.6 shows $V(f_o)$ for samples with various values of Δ^*, for both positive and negative fields. Most of these data (except for the $\Delta^* \approx 0$ trace) were taken at relatively high temperatures, where the sample resistance is of order half the "normal resistance" (the resistance below the Pb transition), R_o. At such a temperature dV/dT is typically at its maximum value, so that, from (3.4), the principal oscillations are large; however the temperature is too high to observe higher-order structure, which relies on more delicate coherence. One observes a trend that the amplitude of the resistance oscillations decreases with increasing field, samples with larger Δ^* showing a more rapid decrease. For example, for $\Delta^* \approx 0$ oscillations appear to persist out to $f_o \approx \pm 9$, while for $\Delta^* = 0.20$ only to $f_o \approx \pm 3 - 4$.

Figure 3.7 shows $R(f_o)$ to larger fields, for samples with $\Delta^* =0.10$ and ≈ 0, and
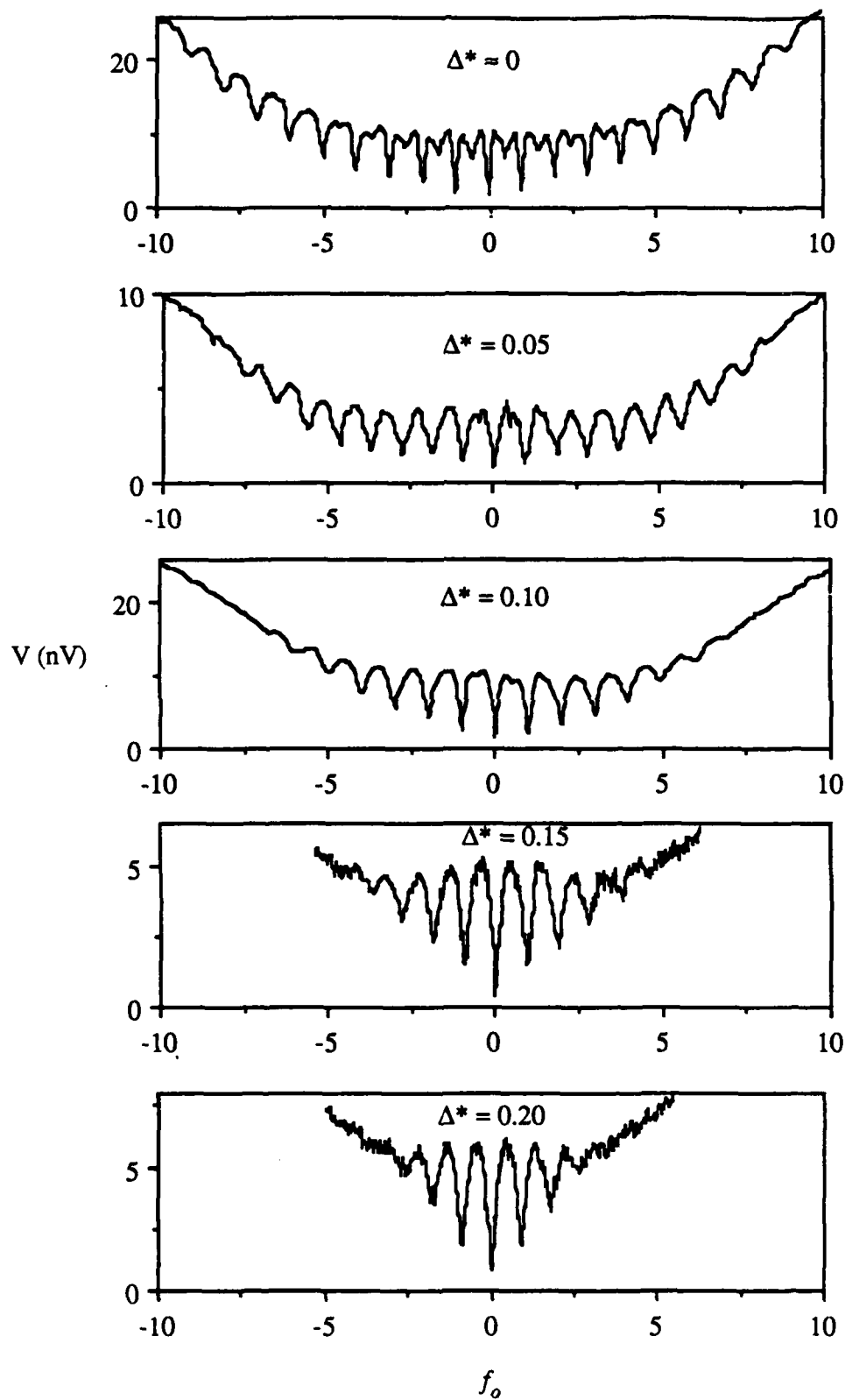
Figure 3.6   Voltage (at I=10μA) vs. magnetic field for samples with various values of Δ^*.
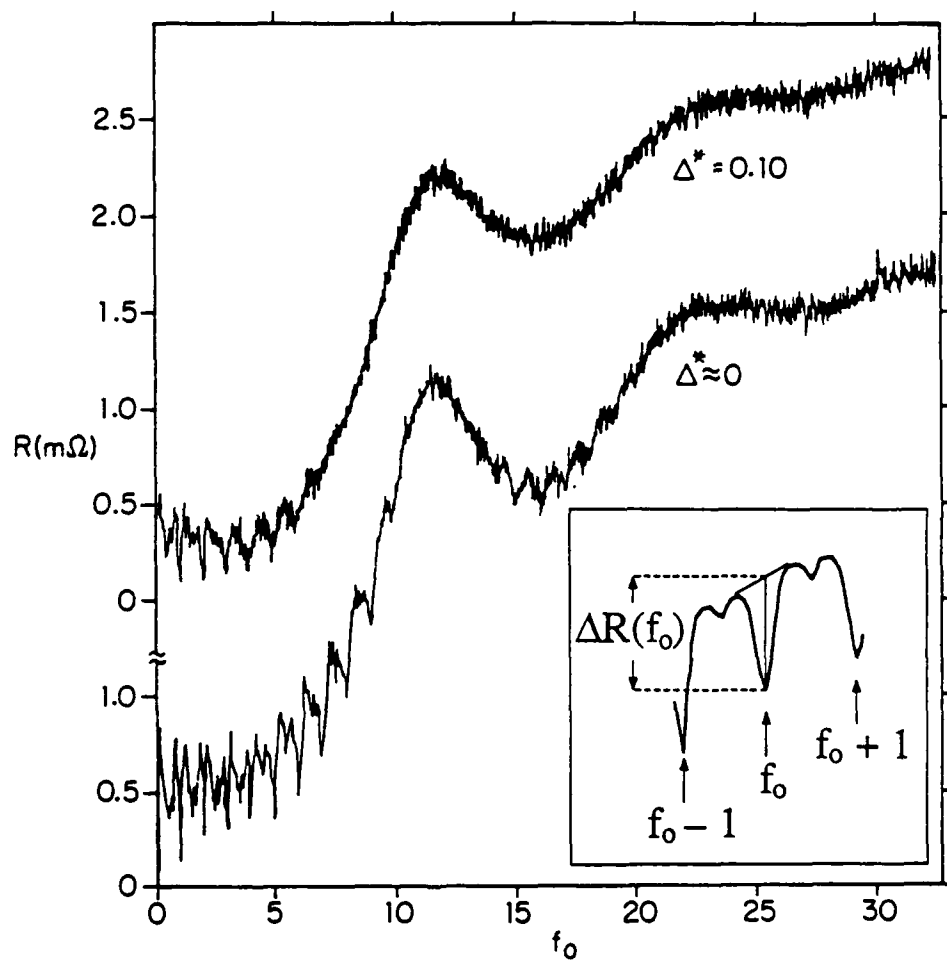
Figure 3.7 Resistance vs. magnetic field, $R(f_o)$, for $\Delta^* = 0.10$ (upper trace) and $\Delta^* \approx 0$ (lower trace), showing oscillations due to collective behavior, modulated by single-junction effects. Inset shows definition of oscillation amplitude $\Delta R(f_o)$.
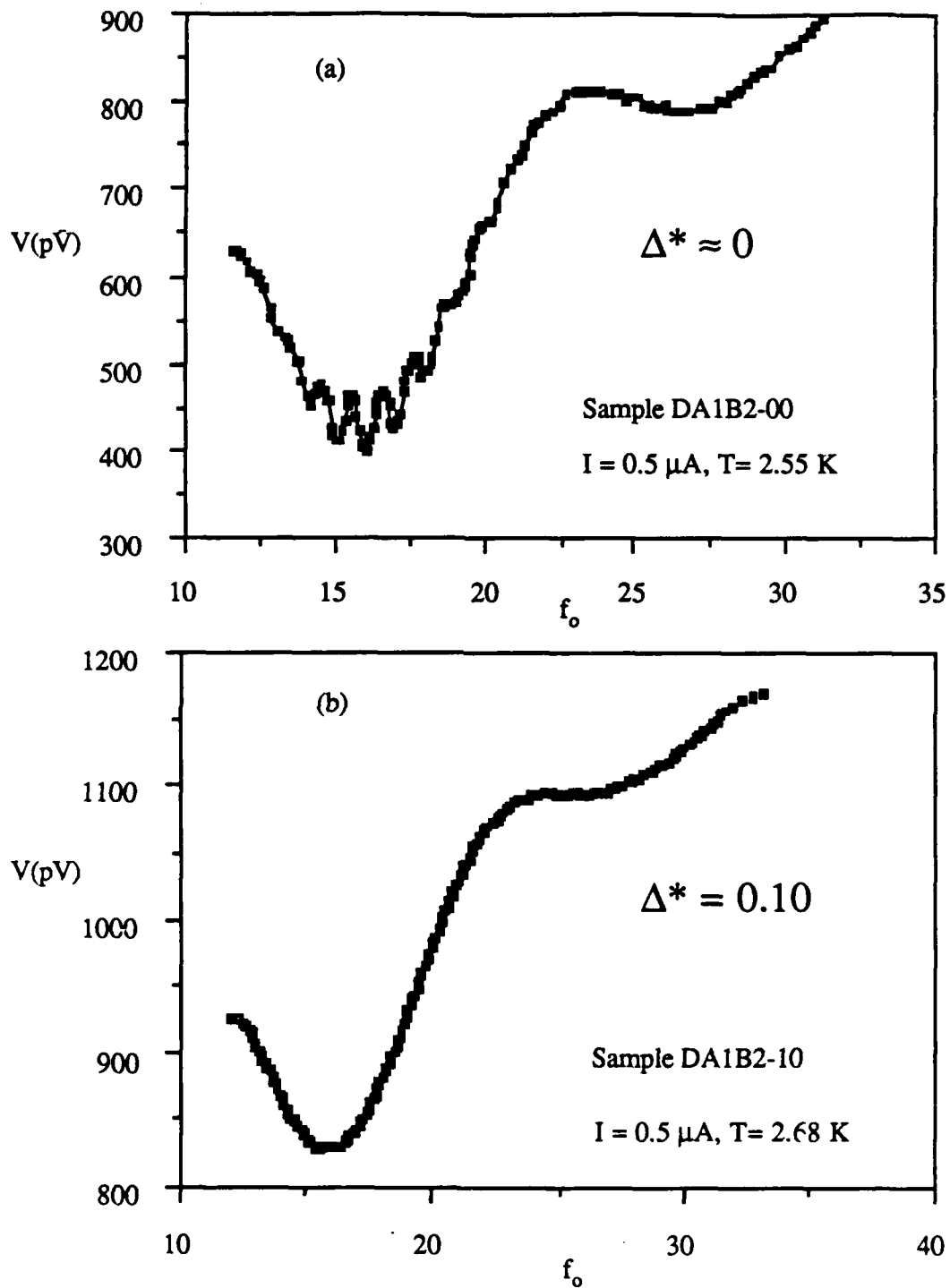
Figure 3.8 Voltage vs. magnetic field at high fields for samples with (a) $\Delta^* \approx 0$, and (b) $\Delta^* = 0.10$. The uniform sample shows oscillations near the secondary minimum of the single-junction diffraction pattern, whereas the disordered one does not.

shows more clearly the Fraunhofer diffraction pattern discussed earlier, with the secondary minimum in R (maximum in i_c) clearly visible. From the lower trace one sees that , in the uniform sample, although the resistance oscillations are decaying as the resistance approaches the first maximum at $f_o \approx 12$, they are visible again as the resistance drops into the second minimum. Fig. 3.8a shows data taken in this region in another sample with Δ^* ≈ 0, using the SQUID for improved signal-to-noise ratio, and shows more cleanly the persistence of the resistance oscillations in this secondary minimum. In contrast, the sample with $\Delta^* = 0.10$ (upper trace in Fig. 3.7) shows no oscillations in this region, even in data taken with the SQUID, as shown in Fig. 3.8b.

3.5   Critical fields

To quantify the destruction of phase coherence we wish to quantify the decay of resistance oscillations in samples with various amounts of disorder. In order to do this we must first account for the single junction effects which modulate the resistance oscillations (Figs. 3.6 and 3.7). In principle one could consider fitting the background to a function which incorporates the modulation of the junction critical currents as described by (3.5). However, as noted earlier, (3.5) apparently fails to describe our arrays in that the array resistance does not reach its normal value, R_o, at the first maximum, where the junction critical currents should, according to (3.5), all be zero. This is presumably due to our samples having a distribution of effective junction areas, and, to a lesser extent, to non-uniform current flow in individual junctions.

As a simple alternative we point out that , empirically, the amplitude of the resistance oscillations always goes to zero at the first maximum in the background, R_{max}, which
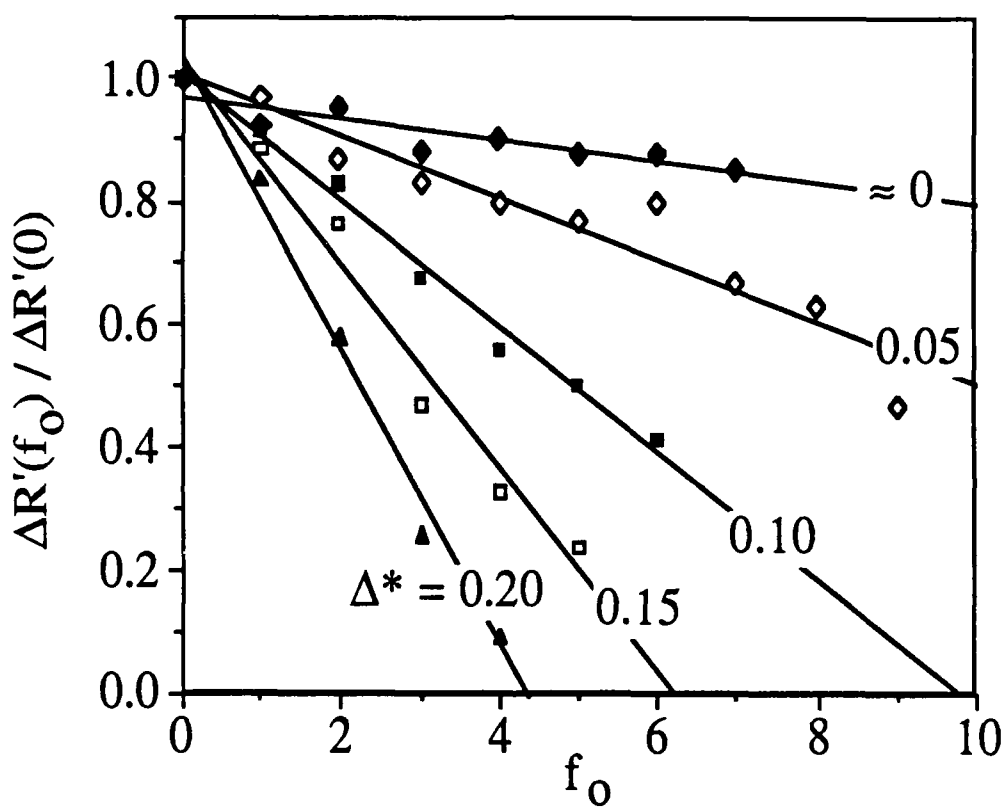
Figure 3.9 Amplitude of resistance oscillations vs. f_o, for various values of Δ^*. The lines are least-squares fits, whose extrapolations to zero define experimental critical fields f_c.

occurs at $f_o \approx 12$ for the sample of Fig. 3.7. This suggests the following approximate procedure to compensate for single junction effects. We determine the oscillation amplitude as a function of f_o, $\Delta R(f_o)$, as illustrated in the inset in Fig. 3.7, and introduce a rescaled oscillation amplitude, $\Delta R'(f_o) \equiv \Delta R(f_o)/(R_{max} - R(f_o))$. (Alternatively, one could replace R_{max} with a field-dependent offset defined by a tangent line to all the observed local maxima in the background. This would not significantly change our results).

Figure 3.9 shows $\Delta R'(f_o)$, normalized to its value at $fo = 0$, for samples with varying amounts of disorder. One sees that, empirically, $\Delta R'$ decreases linearly with increasing f_o, samples with greater disorder showing a steeper decrease. The lines in Fig. 3.9 are least-squares fits assuming linear behavior. For each sample, the point at which this fit intercepts the line $\Delta R' = 0$ is an estimate of the field at which the oscillation amplitude goes to zero. As discussed earlier, at this field we expect that phase coherence has been destroyed on a length scale of order the lattice parameter.

We thus define an experimental critical field, f_c^{exp}, as the field at which, for a given value of Δ^*, the linear fit to $\Delta R'(f_o)$ intercepts $\Delta R' = 0$. Figure 3.10 shows f_c^{exp} plotted vs. $1/\Delta^*$, and demonstrates the linear dependence predicted by (1.29), but with $f_c^{exp} \approx 0.95/\Delta^* \approx 0.55/\Delta$, compared to the theoretical critical field, $0.10/\Delta$. Of course the theoretical critical field corresponds to the destruction of *long-range* (or "quasi-long-range") order, whereas the experimental critical field thus defined corresponds to the destruction of the more robust short-range coherence. Therefore f_c^{exp} *should* be larger than the theoretical critical field.

As for the linear decay of resistance oscillations (and therefore of T_c oscillations) with field, there is no theory available for comparison since the only tractable magnetic fields are *integer* values of f_o, and, to a lesser extent, $f_o = n \pm 1/2$. The oscillation amplitudes are determined by the resistance at integer fields and at the adjacent maxima, where f_o is typically approximately $n \pm 0.4$, for which no theory is available. However, Benz (1987)
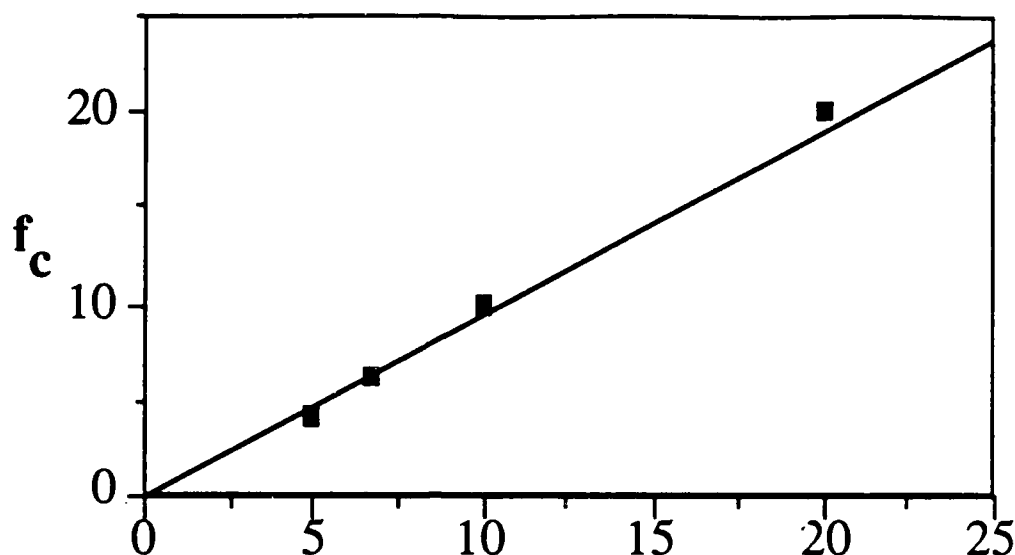
Figure 3.10 Values of f_c from Fig. 3.9, plotted vs. $1/\Delta^*$. The line is a least-squares fit constrained to have zero intercept.

has numerically solved the linearized Ginzburg-Landau equations for an 8×8 array of superconducting wires, to find the mean-field transition temperature, $T_c(f_o)$, *in the presence of positional disorder*. Considering only fields $f_o = n/8$ commensurate with the 8×8 cell, and imposing periodic boundary conditions on the superconducting order parameter, he found that the oscillation amplitudes, $\Delta T_c(f_o)$, decay *approximately* linearly with f_o, as shown in Fig. 3.11, in agreement with our experiments. However, these calculations do show some evidence for non-linearity at low fields, which does not appear in our data.

Although theory deals rather easily with long-range phase coherence, it is difficult, if not impossible, to find an experimental probe of such coherence, especially in a small sample, where finite-current and finite-size effects are important. However, we do have at our disposal an experimental signature of phase coherence on length scales somewhat
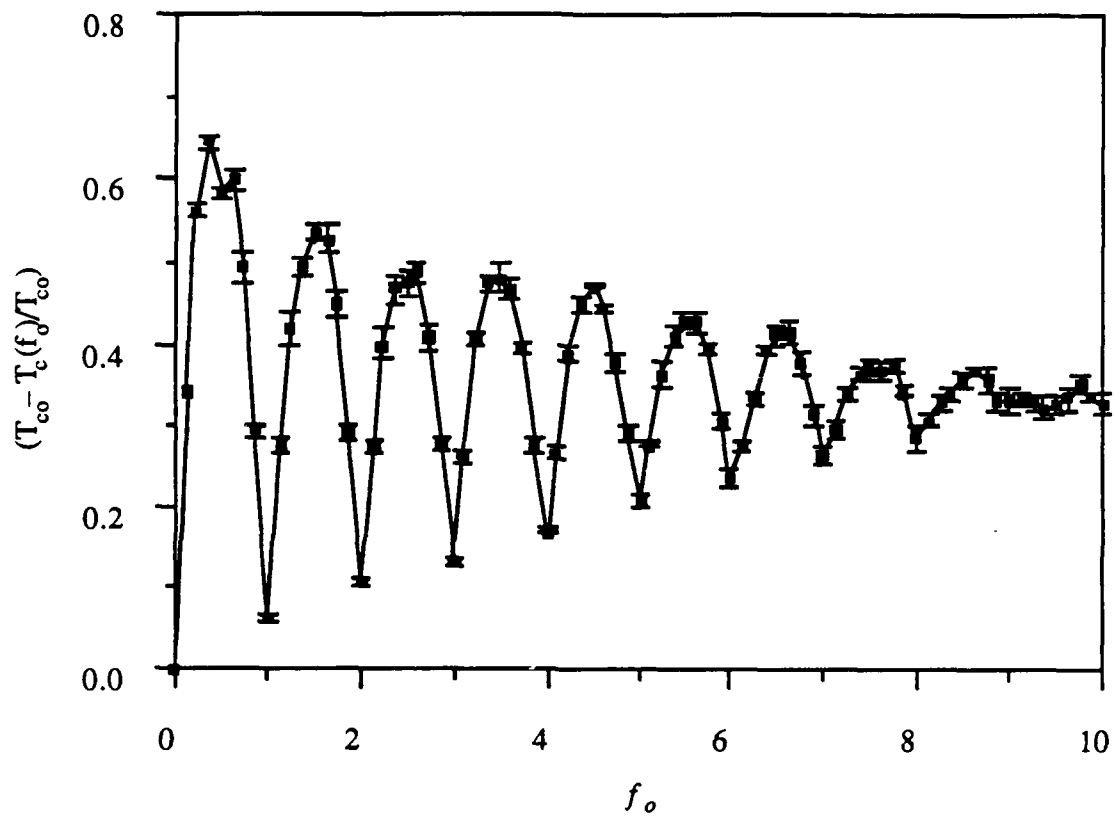
Figure 3.11 Transition temperature vs. field for a wire network with positional disorder, computed using the linearized Ginzburg-Landau equations (Benz, 1987).

larger than the lattice parameter – the higher-order structure in $R(f_o)$.

We recall that a local resistance minimum at a field $f_o = p/q$ is due to phase coherence over a length of order $q \cdot s$. If we can quantify the destruction of such higher-order features with field, and define critical fields $f_c(\Delta^*, q)$ by the disappearance of features at $f_o = p/q$, then we can quantify the destruction of phase coherence over these longer lengths. Of course, the case $q = 1$ corresponds to the principal oscillations already discussed.

In practice we have only attempted to quantify our data for $q = 1$, 2, and 3, since data clean enough to show higher-order effects were the exception rather than the rule. Even for $q = 3$ we only have data for one sample, with $\Delta^* = 0.10$. A further complication is the role of single junction effects, finite measuring currents, and sample imperfections, in suppressing these higher-order structures. From Fig. 3.4 one can see that even in a nominally uniform sample the half-integer ($q = 2$) structure is destroyed at relatively low fields. Unfortunately, the resistive transitions of the various samples are sufficiently different that we cannot simply normalize results for $\Delta^* \neq 0$ to those for $\Delta^* = 0$. We simply note that such structure will be systematically suppressed by a combination of finite-current effects and uncontrolled sample inhomogeneity.

Since it is difficult to define an oscillation amplitude analogous to $\Delta R(f_o)$ for these higher-order features, we have, rather subjectively, defined critical fields $f_c(q=2)$ and $f_c(q=3)$ by noting where the last feature at irreducible rational values $f_o = p/2$ and $p/3$ occurs. If, in the data with the best signal-to-noise ratio, a feature is observed at $f_o = n + 1/2$, but not at $f_o = n + 3/2$, we define $f_c(q=2) = n + 1$, with an error $\pm 1/2$. Similarly, if a minimum is observed at $f_o = n + 1/3$ ($f_o = n + 2/3$) but not at $f_o = n + 2/3$ ($f_o = n + 4/3$), we define $f_c(q=3) = n + 1/2$ ($f_c(q=3) = n + 1$), again with a subjective error of $\pm 1/2$.

The data for $f_c(q)$ are presented in Fig. 3.12. Empirically we find that $f_c(q) \cdot \Delta^*$ is a linear function of $1/q^2$,
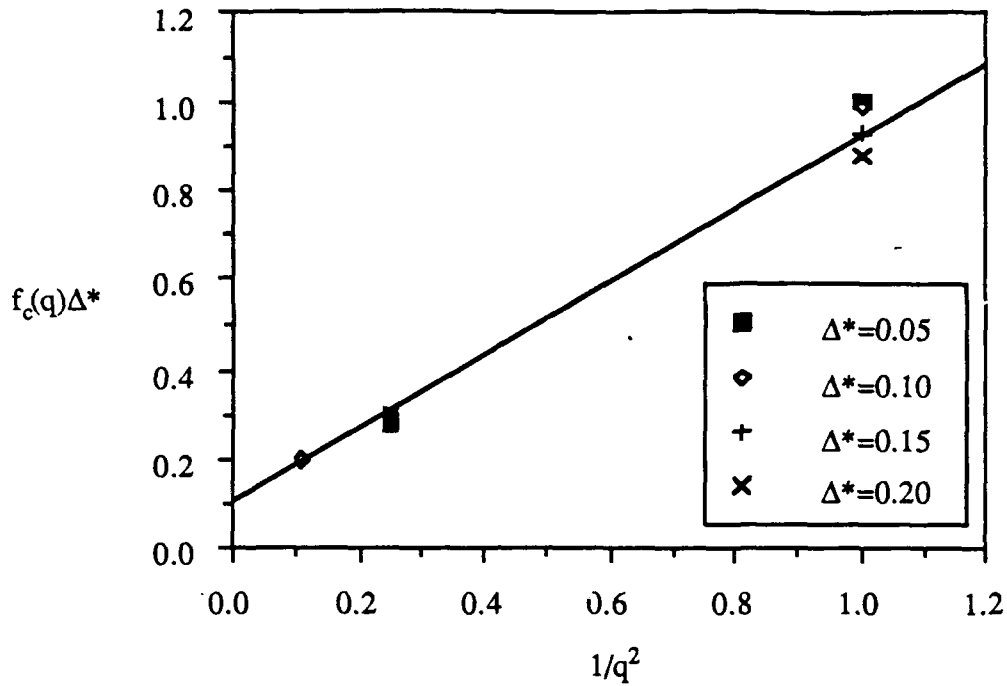
Figure 3.12 Critical fields for structures at fields $f_o = p/q$, corresponding to the destruction of phase coherence on length scales of order $q \cdot s$. Extrapolating to $q = \infty$ gives an estimate for the critical field for destruction of long-range coherence.

$$f_c(q) \cdot \Delta^* \ = \ c_1 + \frac{c_2}{q^2} \qquad (3.8),$$

and the line in Fig. 3.12 is a least squares fit assuming this form. The origin of this q-dependence is not known, but given our identification of $q \cdot s$ as a coherence distance one is reminded of the perpendicular critical field of a superconducting film, $H_{c\perp} \propto 1/\xi^2$, where ξ is the Ginzburg-Landau coherence length. The constant offset c_1 is of course a new feature. If we assume that the form (3.8) holds for all q then we can extrapolate to $q = \infty$ to estimate a critical field, $f_c(q = \infty) = c_1$, for the destruction of QLRC. The data of Fig. 3.12 give a value $f_c(q = \infty) \Delta^* = 0.105 \pm 0.010$. Using our approximation $\Delta \approx \Delta^*/\sqrt{3}$ gives $f_c(q = \infty) \cdot \Delta \approx 0.061 \pm 0.006$, compared to the theoretical result (1.29), $f_c \cdot \Delta = 0.10$.

Given the uncertainties in our analysis, the agreement between our experimental $f_c(q=\infty)$ and the theoretical result is quite satisfactory.

The *sign* of the discrepancy between $f_c(q=\infty)$ and (1.29) can be accounted for by the suppression of higher-order structure due to the combination of effects discussed above, for which we have no quantitative description. We should also reemphasize that our conversion $\Delta \Leftrightarrow \Delta^*/\sqrt{3}$ is only approximate, since it ignores higher moments of the probability distributions for site displacements.

3.6 Summary

We have presented our experimental results on 50×50 arrays of Pb-Cu proximity-effect or SNS junctions, with and without positional disorder. This disorder was introduced by randomly displacing the center of each cross-shaped superconducting island, while preserving the distance of closest approach, so as to avoid disorder in the critical currents of the junctions. The disorder is characterized by a parameter Δ^*, which is the half-width of our uniform distribution of site displacements.

In zero field these arrays have properties similar to those measured by other workers. The critical current of the array as a whole is well fitted, at low temperatures, by the DeGennes (1964) expression for the critical current of a single SNS junction. At the lowest temperatures we observed a crossover to a regime in which the measured critical current increased less steeply with decreasing temperature. In previous work on arrays (Abraham, 1983) a similar crossover was found to be consistent with the Josephson penetration depth, λ_J, becoming smaller than the width of a single junction, so that current flowed ony within a distance of order λ_J from each edge of the junction. In our

measurements this crossover occurs at a lower current level, probably below the sensitivity of Abraham's meaurements. The current at which the crossover occurs appears to be consistent with the perpendicular penetration depth, $\lambda_\perp$, becoming smaller than the width of the entire sample, so that the current flows within a distance of order $\lambda_\perp$ from each edge of the sample as a whole. However this explanation does not predict the correct temperature dependence for I_c below the crossover. Although this issue is not fully resolved, it does seem likely that Abraham's critical current measurements were made in a regime where the current was flowing non-uniformly in the whole array. This would explain the high estimates of $i_c^R(T_c)/T_c$ obtained in that work. Our results for $i_c^R(T_c)/T_c$ are in much better agreement with theory.

The zero-field resistive transition of our samples can be understood in terms of the two behaviors seen in other work. The initial gradual decrease in resistance, below the Pb transition, is well fit by the proximity-effect model of Abraham *et al.* (1982), which describes the gradual spreading of superconductivity from the Pb into the Cu. SQUID measurements of the transition to zero resistance, on the other hand, are in excellent agreement with the theory of Halperin and Nelson (1979) for the KT transition, as long as one uses the effective temperature $T' = TJ(T_c)/J(T)$ appropriate for an array (Lobb *et al.*, 1983).

Our arrays show rich structure in their resistance vs. perpendicular magnetic field, $R(f_o)$, with principal oscillations of period $\Delta f_o = 1$, and reproducible structure at $f_o - n = 1/2, 1/3, 2/3, 1/4,$ and $3/4$. We also observe a modulation of the principal oscillations by single-junction effects, which are due to the field modulating the critical currents of the individual junctions.

After correcting for these single-junction effects we find that the amplitude of the principal oscillations, $\Delta R'(f_o)$, decays approximately linearly with f_o in our disordered arrays, samples with greater disorder showing a steeper slope. By extrapolation of a linear

fit to such data we define an experimental critical field, $f_c^{exp} \equiv f_c(q=1)$, as the field where $\Delta R'$ goes to zero, so that the principal oscillations are completely suppressed. Plotting $f_c(q=1)$ vs. $1/\Delta^*$ we find the empirical form , $f_c(q=1) \approx 0.95/\Delta^* \approx 0.55/\Delta$, so that $f_c(q=1)$ has the same dependence on disorder as does the theoretical critical field, $f_c = 0.10/\Delta$. We argue that $f_c(q=1)$ is the field at which phase coherence is destroyed on a length scale of order the lattice parameter, s.

By quantifying the destruction of higher-order features in $R(f_o)$, at rational values $f_o - n = p/q$, we were able to quantify the destruction of phase coherence on slightly longer length scales. We defined critical fields $f_c(q)$ by the disappearance of such features , and considered data for $q = 1$, 2 and 3. We found that, empirically, $f_c(q)$ followed the form $f_c(q) \cdot \Delta^* = c_1 + c_2/q^2$ quite closely. Extrapolating to $q = \infty$, for long-range coherence, we obtained a result $f_c(q) \approx (0.061 \pm 0.006)/\Delta$, in quite good agreement with the theoretical result $f_c = 0.10/\Delta$.

3.7 Sierpinski gasket arrays of proximity effect junctions

Regular two-dimensional Josephson junction arrays exhibit broad, fluctuation-dominated behavior, undergoing a Kosterlitz-Thouless transition in the absence of frustration, while wire networks, due to much stronger couplings between superconducting islands, exhibit sharp, Ginzburg-Landau-type transitions. Similarly, quasiperiodic junction arrays (Springer and Van Harlingen, 1987) exhibit characteristics which are qualitatively different from those of quasiperiodic wire networks (Behrooz *et al.*,

1986). Sierpinski gasket wire networks, which have a fractal dimension of 1.585, show a narrow Ginzburg-Landau-type phase transition, with the transition temperature as a function of magnetic field, $T_c(B)$, exhibiting dilation invariance, reflecting the self-similar geometry of the gasket (Gordon *et al.*, 1986).

Using the same techniques as for our disordered arrays we have fabricated sixth order Sierpinski gasket arrays of proximity-effect junctions (Lee *et al.*, 1987). These arrays are not expected to undergo a Kosterlitz-Thouless transition, because they are less than two-dimensional. However, the samples show broad transitions, characteristic of weakly-coupled, fluctuation-dominated systems, in contrast to the Ginzburg-Landau behavior seen in wire arrays. Measurements of the zero-field resistive transition and the current-voltage (I-V) characteristics appear to suggest the existence of collective behavior of the junctions in this system.

Our sixth-order gaskets consist of 1095 Pb islands coupled by the proximity effect. Sections of an e-beam written mask are shown in Fig. 2.6. The smallest repetition length is 12.7 μm and the inter-island spacing is 2.2 μm.

We have measured resistance and I-V characteristics as a function of both temperature and applied perpendicular magnetic field. Sample current was injected at one vertex and extracted symmetrically from the other vertices, and the longitudinal potential difference was measured as shown in the inset of Fig. 3.13a. Figures 3.13a and b show the zero-field resistive transition for samples G2 and G1, respectively, the former taken with sample current $I = 20$ nA, using a SQUID, the latter with $I = 10$ μA, using a lock-in amplifier. As expected, the resistive transitions for both samples are broad and fluctuation-dominated.

As in regular 2D arrays, the temperature dependence of the resistance near the superconducting transition of the PbBi islands fits well to the proximity-effect model (the solid curve in Fig. 3.13b). At temperatures below the proximity-effect regime the
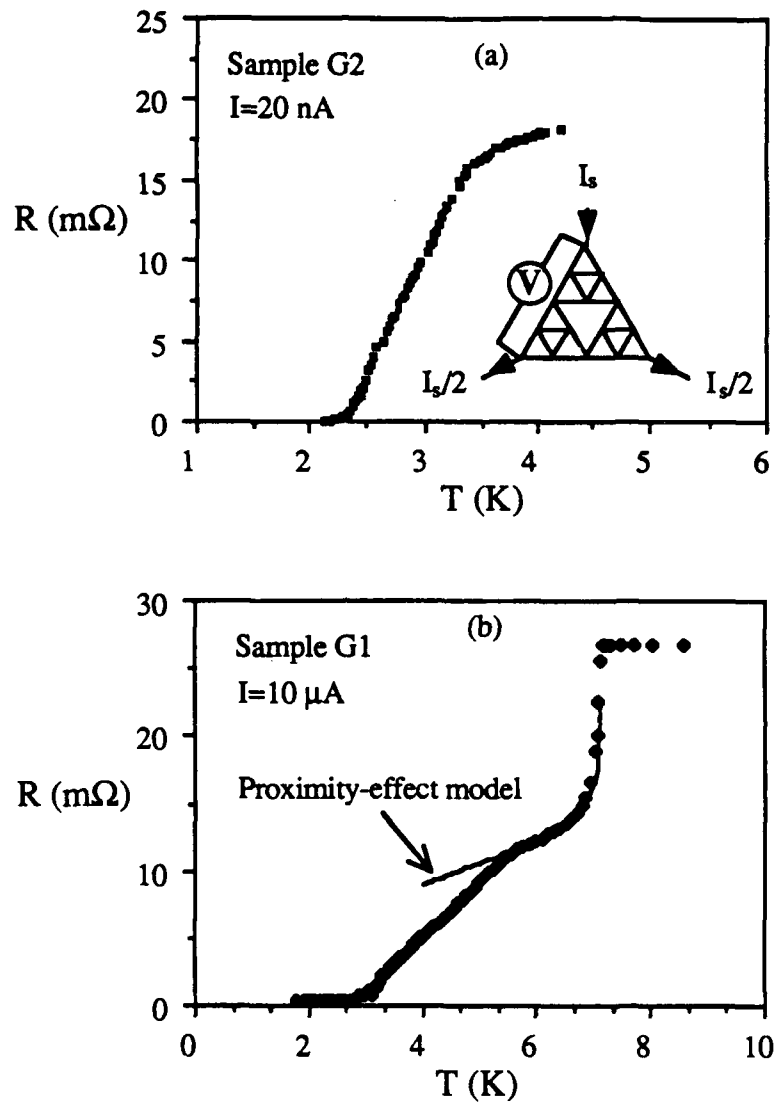
Figure 3.13 Zero-field resistive transitions of (a) Sierpinski gasket sample G2, measured with a SQUID, and (b) sample G1, measured with a lock-in amplifier.

resistance is linear in temperature over a wide temperature range. This broad linear region apparently has no analog in regular arrays, and it is unclear what theoretical model might be appropriate. The data in this regime do not fit the theory of fluctuation effects such as Aslamasov-Larkin fluctuation-enhanced conductivity (Aslamasov and Larkin, 1968), $\Delta\sigma \propto [T/(T-T_{co})]^{(4-d)/2}$, for dimension $d=1$, $d=2$, or $d=1.585$, the fractal dimension of the gasket, where T_{co} is the fitted mean-field transition temperature.

Near the zero-resistance transition, the resistance is found to be highly nonlinear with temperature. The temperature dependence of the resistance in this regime appears not to fit the 2D Kosterlitz-Thouless Halperin-Nelson form (1.12), even using the effective temperature $T'=T\,I_c(T_c)/I_c(T)$, where T_c is the zero-resistance transition temperature. The data also do not fit the single-junction Ambegaokar-Halperin form (Ambegaokar and Halperin, 1969), which might be expected if the junctions at the constricted areas of the gasket, which carry the highest current, dominate the resistance. This temperature dependence would also be expected for series arrays at temperature not too close to T_c, where long-range fluctuations develop. Our tentative conclusion is that the resistive transition of this fractal system cannot be described by 1D or 2D theories.

Figure 3.14 shows the zero-field (< 1 mG) I-V characteristics for sample G2 in a broad temperature range near the zero-resistance transition. For high currents, the I-V characteristics become linear because the sample is driven normal. In the intermediate current range, however, the I-V characteristics show power-law behavior, similar in some ways to the case of regular 2D array in the current-dominated regime, where the current-unbound vortices dominate the resistance. For low currents, the I-V characteristics again show power-law behavior, $V \propto I^{a(T)}$, but with lower powers than in the intermediate current range. In this range, $a(T)$ increases smoothly with decreasing temperature, showing no clear evidence of jump from three to one in the present data. In a large array, the absence of a jump in $a(T)$ would rule out the existence of a Kosterlitz-Thouless
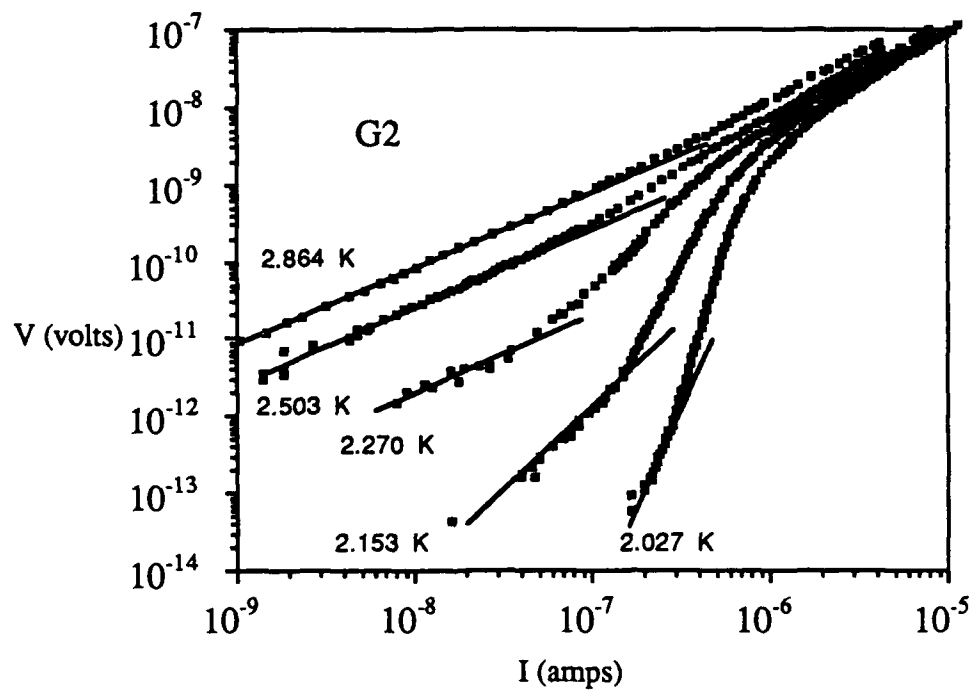
Figure 3.14 Current-voltage characteristics for sample G2. The lines are guides to the eye for the data in the low-current power-law regime.
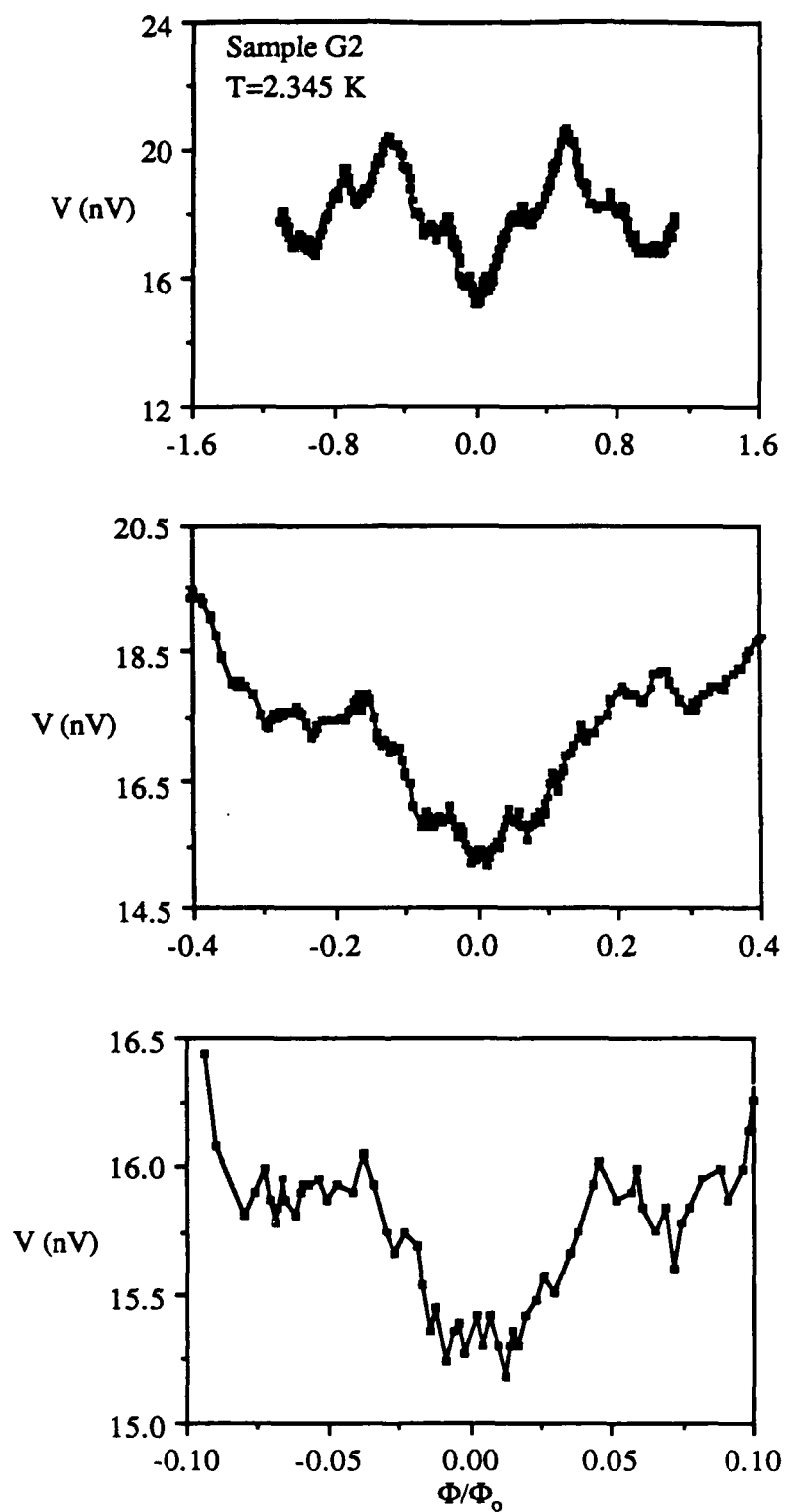
Figure 3.15 Voltage vs. magnetic field for Sierpinski gasket sample G2, showing dilation invariance as the field axis is expanded by factors of four.

transition. However, in our samples the lack of a jump might be due to finite-size effects.

As observed earlier in the arrays of wire networks (Gordon *et al.*, 1986), the sample voltage as a function of external field, $V(H)$, reveals dilation invariance, showing similar structure as we expand the field axis by a factor of 4 (see Fig. 3.15). We could resolve structure in $V(H)$ corresponding to a flux quantum in the area of a 3rd order gasket, implying that $V(H)$ reflects the large-scale fractal nature of the gaskets.

In conclusion, although the Sierpinski gasket array of junctions shows a fluctuation-broadened transition, as do regular 2D arrays, the transition does not fit the Aslamasov-Larkin, Ambegaokar-Halperin, or Kosterlitz-Thouless-Halperin-Nelson behavior. Current-voltage characteristics of this system are in some ways similar to those of 2D arrays, but the apparent smooth temperature variation of $a(T)$ makes the system distinct from the 2D arrays.

CHAPTER FOUR

NUMERICAL SIMULATIONS

4.1 Introduction

To gain further insight into the problem of Josephson junction arrays with positional disorder, we have performed Monte Carlo simulations of an XY spin system with non-uniform frustration. As discussed in chapter one, such a model provides a somewhat idealized Hamiltonian, from which the theoretical predictions of chapter one were derived, and which can serve as an input to an approximate numerical calculation of thermodynamic quantities such as the energy, specific heat, and helicity modulus. Our goal is to calculate such quantities for systems whose size is comparable to our experimental samples, in contrast to the theoretical description of "fully renormalized" quantities, which is only appropriate in the infinite-sample limit.

We begin with a review of the basic ideas behind the Monte Carlo method of Metropolis *et al.* (1953), and then discuss the specific way in which we have applied this method to the study of the randomly frustrated XY model. Next we present our results, with emphasis on two particular quantities – the magnetization modulus, and the helicity modulus. The magnetization modulus gives information about phase ordering while the helicity modulus, the analog of the shear modulus in a solid, is related to the effective superfluid density in an array, and is therefore a natural place to look for reentrant superconductivity.

4.2 The Metropolis rule

A complete review of Monte Carlo techniques and their application to problems in statistical physics is beyond the scope of this work. Our goal in this section is simply to review the ideas behind the Metropolis rule, and then, in the next section, to describe how we have implemented this rule for our study of disordered XY models. Our discussion follows closely the first part of the excellent review article by Binder (1974, chapter I).

Consider a system of N particles, whose interactions are described by a known Hamiltonian, H_N. For simplicity we assume that each particle has a single degree of freedom. The state of the system can at any time be described by a point $\mathbf{x}$ in an N-dimensional phase space, where each component x_i completely describes the state of the ith particle. We would like to be able to calculate the thermodynamic average of some observable, A, by numerical means. Such averages are, in principle, calculated from

$$\langle A \rangle = \frac{\int_\Omega d\mathbf{x}\, A(\mathbf{x}) \exp\left(-H_N(\mathbf{x})/k_B T\right)}{\int_\Omega d\mathbf{x}\, \exp\left(-H_N(\mathbf{x})/k_B T\right)} \qquad (4.1),$$

where the integration is over the entire phase-space volume, Ω. If the x_i are discrete, as in an Ising model, the integrals in (4.1) are to be interpreted as discrete sums.

To calculate $\langle A \rangle$ we need to numerically evaluate the integrals in (4.1). The conventional way to do this in one dimension is to approximate the integral as a discrete sum,

$$\int f(x)\, dx \; \rightarrow \; \sum_\nu f(x_\nu)\, \Delta x_\nu \,.$$

and take the x_ν to be the points of a regular grid. Since we are dealing with a space of dimension N, with $N \sim 10 - 10^{23}$, this approach is impractical. Alternatively one can choose M phase-space points at random, rather than on a regular grid, and let M be a "manageable" number. The problem with this approach is that many of the M sampled points might be "unimportant", in that the Boltzman factor, $\exp(-H_N/k_B T)$, is much less than one, so that the process is inefficient.

The Metropolis method (Metropolis *et al.*, 1953) uses the idea of "importance sampling", where instead of choosing phase-space points at random we choose them according to some probability $P(\mathbf{x})$. In calculating the integrals or sums in (4.1) we must then correct for this bias by dividing each value $A(\mathbf{x})$ by its weighting factor $P(\mathbf{x})$. Then (4.1) is approximated by

$$\langle A \rangle \approx \overline{A} = \frac{\displaystyle\sum_{\nu=1}^{M} A(\mathbf{x}_\nu)\, P^{-1}(\mathbf{x}_\nu)\, \exp\big(-H_N(\mathbf{x}_\nu)/k_B T\big)}{\displaystyle\sum_{\nu=1}^{M} P^{-1}(\mathbf{x}_\nu)\, \exp\big(-H_N(\mathbf{x}_\nu)/k_B T\big)} \qquad (4.2).$$

If we can somehow choose our weighting function $P(\mathbf{x}_\nu)$ to be equal to the equilibrium thermal distribution, $P_{eq}(\mathbf{x}_\nu) \propto \exp(-H_N(\mathbf{x}_\nu)/k_B T)$, then (4.2) simplifies to

$$\overline{A} = \frac{1}{M} \sum_{\nu=1}^{M} A(\mathbf{x}_\nu) \qquad (4.3),$$

so that we simply compute arithmetic averages, but at a set of phase-space points consistent with our "biasing" distribution.

Although this procedure sounds artificial it turns out that there is a simple prescription for choosing phase space points consistent with $P_{eq}(\mathbf{x}_\nu)$, in the limit $M \to \infty$. The
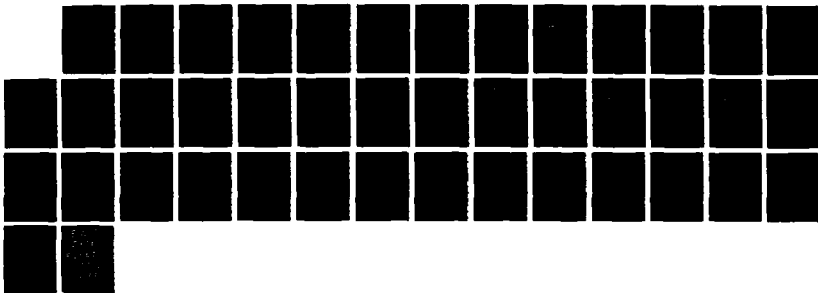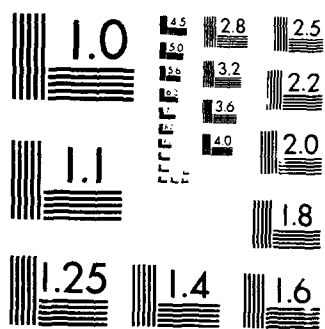
procedure is to execute a random walk in phase space, with the transition probability, $W(x_v \rightarrow x_{v'})$ (per unit time) for a step from x_v to $x_{v'}$ obeying the detailed balance condition

$$P_{eq}(x_v) W(x_v \rightarrow x_{v'}) = P_{eq}(x_{v'}) W(x_{v'} \rightarrow x_v) ,$$

so that the ratio of transition probabilities for $x_v \rightarrow x_{v'}$ and $x_{v'} \rightarrow x_v$ depends only on the energy change $\delta H = H(x_{v'}) - H(x_v)$:

$$\frac{W(x_v \rightarrow x_{v'})}{W(x_{v'} \rightarrow x_v)} = \exp(-\delta H / k_B T) \qquad (4.4).$$

A simple choice of W consistent with (4.4) is

$$W(x_v \rightarrow x_{v'}) = \begin{cases} \exp(-\delta H / k_B T) & \delta H > 0 \\ 1 & \text{otherwise} \end{cases} \qquad (4.5).$$

If, for a given step, δH is less than or equal to zero then the step to $x_{v'}$ is made, and a term $A(x_{v'})$ is added to the sum, (4.3). If δH is greater than zero then we compare W to a value, z, of a random variable uniformly distributed on the interval [0,1]. If $W > z$ then the move is made and $A(x_{v'})$ is added to the sum (4.3), while if $W < z$ the move is not made and $A(x_v)$ is added to (4.3).

In practice, it is often advisable to compute values of the observable A not after every step, but rather after some number of steps. This helps to avoid subsequent terms in the sum (4.3) being highly correlated, since otherwise such terms would differ only by the state of one particle. In addition, one often discards values computed during some initial interval, while the system "equilibrates", and the biasing function $P(x)$ approaches $P_{eq}(x)$.

Our choice of the "averaging interval" and "equilibration time" will be discussed in the next section.

Rather than continuing our discussion in abstract terms we will now specialize to the case of the 2D XY model.

4.3   Monte Carlo simulation of the disordered 2D XY model

Our starting point is the Hamiltonian for the frustrated XY model, (1.13-14), which we reiterate here:

$$H = -J \sum_{<i,j>} \cos(\theta_i - \theta_j - \psi_{ij}) \tag{4.6}$$

$$\psi_{ij} = \frac{2\pi}{\Phi_o} \int_i^j \mathbf{A} \cdot d\mathbf{l} \tag{4.7}.$$

The summation in (4.6) is over nearest neighbors on an $L \times L$ square lattice. Our gauge choice is the Landau gauge,

$$\mathbf{A} = B_o x \hat{y} = \frac{\Phi_o f_o}{s^2} x \hat{y}$$

where s is the lattice parameter. For the simple plaquettes envisioned by GK (see Fig. 4.1a, where the junctions lie on straight lines beween sites i and j, (4.7) reduces to

$$\psi_{ij} = 2\pi \frac{f_o}{s^2} \frac{(x_i + x_j)}{2} (y_j - y_i) \tag{4.8},$$

where the coordinates of the ith spin, or center of the ith superconducting island, are (x_i, y_i). For plaquettes of the type in our samples (Fig. 4.1b) each ψ_{ij} is simply a sum of three terms of the type in (4.8), with endpoints (x_i, y_i) and (x_j, y_j) redefined for each of the three "legs". To introduce positional disorder we assign random diplacement vectors $\mathbf{u} =$

(a)   (b)
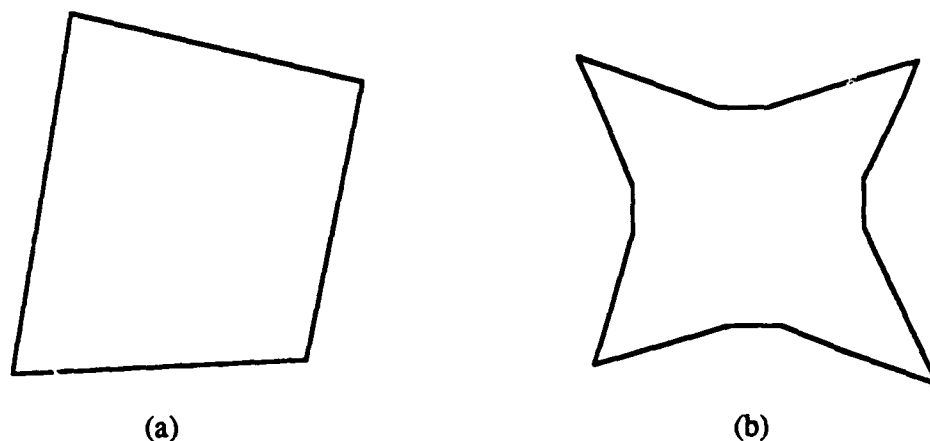
Figure 4.1   Examples of plaquettes, (a) as envisioned by GK, and (b) as realized in our experiments. For the type in (b) each ψ_{ij} is the sum of three terms.

(u_x, u_y) to each site, according to either a gaussian distribution of width Δ, (1.17), or a uniform distribution of half-width Δ^*, (2.1).

Although the subject of boundary conditions merits discussion in any complete review of Monte Carlo simulations, suffice it to say that we have consistently used periodic boundary conditions.

We now outline our implementation of the Metropolis algorithm for this system. We first describe the general procedure, step by step, and then fill in the details of the process as executed on a computer.

4.3.1 Implementation of the Metropolis algorithm

Our random walk through phase space consists in making "passes" through the lattice of spins, adjusting each spin once every pass according to the Metropolis algorithm. The adjustment of a single spin is called a "Monte Carlo step". Rather than stepping through the lattice in regular order, by row for example, we have used a random number generator at the outset, to generate a random order, which was then used for every pass. The use of a random order is generally thought to reduce correlations in the state of the system from one step to the next (Binder, 1974).

During each pass then, for every spin, we execute the Metropolis algorithm as follows:

1) Select a spin, n, and change its spin angle by a random amount $\delta\theta_n$, from θ_n to $\theta_n + \delta\theta_n$. The choice of $\delta\theta_n$ will be discussed below.

2) Compute δH using 4.6, and $W = \exp(-\delta H/k_B T)$.

3) (a) If $\delta H < 0$ accept move. If desired (see subsequent discussion), compute new value of each observable and add to sums, (4.3).

   (b) If $\delta H > 0$ generate a random number z, $0 < z < 1$.

   If $W > z$ accept move. If desired, compute new value of each observable and add to sums, (4.3).

   If $W < z$ reject move. If desired, add *old* value of each observable to sums, (4.3).

4) Go to step 1).

The choice of spin angle change, $\delta\theta_n$, in step 1) above merits discussion. The prescription we have used is to choose a maximum angle change $\delta\theta_{max}$, and then choose $\delta\theta_n$ randomly in the interval $[-\delta\theta_{max}, \delta\theta_{max}]$ by computing a random number γ, from a random variable distributed uniformly on $[-1,1]$, and setting $\delta\theta_n = \gamma \cdot \delta\theta_{max}$. The value of $\delta\theta_{max}$ is adjusted throughout the early stages of the random walk (usually the first 30 – 40

passes) so that the acceptance rate for "uphill" moves (moves with $\delta H > 0$) is approximately one half:

$$\text{Acceptance rate} \approx \frac{\text{No. of uphill successes}}{\text{No. of uphill attempts}} \approx \frac{1}{2} \qquad (4.7)$$

This is a standard prescription (Binder, 1974) which promotes efficiency by discouraging consideration of "unlikely" moves.

As discussed in section 4.2, it is desirable to discard values of observables, A, computed during the initial stages of the random walk, to allow the system to equilibrate, and to avoid correlations with the initial state of the system. In practice, taking note of work by numerous other authors on Monte Carlo simulation of XY models (see for example, Tobochnick and Chester, 1979; Teitel and Jayaprakash, 1983a; Fernández et al., 1986), we have discarded the first 5,000 – 10,000 passes, which we designate as the "equilibration period". During this time we execute the Metropolis algorithm repeatedly, as outlined in steps 1) – 4) above, but without calculating values for any observables, A. It is during the first 30 – 40 passes of this period that $\delta\theta_{max}$ is adjusted according to (4.7).

After this equilibration we executed typically 10,000 – 20,000 passes, now calculating all the quantities of interest *after each pass*. This is preferable to computing quantities after every *Monte Carlo step*, because it reduces correlations between subsequent values of $A(x_v)$. Actually, our program allows for calculation of all quantities after every n^{th} pass, but we have always set $n=1$.

To calculate quantities as a function of temperature we have followed an "annealing schedule" in which we started at high temperature, $T/J \approx 2$, and then gradually "cooled down", usually to $T/J = 0.01$, in 20 – 25 steps. At the highest temperature we used a random spin configuration as initial condition, while for each successive lower temperature we used the final configuration from the previous higher temperature as input. At each

temperature we also used the value of $\delta\theta_{max}$ from the previous temperature as an inital guess for the maximum angle change.

At *each* temperature then, we executed 5,000 – 10,000 equilibration passes, and 10,000 – 20,000 averaging passes. Although it is impossible to know *a priori* how long an equilibration is necessary, we note that Fernández *et al.* (1986) have found from their simulations that the pure XY model appears to exhibit a size-dependent relaxation time τ_L, which follows the form $\tau_L(passes) \approx 2L^2$. For our simulations , with $L = 16$, this gives $\tau_L \approx 500$ passes, so that our equilibration times are approximately $10 \ \tau_L - 20 \ \tau_L$. Of course, it is quite possible that the presence of disorder could increase this relaxation time, or lead to a non-exponential approach to equilibrium. We have found in limited trials, however, that increasing both equilibration and averaging times by a factor of ten does not have an appreciable effect on the results. Extensive checks of this kind are impractical due to the large amount of computing time required.

It is important to have some feeling for the computing time needed for the calculations being discussed. All of the Monte Carlo results presented in this chapter were obtained either on an Apollo DN330 microcomputer, or on a VAX 8600 minicomputer. A typical "run" would calculate, for a *single disorder realization* on a 16×16 lattice (i.e. a given set of site-displacement vectors), the values of the energy, specific heat, helicity modulus and magnetization modulus, at 24 temperatures, with 5,000 passes for equilibration and 10,000 for averaging. Such a run would use 1.4 cpu-days on the Apollo or 10 cpu-hours on the VAX. As will be discussed later, we have frequently performed a "disorder average", where we executed runs for 2– 30 different disorder realizations (with a given value of Δ or Δ^*) and averaged the results. Even an average of five disorder realizations takes one cpu-week on the Apollo and more than 2 cpu-days on the VAX. Our most extensive run, results of which are presented in Fig. 4.8, averaged over 37 realizations, and used 52 cpu-days on the Apollo! It is apparent that any more comprehensive

numerical work on this problem will require the use of a supercomputer.

4.4   Monte Carlo results

4.4.1 Specific heat, C

We have calculated the specific heat of our $L \times L$ spin systems using the relation (Reif, 1965, p. 242)

$$C = \frac{\langle E^2 \rangle - \langle E \rangle^2}{N k_B T^2} \qquad (4.8),$$

where C is the specific heat *per spin*, E is the total energy of the system calculated from (4.6), and $N=L^2$ is the number of spins.

The behavior of C is actually rather uninteresting in the KT transition, showing only a broad, size-independent peak, at a temperature just above T_c, with no divergence or cusp. Fig. 4.2a shows results for a value of the gaussian disorder parameter $\Delta=9.974 \times 10^{-4}$, so that the theoretical critical field (1.29) is 100:

$$f_c = \frac{1}{\sqrt{32\pi}} \frac{1}{\Delta} \approx \frac{0.10}{\Delta} \qquad (1.29)$$

The results for $f_o = 0$ show a peak at $T/J \approx 1.1$, of height $C/k_B \approx 1.5$, consistent with the results of Tobochnick and Chester (1979). The peak does not occur exactly at $T_c \approx 0.9J$ because only vortex pairs with the largest separation (in principle, infinite separation) become unbound there, while as temperature increases more and more tightly-bound pairs
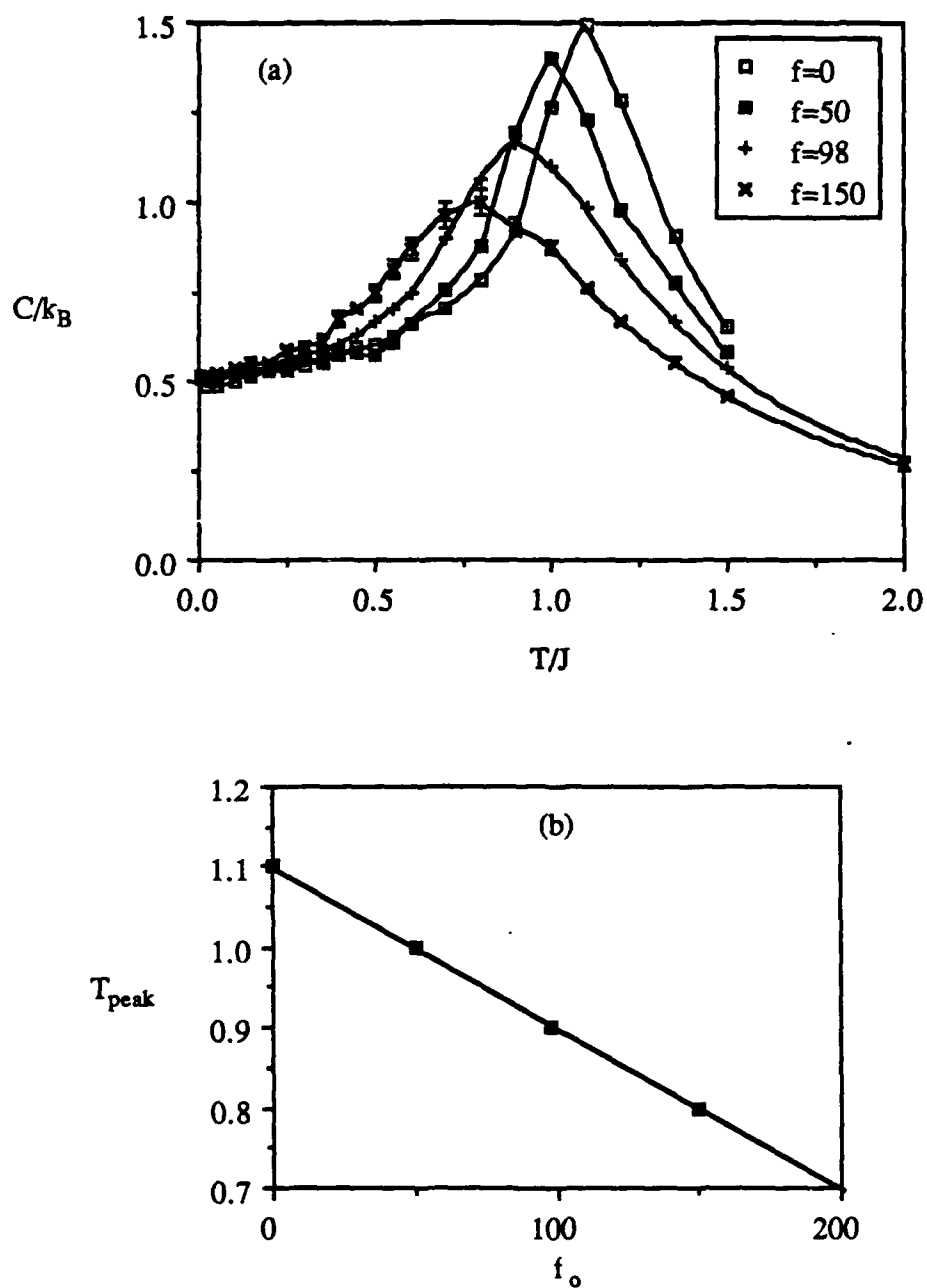
Figure 4.2 (a) Specific heat per spin, for a 16×16 array, with Δ such that $f_c = 100$. (b) Position of the specific heat peak in (a), vs. magnetic field, showing a linear depression of the peak position.

unbind, contributing more and more entropy to the system, until all pairs are unbound. The maximum in C, which corresponds to the maximum rate of increase of entropy with temperature, then occurs *above* T_c, at a temperature where many tightly-bound pairs are being separated.

From Fig. 4.2a one sees that, as the field is increased, the peak position shifts to lower temperatures and its amplitude decreases, indicating a depression of T_c by the field. There is however no novel behavior for fields $f_o \geq f_c$, and no evidence of a second peak associated with a second vortex-unbinding transition. As shown in figure 4.2b, the position of the peak, T_{peak}, simply decreases linearly with field, extrapolating to $T = 0$ at $f_o \approx 5.2 f_c$.

4.4.2 Magnetization modulus, η.

A quantity which gives information about the behavior of the phases, or spin angles, θ_i, is the magnetization modulus, η (Ebner and Stroud, 1982):

$$\eta = \frac{1}{N} \left\langle \left| \sum_{j=1}^{N} e^{i\theta_j} \right| \right\rangle \tag{4.9}.$$

When all the spins are aligned at $T = 0$, then $\eta = 1$, while at high temperatures, where the phases are randomized, $\eta \approx 1/\sqrt{N}$, a finite-size limited value. For the pure XY model, in zero field, this quantity is considered a reliable measure of long-range order. However, in a finite magnetic field, it is *not gauge-invariant*, and therefore is not a measurable quantity. Despite this fact, η turns out to be interesting in its own right.

For an infinite 2D XY system, with no disorder, $\eta(T)$ shows a gradual decrease with
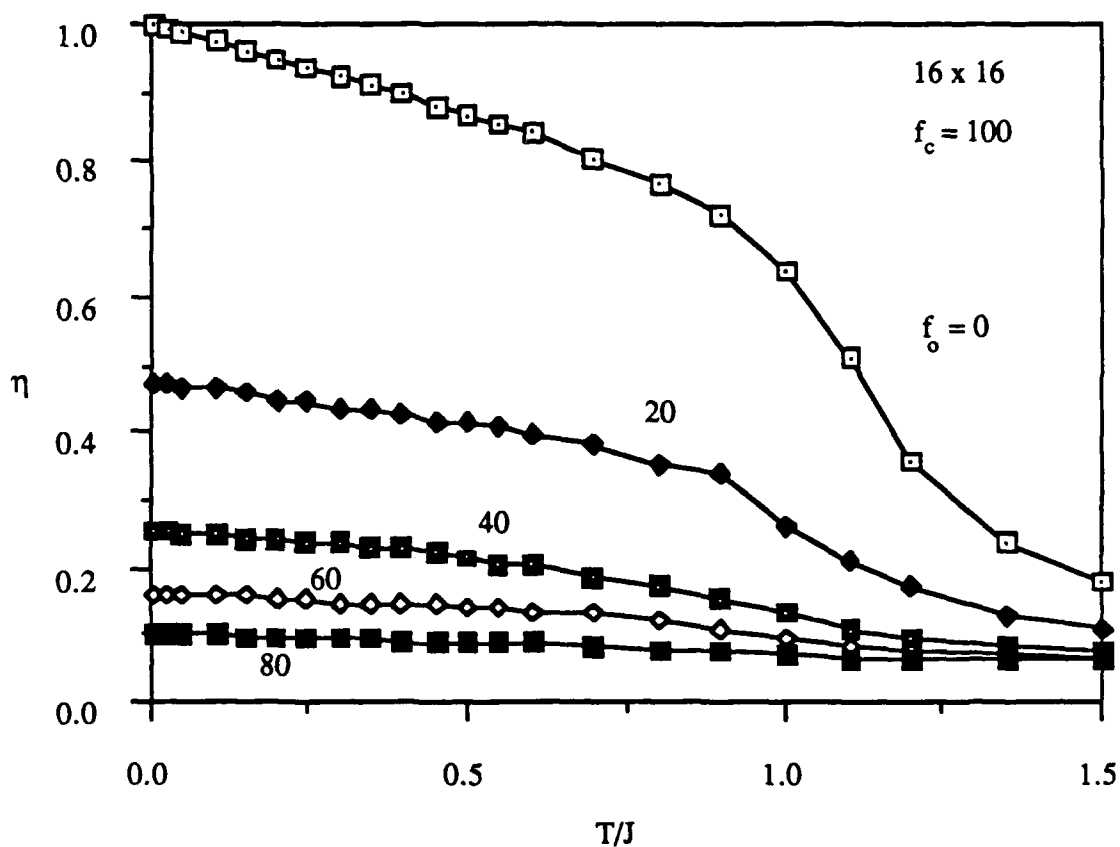
Figure 4.3 Manetization modulus, η, vs. temperature, for a single disorder realization, with $f_c = 100$. One sees that increasing the field supresses η towards its finite-size value, $1/\sqrt{N} \approx 0.067$, indicating that the phases are becoming essentially completely randomized, as f_o approaches f_c.
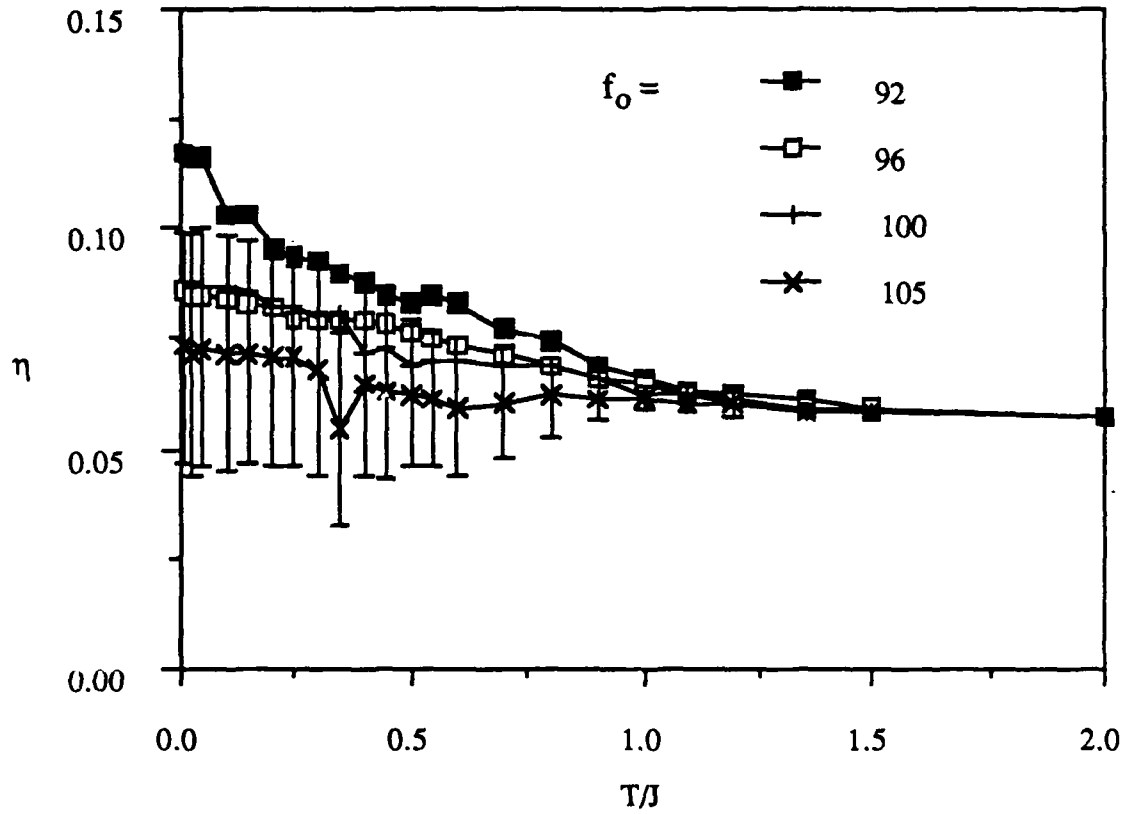
Figure 4.4   Magnetization modulus, $\eta(T)$, in a 16×16 array, for fields f_o close to the theoretical critical field $f_c = 100$, and averaged over $3 - 8$ disorder realizations. η becomes essentially flat for fields within a few percent of f_c. Representative error bars are plotted only for $f_o = 105$ (5 realizations) for clarity.

increasing temperature, and then a sharp drop to zero at $T = T_c$. The behavior for our 16×16 system is shown in Fig. 4.3, where the upper trace is for $f_o = 0$, equivalent to the pure XY model, and shows a very broad decay in $\eta(T)$ in the vicinity of $T_c \sim J$.

The other data in Fig. 4.3 are again for a value of Δ such that $f_c=100$, and are for only one disorder realization. One sees a trend that η is depressed more and more, at all temperatures, as f_o approaches f_c. For $f_o = 80$, $\eta(T)$ has become almost constant with temperature, showing little development of phase ordering as temperature decreases. Figure 4.4 shows similar data, now with an expanded vertical scale, for f_o within ten percent of f_c, and with each trace representing an average over 3–8 disorder realizations. One sees that the trend of Fig. 4.3 is continued and that for $f_o \sim f_c$, $\eta(T)$ becomes essentially flat, so that there is *no* development of phase ordering as temperature decreases. This behavior also seems to persist for fields $f_o > f_c$, but has not been checked for very high fields.

Our interpretation is simply that, as $f_o \rightarrow f_c$, the ψ_{ij}'s in the Hamiltonian (4.6) essentially all become large compared to 2π, so that ψ_{ij} *modulo* 2π become essentially uniformly distributed random variables on the interval $[0,2\pi]$ or $[-\pi,\pi]$. The spin-spin coupling, which wants to minimize the gauge-invariant phase differences, $\theta_i - \theta_j - \psi_{ij}$, then orients the phases θ_i at random angles, so that η retains its high-temperature, finite-size limited value $1/\sqrt{N} = 1/16 \approx 0.063$ at all temperatures.

To investigate the nature of the disordered phase with $f_o > f_c$ it would be of interest to calculate gauge-invariant two-point correlation functions (*cf.* (1.1)), to see how correlations decay with distance in this region. Such calculations are much more numerically intensive than those presented here, and are presently beyond the scope of our computing power.

The behavior of $\eta(T)$ has actually served to verify our approximate relation $\Delta \approx \Delta^*/\sqrt{3} \approx \Delta^*/1.73..$, relating the gaussian disorder parameter for the plaquettes of Fig. 4.1a, and

the uniform disorder parameter for the experimental-type plaquettes of Fig. 4.1b. As discussed in section 4.3, by suitable definition of the ψ_{ij}'s we can perform simulations for the latter type of sample. Results for $\eta(T)$ then show that η becomes independent of temperature at a field which is approximately 1.7 times that expected from the naive relation, $\Delta = \Delta^*$, so that the effective disorder must be 1.7 times *less*.

4.4.3 Helicity modulus, Y.

The helicity modulus, Y, of a magnetic system is, in a sense, an analog of the shear modulus of a solid. If we take a 2D XY spin system and cant the phases along one edge, while holding those along the opposite edge fixed (see for example Fig. 1.2(a)), then Y tells us the increase in free energy of the system in response to the twist induced in the system, *in the limit that the wave vector of the twist, k, goes to zero.* In general Y is a 2×2 matrix (in two dimensions):

$$Y_{ij} = \lim_{k_i, k_j \to 0} \frac{\partial^2 F}{\partial k_i \partial k_j} \qquad (4.10),$$

where F is the free energy per unit area. It turns out that, in an isotropic system in equilibrium, the principal component $Y_{xx} = Y_{yy} = Y$, is simply related to the stiffness, K, discussed in chapter one, by

$$Y = K \cdot k_B T \qquad (4.11),$$

and in a square array in equilibrium is equal to the effective superfluid density, $n_s^{eff} =$

$\hbar i_c{}^R/2e$, where $i_c{}^R$ is the fully renormalized critical current.

To calculate Y we have not in practice applied a twist as described above, and computed the resulting increase in free energy. Instead we have used a response-function type approach, using an expression from Shih et al. (1984):

$$Y = \frac{1}{N}\sum_{<i,j>} J \Delta x_{ij}^2 \langle \cos(\theta_i - \theta_j - \psi_{ij}) \rangle - \frac{1}{Nk_BT} \left\langle \left[\sum_{<i,j>} J \Delta x_{ij} \sin(\theta_i - \theta_j - \psi_{ij}) \right]^2 \right\rangle$$

$$+ \frac{1}{Nk_BT} \left\langle \sum_{<i,j>} J \Delta x_{ij} \sin(\theta_i - \theta_j - \psi_{ij}) \right\rangle^2 \qquad (4.12),$$

where $\Delta x_{ij} = x_j - x_i$, and Y is the helicity modulus per spin. This expression follows from assuming that the twist in the phases progresses uniformly across the sample, so that one can consider a Hamiltonian of the form

$$H = -J \sum_{<i,j>} \cos(\theta_i - \theta_j - \psi_{ij} - k\Delta x_{ij})$$

Using this form in the partition function, $Z = \int d\Omega \exp(-H/k_BT)$, one can compute the free energy from $F = -k_BT \ln Z$. Evaluating d^2F/dk^2, *in the limit $k = 0$*, one obtains the result 4.12. The assumption of a uniform twist is probably unrealistic, except perhaps in some average sense, where one considers an ensemble of samples. In effect we have tried to do this by performing a "disorder average" in our computations, averaging results from a number of samples, with different configurations of site-displacement vectors. The meaning of Y as computed by (4.12) is admittedly uncertain when considering individual samples. Despite this, the use of this expression, or variants of it, is quite widespread in the literature (Teitel and Jayaprakash, 1983a; Shih et al., 1984; Choi et al., 1987)
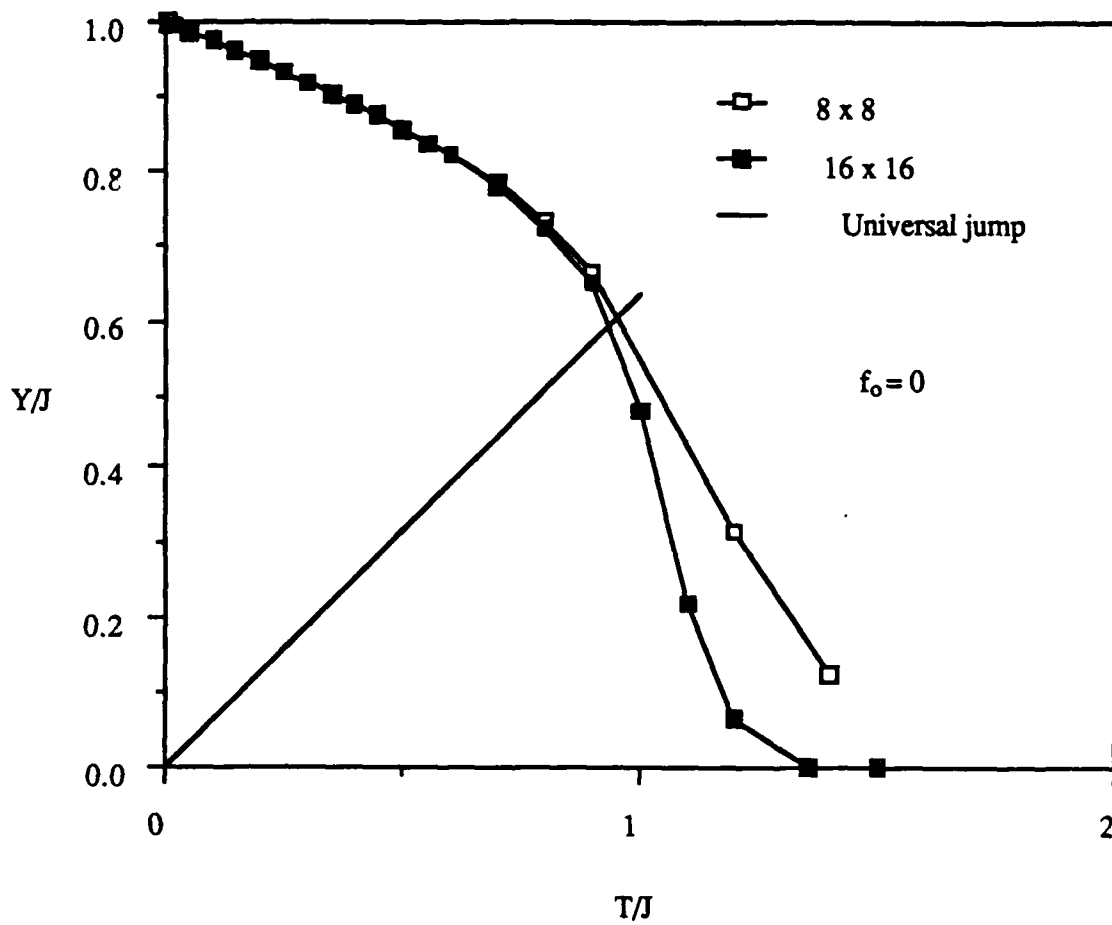
Figure 4.5 Helicity modulus versus temperature, in zero field, for an 8×8 and a 16×16 sample. The diagonal line is the universal jump prediciton of Nelson and Kosterlitz (1977).

Fig. 4.5 shows results for L=8 and 16, with f_o=0. The line, of slope $2/\pi$, is the universal jump prediction of Nelson and Kosterlitz (1977). In an infinite sample Y should drop discontinuously to zero when it intersects this line, so that $Y(T_c)/T_c = 2/\pi$, but in small samples this discontinuity is smeared out, as discussed in chapter one.

In the presence of disorder Y turned out to be numerically less "well-behaved" than the energy, specific heat, and magnetization modulus, and data for *individual* disorder realizations seemed to fall into one of three classes. The first class showed wild
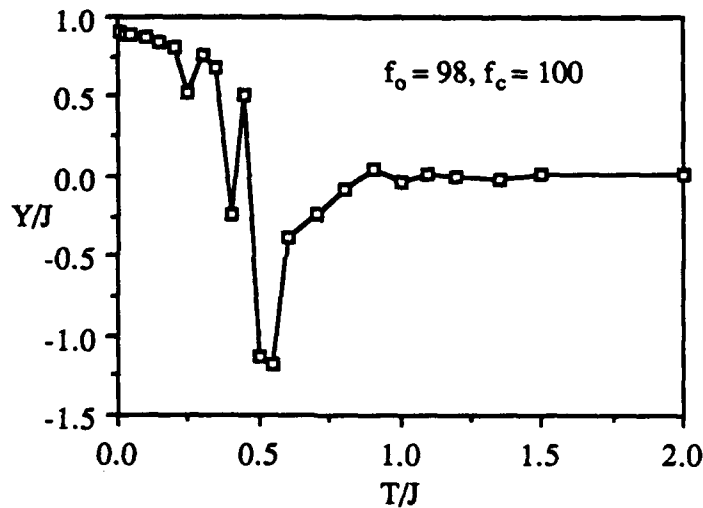
Figure 4.6   An example of pathological behavior in the helicity modulus vs. temperature, for a single realization of a 16×16 sample with $f_o = 98$ and f_c =100.

fluctuations as a function of temperature, often giving *negative* values at some temperatures. Although such fluctuations appeared random, they were in fact reproducible from run to run, starting with different initial spin configurations. Similar behavior has been seen (Chung, 1987) in a Monte Carlo study of the *fully frustrated* XY model with positional disorder (which is *not* expected to show a reentrant phase transition) (Choi *et al.*, 1987). Such behavior was occasionally seen at fields as low as 20% of the critical

field, but became more common for f_o approaching f_c. Figure 4.6 shows an example of this behavior, in one 16×16 lattice, for $f_o = 98$, and Δ such that $f_c = 100$.

By contrast, many disorder realizations resulted in a second class of behavior, where the helicity modulus was well behaved, even at some fields close to f_c, with $Y(T)$ increasing monotonically with decreasing T, much like the results for $f_o=0$ in Fig. 4.5, but with a depressed T_c. A third type of behavior was also common, wherein as T decreased, Y first increased, then decreased over a narrow temperature range, and then increased again at the lowest temperatures. Figure 4.7 gives two examples illustrating varying degrees of this "doubly reentrant" behavior in 16×16 arrays, both for a value of $\Delta = 0.015$, so that $f_c = 6.67$. The data in Fig. 4.7a represent an average over four independent runs for *one disorder realization*, and show a very sharp dip in Y, with a minimum at $T/J \approx 0.025$. The error bars, which represent the uncertainty in the mean of the four values of Y at each temperature, are very small except in the dip. Figure 4.7b shows results for another disorder realization, now with $f_o=5$ and $f_c=6.67$, and showing only a subtle dip in $Y(T)$, at $T/J \approx 0.05$.

Data which showed a well-behaved $Y(T)$ (i.e. no wild fluctuations) *and* reentrant behavior tended to have two common characteristics. First, the reentrance was observed at low temperatures – usually for $T/J < 0.2$, and second, Y/J was always finite and close to one at the lowest temperature simulated (usually $T/J = 0.01$). By contrast, realizations which gave a wildly fluctuating $Y(T)$ usually showed such behavior over a range of T/J, from approximately 1 to 0.1, with Y/J again always approaching a value close to one at the lowest temperature.

In a sense, different disorder realizations seemed to exhibit $Y(T)$ "fingerprints", which fell into one of the three classes discussed, and which were reproducible from run to run, regardless of inital conditions, and apparently independent of the annealing schedule to the limited extent to which we were able to check. This suggests comparison with the
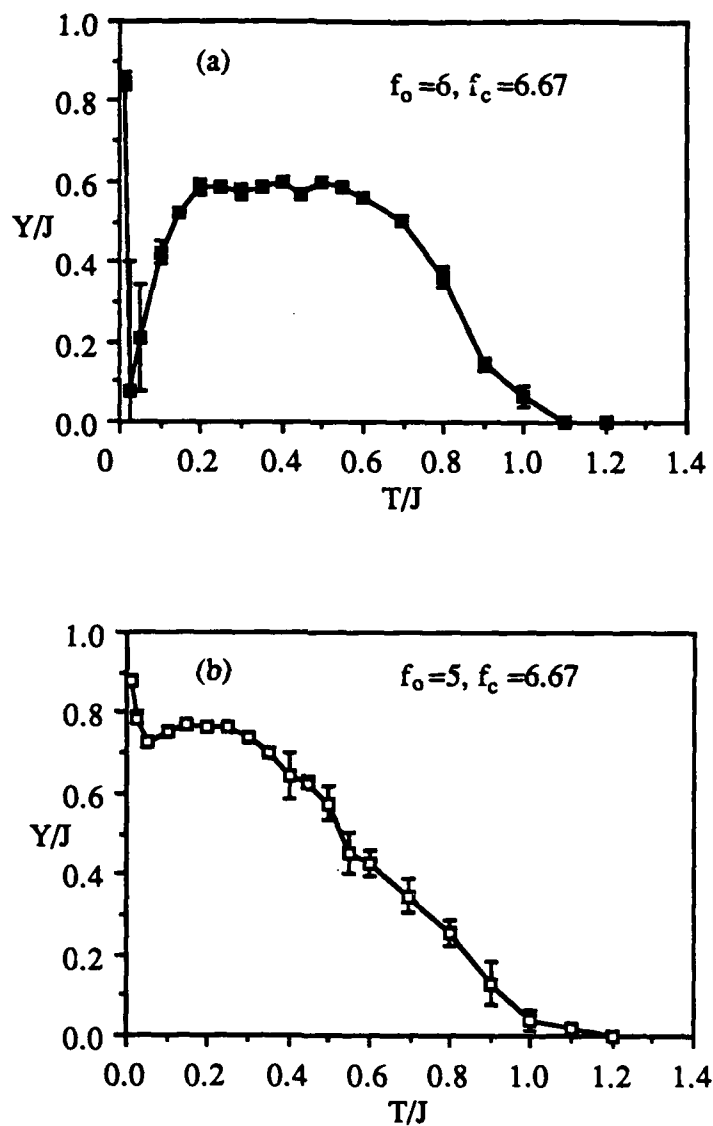
Figure 4.7   Examples of reentrant behavior in the helicity modulus, for two different disorder realizations, both with Δ such that $f_c = 6.67$, for (a) $f_o = 6$ and (b) $f_o = 5$.

well-known magnetoresistance fingerprints (Lee *et al.*, 1987) found in disordered conductors (Benoit *et al.*,, 1987; Skocpol *et al.*, 1987), which become most prominent when the sample size is small compared to the inelastic scattering length. Such fingerprints are then associated with particular distributions of scattering centers, analogous to our particular sets of site-displacement vectors.

To the extent that constraints on computing power have allowed, we have investigated the effect of disorder averaging, to see if the reentrant behavior in the helicity modulus persisted. In a sense such averaging helps us to understand the behavior of large samples from our results on small lattices. Figure 4.8 shows what we consider to be our most important result. This figure shows $Y(T)$ for $f_o = 98$ and $f_c = 100$, averaged over 37 disorder realizations, along with the result for $f_o = 0$ for comparison. This is the run alluded to in section 4.3.1, which used 52 cpu-days on an Apollo DN330. The value of $f_o = 0.98 f_c$ was chosen so as to approach the theoretical phase boundary, so that, according to the qualitative phase diagram of Fig. 1.9, the reentrant transition temperature, $T_c^-(f_o)$, should be essentially at its maximum.

The results show doubly reentrant behavior, qualitatively similar to that shown in Figs. 4.8a and b, but with the dip in Y occuring now at $T/J \approx 0.5$, rather than at $T/J \approx 0.05$ or lower. Apparently the low temperature reentrant behavior of Fig. 4.8, which was part of an otherwise well-behaved $Y(T)$ fingerprint, does not persist through disorder averaging. Instead, the disorder realizations which gave wildly fluctuating results over a broad temperature range average in such a way as to leave a dip in $Y(T)$ at relatively high temperature. The large negative values present in many of the individual realizations do not generally persist through such averaging, although some temperatures show slightly negative values, within the one-sigma error bars. One also sees that the magnitude of the error bars peaks near the minimum in $Y(T)$, perhaps suggesting the possibility of a phase-transition at that temperature. Limited runs at $f_o = 96$ showed some evidence for a
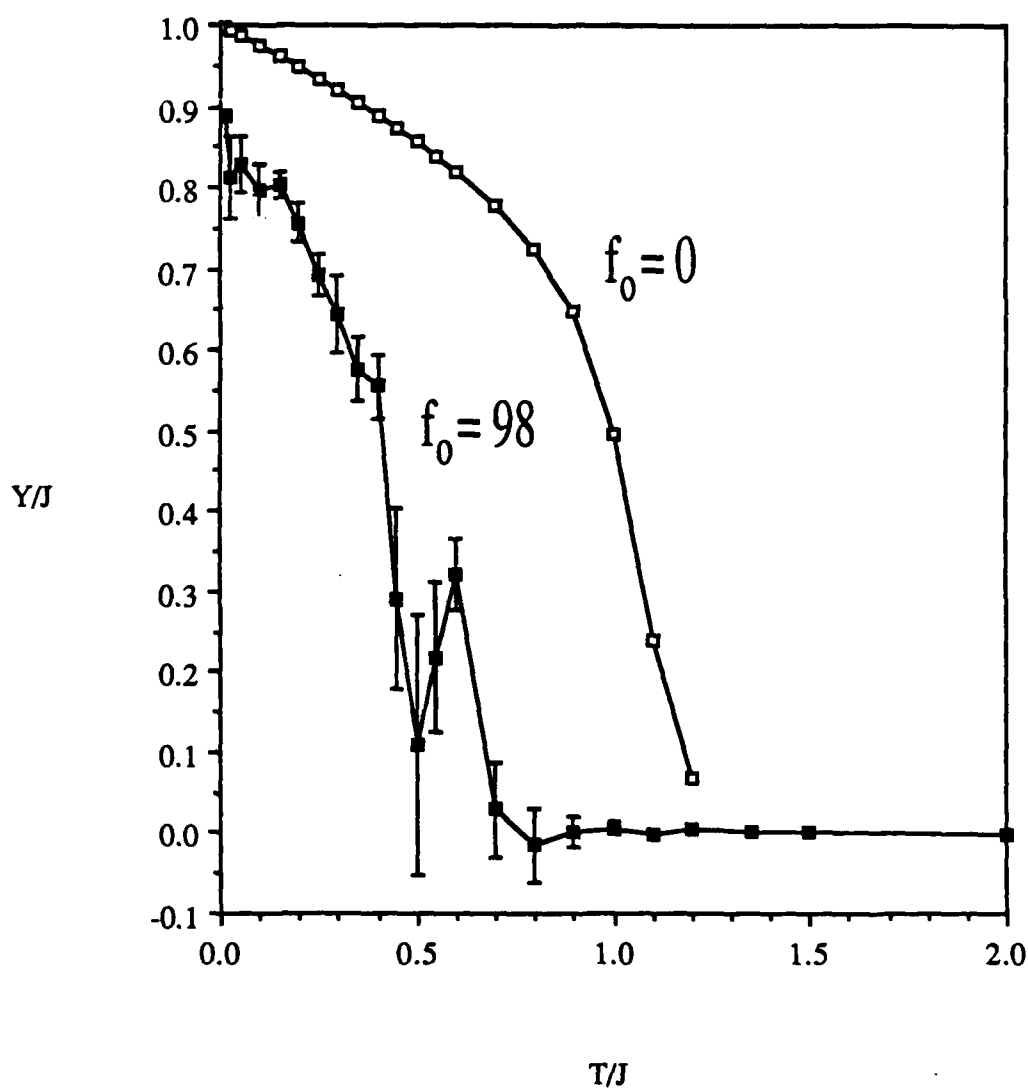
Figure 4.8 Helicity modulus versus temperature for a value of Δ such that $f_c =100$. Upper curve is for $f_o = 0$, where the disorder is irrelevant. The lower curve, which represents an average over 37 disorder realizations, is for $f_o = 98$, and shows evidence for reentrant behavior.
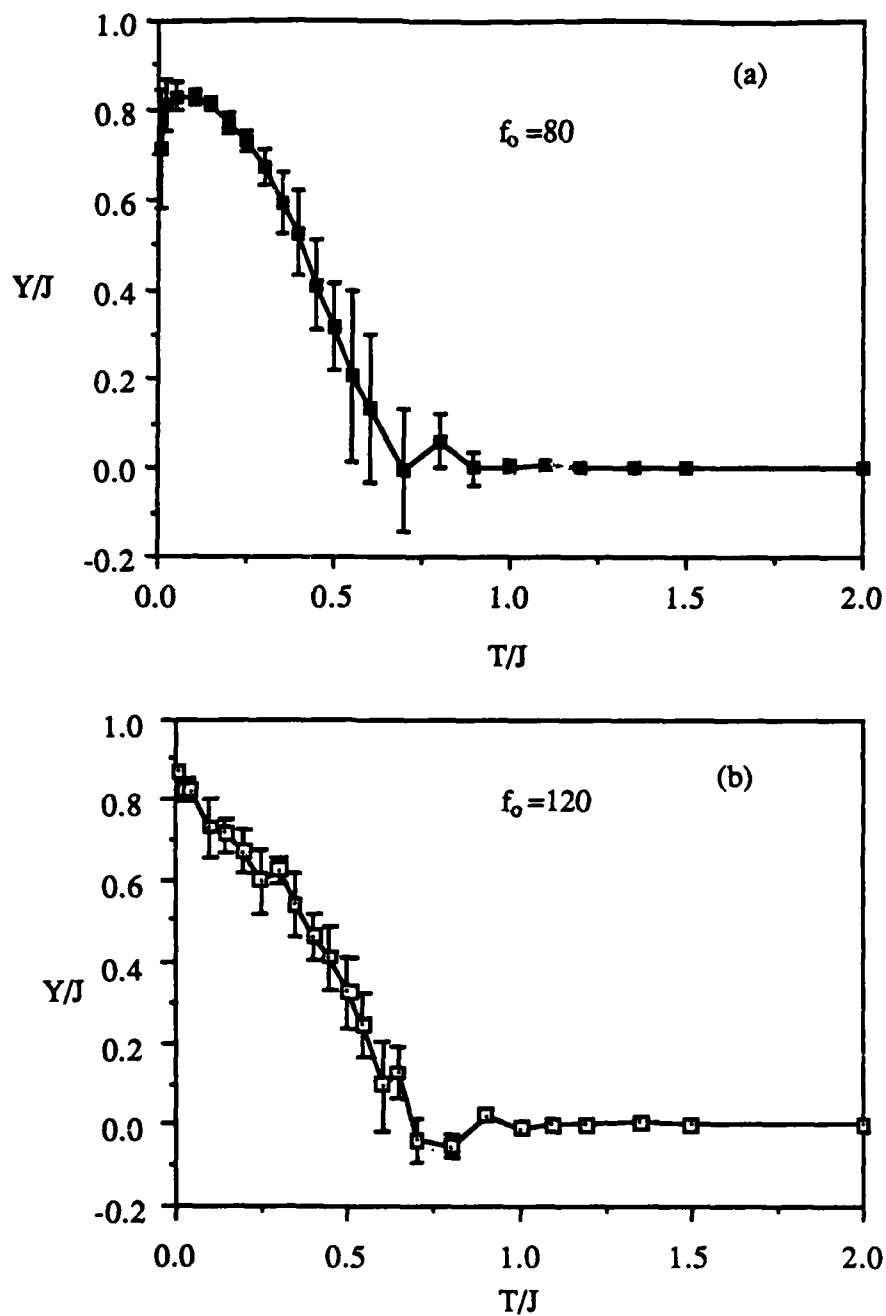
Figure 4.9 Helicity modulus vs. temperature for $f_c = 100$, averaged over 19 disorder realizations, for (a) $f_o = 80$, and (b) $f_o = 120$. The overall shape is similar to that of the background in Fig. 4.8 for $f_o = 98$, but there is no obvious reentrant behavior.

dip $\therefore T/J \approx 0.3$, again with large error bars, but were not conclusive.

Figures 4.9a and b show results for $f_o = 80$ and $f_o = 120$, respectively, again for $f_c = 100$, and with each curve representing an average over 19 disorder realizations. Although, theoretically, $Y(T)$ should be zero at all temperatures for $f_o = 120 = 1.2f_c$, the observed behavior is quite similar to that for $f_o=80$, showing essentially a smooth, monotonic increase in Y with decreasing temperature. The data for $f_o=80$ actually show slight reentrance at very low temperature, due to the fact that two of the 19 realizations showed behavior like that in Fig. 4.7a, with a sharp minimum at low temperature.

Figure 4.10 is a composite of the results for $f_o = 80$, 98, and 120, with the error bars omitted for clarity. Overall, all three curves are quite similar, except for the noticeable dip at $T/J = 0.5$ for $f_o=98$. It appears that there is a reentrant tendency at $f_o=98$, where we are within two percent of the theoretical phase boundary, but that this tendency is being counteracted by the smoothly-rising background which is common to all three values of f_o. There are at least two possible explanations for this effect: finite-size effects and pinning.

We recall that, theoretically, the reentrant phase transition at T_c^- should be brought about by the unbinding of vortex pairs by the quenched random background of dipoles. However, since these vortices are thermally activated, there will be fewer of them present at low temperatures. In a small sample it is possible that there are actually *no* vortices present, at least for part of the time. However, for the helicity modulus to be zero there must be free vortices present at all times to destroy the quasi-long-range order. Unfortunatley it is not a trivial matter to estimate how many vortices should be in our 16×16 samples at a given termperature, *in the presence of disorder*. For the pure XY model, Tobochnick and Chester (1979) found the vortex pair density, $n_p(T)$, to be fairly well described by the approximate expression, $n_p(T) \approx 145 \exp(-9.4J/T)$. For a 16×16 sample this expression says that, on average, there will be one vortex pair present at a temperature $T \approx 0.89\,J$, while at $T \approx 0.5\,J$ there would be approximately 3×10^{-4} pairs
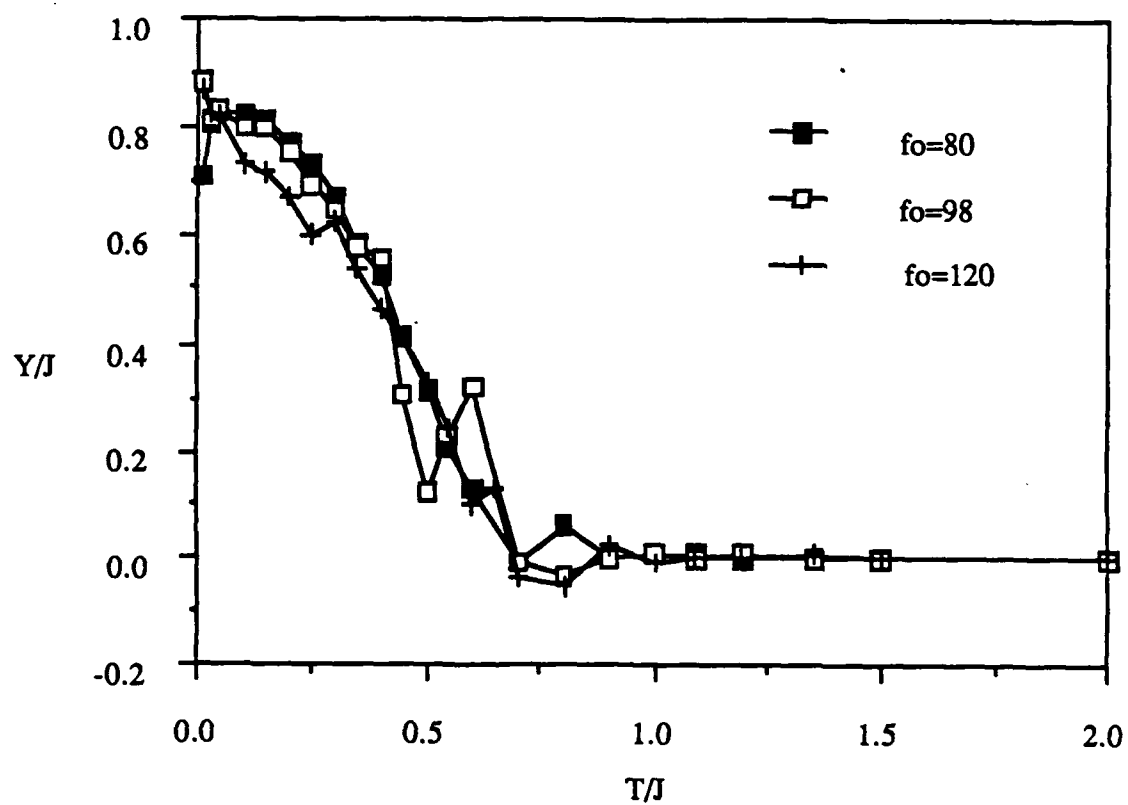
Figure 4.10 Composite plot of helicity modulus data from Figs. 4.8 and 4.9, for $f_o = 80$, 98, and 120.

present, on average! If these numbers were correct it would mean that there were essentially no vortices in our samples at any temperature where we have observed reentrance. Comparing the direction in which the renormalization flows progress at low temperatures, for the pure XY model (Fig. 1.7) and for the disordered system (Fig. 1.8), on sees that the renormalization of the vortex-vortex interaction *decreases* the vortex fugacity y , and therefore the pair density, in the pure case, but *increases* it in the disordered system. The pair density in the disordered system will then exceed that for the pure system at low temperatures.

Since it is impractical to investigate the nature of finite-size effects by studying *larger* samples, we have instead studied samples with $L=2$ and 4. The results are shown in Fig. 4.12, again for $f_o=98$, where the curves for $L = 2$ and 4 represent averages over 20 disorder realizations. The solid line, which is drawn to coincide with the $L = 2$ data at $T=0$, has a *slope* corresponding to the leading-order depletion of Y due to spin waves alone (Ohta and Jasnow, 1979):

$$Y \approx Y(0)\left(1 - \frac{k_B T}{4J}\right)$$

One sees that the results for $L = 2$ follow the spin-wave result rather closely, indicating that vortices are not important in such a sample at any temperature studied. For $L=4$ one sees some deviation from spin-wave behavior for $T/J > 0.7$, indicating that there may be vortices present some of the time at these temperatures. However, most importantly, one sees *no evidence for reentrance for $L=2$ or 4*, consistent with there being no vortices present to bring about a reentrant transition. Again, given the availability of supercomputer time, it would be extremely valuable to investigate much larger samples, say with $L \sim 100$ or larger, to resolve the issue of finite-size effects.

An alternative explanation for the ubiquitous rising background is that, even if there
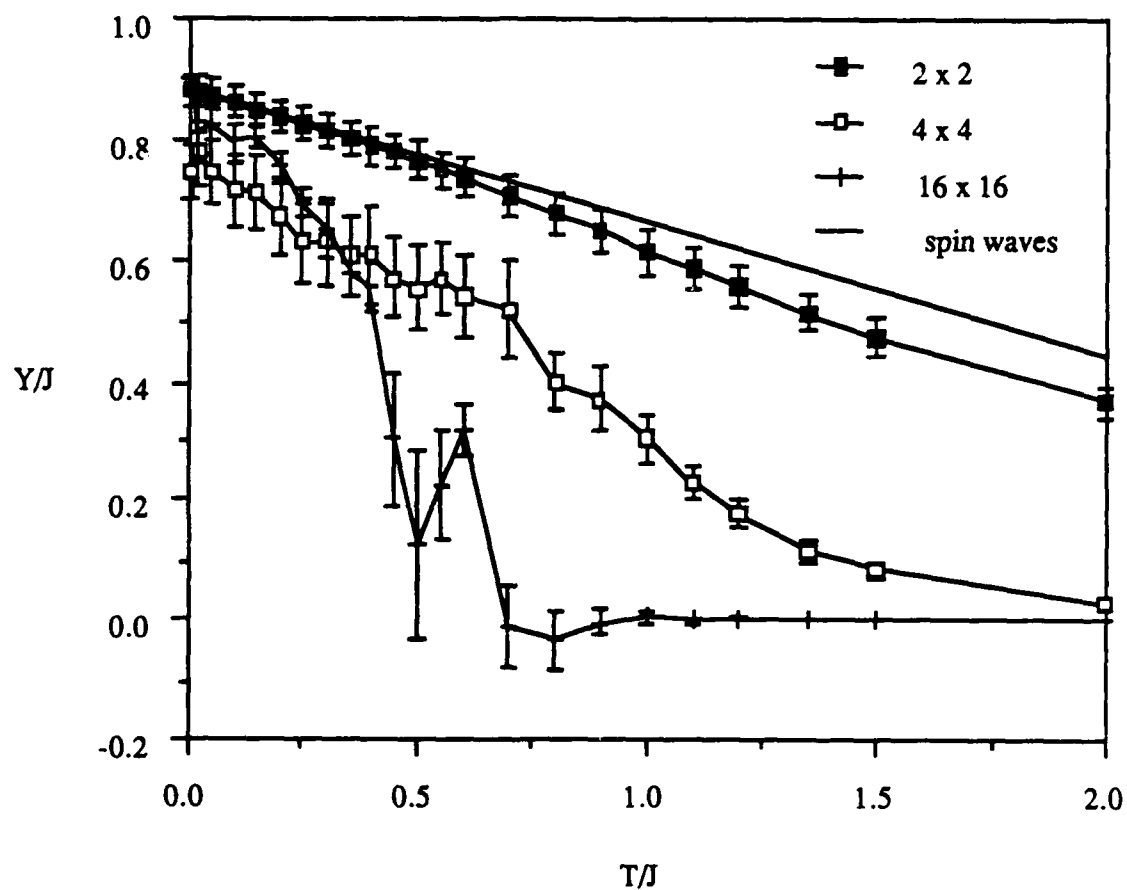
Figure 4.11 Helicity modulus vs. temperature, with $f_o = 98$ and $f_c = 100$, for 2×2, 4×4, and 16×16 arrays. The slope of the solid line corresponds to the spin-wave depletion of Y.

are vortices present, they are pinned by the disorder. If the vortices are not mobile then Y will not go to zero, just as if there were *no* vortices present. The strength of the pinning should increase with the strength of the effective disorder, which increases with magnetic field. The behavior in this low temperature, high disorder regime may be "glassy" in the sense that, if one waited long enough, vortices might be thermally activated out of their pinning sites, but in practical time scales this does not happen and the vortices remain trapped.

D. R. Nelson has pointed out that this system is formally identical to the 2D random binary mixture of hard spheres (ball bearings) studied experimentally by Nelson, Rubinstein, and Spaepen (1982). The disorder in this case was due to the presence of a random admixture of *larger* spheres, which disrupted translational order. These authors found that when a system with a dilute concentration of large spheres was "quenched" by increasing the density of spheres, dislocations, analogous to our vortices, became trapped by the large spheres. Thus, although the shear modulus of the system should have been zero, the fact that the dislocations were not free to move resulted in the system having a finite shear modulus.

It is possible that a detailed study of spin configurations from our simulations might illuminate the role of trapping in our system. Experimentally one could look for evidence of hysteretic behavior, say in I-V characterstics or resistance vs. magnetic fied, as long as one could study a regime where pinning was not *too* strong. In our experiments to date we have observed no evidence of hysteresis.

It is clear that the theoretical work of Granato and Kosterlitz (1986b) provides an oversimplified description of the behavior of a strongly disordered array. The importance of pinning, and the possibility of glassy behavior, were not taken into account, and it is likely that the predicted reentrance, of which we have seen glimpses in our simulations, may be difficult to observe experimentally.

4.5 Summary

In this chapter we have discussed the results of our Monte Carlo simulations of 2D XY magnets with non-uniform frustration, which are model systems for Josephson junction arrays with positional disorder. We have focussed on three quantities in particular – the specific heat C, magnetization modulus η, and helicity modulus Y.

Our results for the specific heat show that in an array with positional disorder there is a single broad peak, similar to that found in the pure XY model. The temperature at which this peak occurred was found to decrease linearly with applied field, extrapolating to $T = 0$ at a field $f_o \approx 5.2 f_c$. We found no evidence for novel behavior as f_o approached the critical field f_c, and no evidence for a second peak associated with a second, low-temperature, vortex-unbinding transition.

The magnetization modulus, $\eta(T)$, although not gauge-invariant, proved to be a useful measure of the degree of ordering of the phases, or spins, in our particular gauge choice. We found that $\eta(T)$ was depressed by the magnetic field, and for fields in the vicinity of f_c, became essentially independent of temperature, and saturated at a finite-size limited value $\approx 1/\sqrt{N}$. This showed that, for such large disorder, there was no development of phase-ordering, as measured by η, as temperature decreased.

Our most important, though inconclusive, results were for the helicity modulus Y, which, in equilibrium, is equal to the effective superfluid density in an array. Simulations of individual disorder realizations showed three types of behavior with decreasing temperature: 1) $Y(T)$ "well-behaved" and increasing monotonically, similar to the zero-field behavior; 2) $Y(T)$ well-behaved but with a dip at temperatures T/J of order 0.05; and 3) $Y(T)$ fluctuating wildly, but reproducibly, with negative values at some

temperatures. All three behaviors shared the common trait that Y/J was finite and close to one at the lowest temperatures, even for fields $f_o > f_c$, where theory says that Y should be zero at all temperatures.

Upon disorder averaging however, we found that reentrant behavior persisted only in a narrow range of f_o close to f_c. The reentrance was actually manifested as a dip in $Y(T)$, on a background which otherwise rose monotonically with decreasing temperature. This background was observed for fields f_o both greater and less than f_c.

Two possible explanations for this lack of complete reentrance ($Y \rightarrow 0$ as $T \rightarrow 0$), and for the behavior of $Y(T)$ for $f_o > f_c$, are finite-size effects and pinning. The finite-size argument says that our small simulated samples may not contain any vortices at low temperatures, so that quasi-long-range order will not be destroyed and Y will remain finite. Results for smaller samples support this idea by showing that 2×2 and 4×4 arrays, for example, do not appear to contain vortices at any temperature of interest, in as much as their behavior is well-fit by spin waves alone.

The pinning argument says that although there may be free vortices present at low temperatures, they are so well-pinned by the disorder that they cannot move around and destroy the order. Such a strongly pinned phase may be glassy in behavior, with extremely slow equilibration.

At present we are unable to rule out either of these explanations. Simulations of larger systems would hopefully illuminate the role of finite-size effects, while experiments to search for hysteresis might clarify the role of pinning. A sytematic search for vortices in the simulations should provide insight into both effects, and should be a priority for future work.

114

CHAPTER FIVE
SUMMARY

We have presented the results of both experiments and simulations on Josephson junction arrays with positional disorder. Theoretically, such arrays are expected to show novel behavior, including a disorder-dependent critical field, and a reentrant phase transition, in a magnetic field. In the Coulomb-gas analogy, where vortices are described as charges, the disorder introduces a random background of "dipoles" $\mathbf{p_r} \propto f_o \mathbf{u_r}$, where f_o is the average flux per plaquette, in units of the flux quantum, and the $\mathbf{u_r}$ are the random displacement vectors of the superconducting sites. For f_o an integer, Granato and Kosterlitz have predicted that the critical field for the destruction of quasi-long-range phase coherence should be given by $f_c \approx 0.10/\Delta$, where Δ is the width of a gaussian distribution of displacement vectors $\mathbf{u_r}$, and that for fields $f_o < f_c$ the dipoles should weaken the vortex-vortex interaction enough to cause a reentrant vortex-unbinding transition at low temperatures.

We have fabricated 50×50 arrays of Pb/Cu proximity-effect junctions, with cross-shaped Pb islands. We have introduced positional disorder by displacing the centers of the Pb islands by random amounts, while maintaining the distance between the tips of the crosses, so as not to introduce disorder in the junction critical currents. For practical reasons, we have used a *uniform* distribution of displacement vectors, of half-width Δ^*, and have made samples with $\Delta^* = 0, 0.05, 0.10, 0.15,$ and 0.20, in units of the lattice parameter.

Our measurements have emphasized the observation of oscillations in the resistance vs. magnetic field, $R(f_o)$, as a signature of phase coherence. In samples with positional disorder we have found that the principal oscillations decay linearly with field,

disappearing at a field $f_c(q=1) \approx 0.95/\Delta^* \approx 0.55/\Delta$. We have argued that this field marks the destruction of phase coherence on a length scale of order the lattice paramter, s.

By quantifying the destruction of higher-order structure in $R(f_o)$, at rational values $f_o = p/q$, we have quantified the destruction of phase coherence on somewhat longer length scales, of order q times the lattice parameter. Defining critical fields $f_c(q)$ by the disappearance of such structures, we find the empirical behavior $f_c(q) = c_1 + c_2/q^2$. Extrapolating to $q = \infty$, we estimate the critical field for the destruction of quasi-long-range coherence to be given by $f_c \cdot \Delta \approx 0.061 \pm 0.006$, compared to the theoretical result, $f_c = 0.10/\Delta$. We have argued that the systematic suppression of these higher-order structures by, for example, measuring currents and sample inhomogeneity are consistent with our experimental f_c being lower than theoretically expected. The experiments have shown no evidence for the predicted reentrant phase-transition.

On the other hand, our simulations of XY spin systems with positional disorder *have* provided a glimpse of reentrant behavior for fields very close to the theoretical critical field. For a 16×16 array, at a field $f_o = 0.98 f_c$, for example, the helicity modulus Y shows a narrow dip at $=T/J \approx 0.5$, on a background which otherwise increases monotonically with decreasing temperature. For fields $f_o = 0.80 f_c$ and $1.20 f_c$, one sees only the monotonic background, with no evidence for reentrance. We have suggested that the finite value of Y at low temperatures may be due to either finite-size effects or to vortex pinning.

The fact that the reentrant behavior is so subtle in finite samples means that it may be difficult or impossible to observe experimentally. This may depend, however, on whether the reentrance is visible only at integer fields, so that one must have a sample whose disorder is such that there is an integral field value within a few (perhaps as little as two) percent of the theoretical critical field. Theoretically, only the case $f_o = n + 1/2$ has been shown to exclude reentrant behavior (Choi *et al.*, 1987).

There are several possible ways to look for reentrance. In this work we have seen no

evidence for the reppearance of resistance at low temperatures, but we have been unable, because of equipment problems, to make extensive measurements of I-V characteristics in samples with disorder. Future work should emphasize such measurements because one might find reentrance in either the critical current, or in the low-current I-V power, $a(T)$. The relationship between a and the superfluid density has not been established for finite fields, but the work of Van Wees *et al.* (1987) on fully frustrated arrays suggests that a may be sensitive to changes in the nature of the phase transition. Another attractive possibility is to probe the superfluid density more directly through measurents of the complex ac impedance (Leeman *et al.*, 1986). However, for such measurements one must be aware of the effects of both the finite currents induced in the sample, and the finite measurement frequency, both of which will affect the vortex dynamics.

Future computer simulations could be used to conduct a systematic search for vortices in the simulated samples, to determine whether there are vortices present at the temperatures of interest, and if so, whether they appear to be pinned by the disorder. Tobochnik and Chester (1979) have carried out such calculations for the pure XY model, and their results have provided very direct support for the notion of vortex-pairs unbinding at T_c. Given the availability of supercomputer time, it would also be of interest to simulate larger systems, and to calculate two-point correlation functions to investigate the nature of the ordering in finite systems. One could then investigate whether algebraic order was destroyed for fields greater than f_c, in favor of some disordered "glassy" phase which has a finite stiffness over accessible time scales. The study of some kind of *gauge-invarianat* order parameter, as an alternative to the magnetization modulus η studied here, might also provide insight into the nature of the ordering in various regimes. The work on "gauge glasses" by Ling *et al.*, (1983, and references cited therein) may be of interest in this regard.

A disordered Josephson junction array provides a rich system in which the effects of

disorder and frustration on phase transitions can be investigated in a controlled fashion. It is hoped that the experimental and numerical study of arrays with postional disorder will continue to provide insight into the subtle physics of two-dimensional systems, including the possibility of a two-dimensional glass transition.

REFERENCES

Abraham, David W., C. J. Lobb, M. Tinkham, and T. M. Klapwijk, Phys. Rev. B 26, 5268 (1982).

Abraham, David W., unpublished thesis, Harvard University (1983).

Alexander, S., Phys. Rev. B 27, 1541 (1983).

Ambegaokar, V., and B. I. Halperin, Phys. Rev. Lett. 22, 1364 (1969).

Aslamazov, L. G., and A. I. Larkin, Phys. Rev. Lett. 26A, 238 (1968).

Behrooz, A., M. J. Burns, H. Deckman, D. Levine, B. Whitehead, and P. M. Chaikin, Phys. Rev. Lett. 57, 368 (1986).

Benoit, A., C. P. Umbach, R. B. Laibowitz, and R. A. Webb, Phys. Rev. Lett. 58, 2343 (1987).

Benz, S. P., private communication (1987).

Berezinski, Sov. Phys. -JETP 34, 610 (1971).

Binder, K., (editor), *Monte Carlo Methods in Statistical Physics* (Springer, Heidelberg, 1974).

Brown, R. K., and J. C. Garland, Phys. Rev. B 33, 7827 (1986).

Choi, M. Y., and D. Stroud, Phys. Rev. B 32, 5773 (1985).

Choi, M. Y., Jean S. Chung, and D. Stroud, Phys. Rev. B 35, 1669 (1987).

Chung, Jean S., private communication, (1987).

Clarke, J., Proc. Roy. Soc. 308, 447 (1969).

Danchi, W. C., unpublished thesis, Harvard University (1983).

Davidson, A., and C. C. Tsuei, Physica 108B, 1243 (1981).

De Gennes, Rev. Mod. Phys. 225 (1964).

Deutscher, G., and P. G. De Gennes, in *Superconductivity*, edited by R. D. Parks (Marcel-Dekker, New York, 1969), Vol. II.

Ebner, C., and D. Stroud, Phys. Rev. B 25, 5711 (1982).

Epstein, K., A. M. Goldman, and A. M. Kadin, Phys. Rev. Lett. **45**, 534 (1981).

Fernández, Julio F., Manuel F. Ferreira, and Jolanta Stankiewicz, Phys. Rev. B **34**, 292 (1986).

Forrester, M. G., Hu Jong Lee, M. Tinkham, and C. J. Lobb, Jap. Jour. Appl. Phys. **26**, Suppl. 26-3, 1423 (1987).

Gordon, J. M., A. M. Goldman, J. Maps, D. Costello, R. Tiberio, and B. Whitehead, Phys. Rev. Lett. **56**, 2280 (1986).

Granato, E., and J. M. Kosterlitz, Phys. Rev. B **33**, 4767 (1986)a.

Granato, E., and J. M. Kosterlitz, Phys. Rev. B **33**, 6533 (1986)b.

Halperin, B. I., and David R. Nelson, J. Low Temp. Phys. **36**, 599 (1979).

Halsey, T. C., J. Phys. C **18**, 2437 (1985).

Harris, A. Brooks, J. Phys. C **7** (1974).

John, Sajeev, and T. C. Lubensky, Phys. Rev. Lett. **55**, 1014 (1985).

José, J., L. P. Kadanoff, S. Kirkpatrick, and D. R. Nelson, Phys. Rev. B **16**, 1217 (1977).

Kadin, A. M., K. Epstein, and A. M. Goldman, Phys. Rev. B **27**, 6691 (1983).

Kimhi, D., F. Leyvraz, and D. Ariosa, Phys. Rev. B **29**, 1487 (1984).

Kosterlitz, J. M., and D. J. Thouless, J. Phys. C **6**, 1181 (1973).

Kosterlitz, J. M., J. Phys. C **7**, 1046 (1974).

Lee, Hu Jong, M. G. Forrester, M. Tinkham, and C. J. Lobb, Jap. Jour. Appl. Phys. **26**, Suppl. 26-3, 1385 (1987).

Lee, P. A., A. Douglas Stone, and H. Fukayama, Phys. Rev. B **35**, 1039 (1987).

Leemann, Ch., Ph. Lerch, B. -A. Racine, and P. Martinoli, Phys. Rev. Lett. **56**, 1291 (1986).

Ling, D. D., D. R. Bowman, and K. Levin, Phys. Rev. B **28**, 262 (1983).

Lobb, C. J., David W. Abraham, and M. Tinkham, Phys. Rev. B **27**, 150 (1983).

Lobb, C. J., unpublished thesis, Harvard University (1980).

Lobb, C. J., Physica **126B**, 319 (1984).

Mermin, N. D., and H. Wagner, Phys. Rev. Lett. **22**, 1133 (1966).

Metropolis, N., A. W. Rosenbluth, M. N. Rosenbluth, A. H. Teller, and E. Teller, J. Chem. Phys. **21**, 1087 (1953).

Miller, S. L., and D. K. Finnemore, Phys. Rev. B **30**, 2548 (1984).

Minnhagen, P., Phys. Rev. B **32**, 7548 (1985).

Mooij, J. E., private communication (1986).

Nelson, D. R., and J. M. Kosterlitz, Phys. Rev. Lett. **39**, 1201 (1977).

Nelson, David R., Michael Rubinstein, and Frans Spaepen, Phil. Mag. A **46**, 105 (1982).

Ohta, Takao, and David Jasnow, Phys. Rev. B **20**, 139 (1979).

Pannetier, B., J. Chaussy, and R. Rammal, J. Phys. (Paris) Lett. **44**, L853 (1983).

Pearl, J., J. Appl. Phys. Lett. **5**, 65 (1964).

Peierls, R. E., Helv. Phys. Acta. **7**, Suppl. II, 81 (1934).

Rammal, R., T. C. Lubensky, and G. Toulouse, Phys. Rev. B **27**, 2820 (1983).

Reif, F., *Fundamentals of Statistical and Thermal Physics*, (McGraw Hill, New York, 1965).

Resnick, J., J. C. Garland, J. T. Boyd, S. Shoemaker, and R. S. Newrock, Phys. Rev. B **26**, 5268 (1982).

Rubinstein, M., B. Shraiman, and D. R. Nelson, Phys. Rev. B **27**, 1800 (1983).

Sanchez, Daniel H., and Jean-Luc Berchier, J. Low Temp. Phys. **43**, 65 (1981).

Shih, W. Y., and D. Stroud, Phys. Rev. B **28**, 6578 (1983).

Shih, W. Y., and D. Stroud, Phys. Rev. B **32**, 158 (1985).

Shih, W. Y., C. Ebner, and D. Stroud, Phys. Rev. B **30**, 134 (1984).

Skocpol, W. J., P. M. Mankiewich, R. E. Howard, L. D. Jackel, D. M. Tennant, and A. Douglas Stone, Phys. Rev. Lett. **58**, 2347 (1987).

Spitzer, F., *Principles of Random Walk* (Van Nostrand, Princeton, 1964).

Teitel, S., and C. Jayaprakash, Phys. Rev. B **27**, 598 (1983)a.

Teitel, S., and C. Jayaprakash, Phys. Rev. Lett. **51**, 1999 (1983)b.

Tinkham, M., D. W. Abraham, and C. J. Lobb, Phys. Rev. B **28**, 6578 (1983).

Tinkham, M., *Introduction to Superconductivity* (McGraw-Hill, New York, 1975).

Tobochnik, Jan, and G. V. Chester, Phys. Rev. B **20**, 3761 (1979).

Van Harlingen, D. J., and K. N. Springer, Bull. Am. Phys. Soc. **32**, 690 (1987).

Van Wees, B. J., H. S. J. van der Zant, and J. E. Mooij, Phys. Rev. B **35**, 7291 (1987).

Villain, J., J. Phys. C **10**, 1717 (1977).

Voss, R. F., and R. A. Webb, Phys. Rev. B **25**, 3446 (1982).

Webb, R. A., R. F. Voss, G. Grinstein, and P. M. Horn, Phys. Rev. Lett. **51**, 690 (1983).

Yosefin, M., and E. Domany, Phys. Rev. B **32**, 1778 (1985).

APPENDIX

Detailed fabrication instructions for arrays: Positive process

The positive process is used for the disordered arrays and Sierpinski arrays, whose masks

have Cr where the islands will be in the samples.

1) Substrate cleaning:

a) (Start here for used substrates). 30 mins in boiling Shipley PR remover 112A.
b) 2 hours in strong KOH solution, ultrasonic (US).
c) If metal still remains, 2 mins in 1:1 $HCl:HNO_3$.
d) 5 mins. US in distilled water.
e) Blow dry with nitrogen or air.
f) (Start here for new substrates). 5 mins. US in Trichlorethylene (TCE).
g) 5 mins. US in acetone.
h) 5 mins. US in methanol.
i) Blow dry with nitrogen or air.

2) Preparation of PR structure for bilayer:

a) Spin lower layer of PR - Shipley 1400-27 or 1400-33, 4000 rpm, 30 secs.
b) Bake 30 mins. @ 100 C.
c) Flood expose bottom layer, 15 secs in Karl Süss mask-aligner.
d) Evaporate 500-700 Å Al, for PR layer separation. Use alumina coated boat.
e) Spin top layer of PR - Shipley 1400-27, 4000 rpm, 30 secs.
f) Bake 30 mins. @ 90 C.
g) Let cool ≈ 10 mins.
h) Expose in Karl Süss (soft contact mode), using appropriate bilayer mask, 5 secs.
i) Develop ≈ 30-45 secs in 5:1 H_2O:Microposit 351 developer.
j) Rinse immediately with H_2O squirt bottle (not in standing water).
k) Blow dry with nitrogen.
l) Etch Al until ≈ 10 secs. after it appears to be gone. Rinse with H_2O. Blow dry.
m) Develop bottom PR layer ≈ 15-30 secs. Rinse with H_2O. Blow dry.
n) Etch Al under undercut for about same time as step l). Rinse with H_2O. Blow dry.
o) Inspect under microscope. Develop more if necessary to increase undercut.

3) Bilayer deposition.

a) Set up diff.-pumped evaporator for Cu and PbBi(.05) deposition.
b) Mount substrates.
c) Fill boats, tungsten for both materials.
d) Make window to observe boats during evaporation. Set thickness monitor for Pb.
e) Pump down to ≈ 5 x10^{-6} torr.
f) Fill LN_2 trap on diff.-pump.

i)   Turn up accelerator to ≈ 170 V, <u>or</u> to minimize accelerator current.

j)   Adjust cathode current until beam current ≈ 10 mA.

k)   Turn up neutralizer until 'emission' matches beam current.

l)   Turn sample into beam.

m)   Etch until test area is clean Cu color. If there is no test area on the bilayer (for example if it lifted off!) you can usually tell when you're done by looking at the array with a flash-light.

n)   Turn off supplies, reversing steps d through k.

o)   Leave gas on, close gate-valve, and let guns cool 20 mins. before opening chamber.

p)   Remove sample from chamber.

q)   Close and evacuate chamber.

r)   Turn off gas, water, and power supplies.

8) PR removal.

a)   Squirt sample with acetone to remove as much PR as possible. PR may be baked onto islands, but it must be removed from pads.

b)   Soak in acetone if necessary.

c)   Rinse with ethanol (*not* methanol!). Blow dry.

g) Pump until $p < 2 \times 10^{-7}$ torr.
h) Turn up Cu power supply until Cu melts then turn down 25%.
i) Turn up Pb supply until Pb melts ("idle position").
j) Keeping substrate shutter closed, check evaporation rate for Pb ("evaporation position"). Try for ≈ 100 Å/sec.
k) Turn down Pb supply to idle position (as in step i).
l) When Cu has been melted for > 2 mins. open substrate shutter, turn up Cu supply to > 75% full power, wait ≈ 10 secs. for evaporation to get going, then open bottom shutter. At same time turn up Pb to evaporation position.
m) After depositing desired amount of Cu (2000 Å or more) flip lower shutter to Pb position and evaporate 2000-3000 Å Pb. There should be no perceptible break between Cu and Pb evaporations. Turn off Cu supply to conserve Cu.
n) Turn off Pb supply.
o) Let cool ≈ 10 mins.
p) Remove substrates from evaporator and set up for Ge evaporation.

4) Bilayer liftoff.

a) One substrate at a time, holding substrate slightly face-down, squirt with acetone. If necessary let soak in beaker of acetone and then repeat until completely lifted off.
b) Spray with ethanol (*not* methanol!!!! Methanol will disolve Pb!).
c) Blow dry.

5) Ge deposition.

a) Evaporate ≈ 100 Å Ge. This will prevent developer from attacking Pb.

6) PR deposition, exposure, and post-bake.

a) Spin 1400-23 or -25 resist, 4000 rpm, 30 secs.
b) Bake 30 mins. @ 95 C.
c) Let cool 5 mins.
d) Mount appropriate array mask in Karl Süss and align to bilayer.
e) Expose 5 secs. in vacuum contact (HP) mode.
f) Develop ≈ 30 secs in 5:1 H_2O:Microposit 351 developer.
g) Rinse and blow dry.
h) Inspect under microscope.
i) Post-bake 30 mins. @ 110 C (not 120 C).

7) Ion etching with Commonwealth ion-guns.

a) Mount sample in dual-ion-beam system, turned away from beam. Make sure observation window is clear!
b) Pump down to $\approx 1 \times 10^{-6}$ torr.
c) Establish Ar flow of ≈ 10 sccm through gun. Turn on water supply to guns and sample holder
d) Turn on 'source' on Commonwealth power supply.
e) Turn up discharge voltage to 35 V.
f) While observing discharge current, turn up cathode current until $I_D \approx 0.2$ mA. Discharge light should now be steady.
g) Turn on 'beam'.
h) Turn up beam voltage to 35 V.

ACKNOWLEDGEMENTS

It is a pleasure to acknowledge the support and assistance of many individuals throughout my graduate study at Harvard.

Chris Lobb has been both a friend and advisor throughout the past few years, and has provided much-needed encouragement at numerous points (every other day?). When I despaired that nothing would ever work he prodded me to keep going, even when he wasn't really sure either. Chris has taught me practically everything I know about critical phenomena ("What *is* a first order phase transition Chris?") and low-temperature measurements ("Run that explanation of the rf-SQUID by me *one* more time please!") and has never shied away from breaking out the *good* wine in my presence. His sense of humor has helped me to remain sane during the most grim times. Prof. Michael Tinkham has kept a critical eye on the proceedings, and has instilled in me a sense of how to do good science, as well as how to sell an idea to a funding agency!

I greatly enjoyed working with, and learning from, Hu Jong Lee during his all-too-brief stay at Harvard. Without Hu Jong's efforts I would probably have been in graduate school another six years. He literally worked day and night to master the e-beam lithography for mask-making, and did almost all of the work on the Sierpinski gaskets.

I have benefitted from the labors and the company of many graduate students throughout my stay at Harvard. Jim Gordon has always been a good friend and confidant, and showed me the ropes around the lab in the early days. I always enjoyed our late-night discussions, along with Qing Hu, when we all used to work the "late shift". My only regret is that we never made it onto the Letterman show. Charlie Johnson and Marco Iansiti deserve thanks for their development of the e-beam lithography. Gabe Spalding helped to get the ion-beam etching going in the evaporator, and built the excellent chamber

which we ultimately used to produce samples. He was also willing to tune up those MKS gadgets on many occasions. The man has patience! Walter Smith completed numerous projects that I never got around to, including getting the digitizer up and running, and provided instantaneous software updates for his famous "xxanal" plotting program. I would also like to single out Sam Benz for seeing things my way on matters trivial and important, and for helping me to keep my sense of humor throughout the past couple of years.

Horst Rogalla wrote the e-beam software and also patiently answered my numerous questions about sputtering, mask aligners, and anything else I didn't understand. I very much enjoyed his two visits to Harvard. I thank Louis DeFeo for his expertise in the machine shop, and for his willingness to make something on the basis of little more than a verbal description. He has always done the job quickly and skillfully. I would also like to acknowledge useful conversations with Prof. David Nelson, and computer time provided by Prof. Paul Sokol and the Westervelt group.

I would like to thank my parents for their love and support, and for the sacrifices they made to send me to the most expensive university in the country. I hope that I have made them proud.

Finally, I would like to thank my wife Cathy, and my daughter Andrea, for their love, their work, and their patience. I could not have completed this work without them being there for me every day. I am proud to have them as my family, and dedicate this thesis to the two of them.

END
DATE
FILMED
DTIC
11- 88